VIBRATIONAL SPECTROSCOPIC STUDY ON STRUCTURES AND TRANSITION BEHAVIOR OF ION-CONTAINING LONG CHAIN COMPOUNDS

A Doctral Thesis

by

Tsutomu Ishioka

Submitted to the Faculty of

Science, Osaka University

May, 1990

Approvals

April, 1990

This thesis is approved

as to style and content

by

小林雅通

Member-in-chief

寺本明夫

Member

小高忠男

Member

高木俊夫

Member

Acknowledgements

The present work has been carried out under the direction of Professor Masamichi Kobayashi, Department of Macromolecular Science, Osaka University. The author would like to express sincere gratitude to Professor Masamichi Kobayashi for his guidance, critical discussions, and encouragements through all the course of his study. He is also grateful to Drs. Yasuhiro Takahashi and Kohji Tashiro for their continuing instructive suggestions.

The author is indebted to Professors Yukiteru Katsube and Nobuo Tanaka, and Drs. Mamoru Sato and Yukio Morimoto of the Institute for Protein Research, Osaka University for the SAXS measurements and valuable discussions, Dr. Takashi Nogami of Department of Applied Chemistry, Faculty of Engineering, Osaka University for discussions, and Professor Shinichi Yano of Department of Synthetic Chemistry, Faculty of Engineering, Gifu University for information about NATO Workshop on Ionomers (1986).

Thanks are due to all the members of Kobayashi laboratory for their stimulations.

Finally he is sincerely indebted to Professor Yozo Chatani of Tokyo University of Agriculture and Technology for his recommendation to publish this thesis.

January, 1990

Tsutomu Ishioka

Tsutomu Ishioka

Contents

General Introduction 1

References 7

Chapter 1. Brillouin and Raman Study on Melting Process of Ethylene-methacrylic Acid Ionomers 11

1-1. Introduction 12

1-2. Experimentals 15

1-2-1. Samples 15

1-2-2. Brillouin Measurement 15

1-2-3. Raman Measurement 18

1-2-4. Infrared Measurement 20

1-3. Temperature Dependence of Elastic Constant 20

1-4. Polyethylene Crystallite 24

1-5. Structural Change of Polymethylene Moleculoes in Non-crystalline Phase 28

1-6. Structural Change of Aggregation of Ionic Groups and Dissociation of Acid Dimer 37

1-7. Temperature Dependence of Specific Volume 45

1-8. Conclusion 48

1-9. References 51

Chapter 2. Small-angle X-ray Study on Structural Changes of Ion Cluster in Zinc Salt of Ethylene-metahcrylic Acid Copolymer on Water Absorption 54

2-1. Introduction 55

2-2. Experimentals 58

2-2-1. Sample 58

2-2-2. SAXS Measurement 58

2-3. Result and Discussion 59

2-4. References 71

Chapter 3. Infrared Study on Intra-cluster Structural Changes in Zinc Salt of Ethylene-methacrylic Acid Copolymer on Water Absorption 73

3-1. Introduction 74

3-2. Experimentals 76

3-2-1. Sample 76

3-2-2. Infrared Measurement 76

3-3. Result and Discussion 76

3-4. References 96

Chapter 4. Phase Transition of Ion-containing Long-chain Compounds 100

4-1. Introduction 101

4-2. Experimentals 104

4-2-1. Samples 104

4-2-2. Raman and IR Measurements 104

4-3. Results and Discussion 105

4-3-1. Structures and Assignment of Spectral Bands 105

4-3-2. Transition of C_{18}-DABCO-C_{18}-Br_2 109

a) Structural Changes of Alkyl Chain 112

b) Changes in Band Width of the Bicyclo-ring Modes 118

4-3-3. Transition of C_{17}-DABCO-Br and C_{22}-DABCO-Br 128

4-4. Conclusion 131

4-5. References 133

Chapter 5. Application of Raman Microprobe as a New Technique for Polarization Measurement of Microdomain Structures 135

5-1. Introduction 136

5-2. Experimental 138

5-2-1. Microprobe Instrument 138

5-2-2. Samples 138

a) Stearic Acid Overgrown Crystals 138

b) o-POM and α-Quartz 140

5-3. Experimental Spatial Resolution 140

5-4. Calculated Spatial Resolutions 151

5-4-1. Energy Distribution along Z-axis 153

5-4-2. Energy Distribution within X-Y Plane 155

5-4-3. Distributions of $|E_X|^2$ and $|E_Z|^2$ 155

5-5. Analysis of Polarization Measurements 159

5-5-1. Intensities of Polarized Spectra 159

5-5-2. Analysis of Polarized Spectra of α-Quartz and o-POM Single Crystals 164

a) α-Quartz 166

b) o-POM 171

5-6. References 175

Chapter 6. Summary and Conclusions 177

List of publications 184

General Introduction

Ionic polymer is a wide class of materials covering inorganic glass, polyelectrolytes, ionomers, organic polysaccharide gels, etc. Although inorganic glass has a history of several thousand years, it is only in the last 30 years that most of the synthetic ionic polymers have received extensive attention in industrial and scientific fields. The studies of the synthetic ionic polymers were originated from the works by Brown on carboxylated rubbers in 1957,[1] Nielsen on polyacrylates in 1964,[2] and Rees et al. on ionomers in 1965.[3,4] By introducing ionic groups, these studies intended to enhance original properties or to add new characters which original non-ionic substances do not have. Thereafter, a variety of substances has been synthesized and widely utilized as industrial materials up to now. In this new field, general classifications with respect to the structures are not established and the researches of these substances are now in progress by many investigators.[5-10] In this thesis, structures and transition behaviors of two kinds of ion-containing long-chain compounds were studied, i.e., ethylene-methacrylic acid ionomers and N,N'-dialkyl-1,4-diazabicyclo(2,2,2)octane halides.

A series of ethylene(E)-methacrylic acid (MA) ionomers (being first produced in 1965 by Du Pont Co. under the trade name "Surlyn"[3,4,11]) is one of the most extensively studied class of ionic polymers, because of their great industrial importance as thermoplastic polymers. They are copolymers of ethylene and methacrylic acid (less than 10mol%) partially or fully

neutralized with cations such as Na (this salt being denoted with an abbreviation as E-MA-Na) and Zn (as E-MA-Zn), and are distinguished from polyelectrolytes having ionic groups on alternate backbone segments.

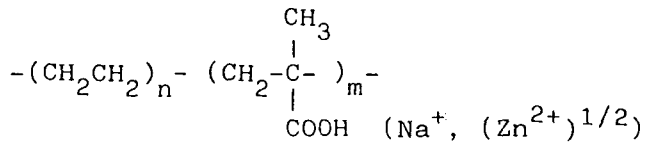

On ionization, their tensile strength and melt viscosity are enhanced remarkably as compared with those of non-ionic low density polyethylene. These physical properties of the E-MA ionomers have been interpreted in terms of association of the ionic side groups. Namely, association of the ionic groups acts as temporary crosslinking point and enhances the mechanical properties. Contrary to the crosslinks by covalent bonds, the ionic linkages were considered to dissociate on heating under stress and to reform on cooling. This feature gives thermoplastic properties to the ionomers.

In order to reveal the mechanism of enhancement of bulk mechanical properties of the E-MA ionomers on ionization from the view point of molecular level structure, determination of the structure of the ion association is desirable at first. The ionomers are non-crystalline or poorly-crystalline and hence wide angle x-ray diffraction method is not readily applicable to the systems. Alternative approaches for structural analysis of the ion association should be necessary. The structures of such systems have been investigated with a variety of experimental techniques: Mössbauer spectroscopy, magnitization measurement,

and electron spin resonance were used for some ionomers containing specific metals to indicate the aggregation state of the metal ions.[12-16] Existence of the ion aggregate with a dimension of several 10Å in diameter was confirmed by electron microscopy.[17-19] Small angle x-ray scattering (SAXS) technique has been utilized to determine the shape and the size of the ion aggregate.[20-26] In spite of these many studies, the detailed structure of the aggregate is still uncertain.

The characteristic mechanical properties of the E-MA ionomers might be also ascribed to the structure of the non-ionic polymethylene phase as well as that of the ionic phase, since the non-ionic phase occupies major part of the samples. Therefore, it is of importance to know how the presence of ionic groups affects the structure of the non-ionic polymethylene phase and how the structure is related to the bulk mechanical properties of the ionomers.

In order to solve the problems, it is desirable to investigate structural transition behaviors of crystalline low-molecular-weight compounds as model compounds of E-MA ionomers, having ionic groups and non-ionic polymethylene chains in an individual molecule. A series of quaternary N,N'-dialkyl-1,4-diazabicyclo(2,2,2)octane (DABCO) halides having quaternary ammonium ions and alkyl chains in a molecule is one of them.

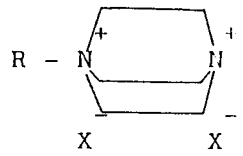

$R = C_nH_{2n+1}$

$X = Br, Cl, I$

The compounds were synthesized by Nogami et al. of Osaka

University in 1985-1986.[27-31] Although low molecular weight and polymeric homologous series of the compounds were synthesized early by Abbiss and Mann in 1964,[32] and Salamone and Snider in 1970,[33] respectively, systematic studies about the thermal and electric properties of the compounds were first done by Nogami et al. They found a first order solid state phase transition of them accompanied by an abrupt increase in halide anion conductivity by two to three orders of magnitude on heating the sample. The transition was explained in terms of the conformational change of the alkyl chains of the molecule from x-ray powder diffraction and IR measurements, while the detailed structural transition behavior is still not clarified.

In ionic polymers including ionomers, the occurence of microphase separation to ionic and non-ionic domains has been often found out. To investigate the molecular structure in each domain, we need new micro-characterization techniques because of poor feasibility of application of usual structural determination techniques such as x-ray diffraction to these heterogeneous systems. Raman microprobe is useful to measure the spectra of micrometer-size materials. In this technique, the incident laser beam is focused by an objective lens with a large numerical aperture value and the backward scattered light is collected by the same objective. This was developed in 1975 by Rosasco et al.[34] and Delhaye et al.,[35,36] independently. Compared with the electron microprobe, the Raman microprobe has an advantage of studying samples in air, at any specified temperature, or even inside transparent media besides in vacuum[36] and suitable for structural study on the microdomain systems. Although the

technique has been extensively used for such as biological substances and mineral inclusions,[37-47] the method of quantitative analysis of the spectrum is still not developed.

In this thesis, the molecular structures and their transition behaviors were studied for the above two kinds of ion-containing long-chain compounds by means of vibrational spectroscopy (IR and Raman) and small angle x-ray scattering (SAXS). In addition, some fundamental problems in the analysis of the micro-focus Raman spectroscopy as a new technique for the microcharacterization of microdomain structures were dealt with. The thesis consists of the following six chapters.

Chapter 1 deals with the molecular mechanism of enhanced elastic moduli of ionomers. The author examined the melting behaviors of an E-MA-Na and an E-MA-Zn in comparison with that of an non-ionic low density polyethylene. With Brillouin scattering technique[18] the temperature dependence of an elastic constant of each sample was measured in the temperature range covering both sloid and liquid states. Structural changes in the non-ionic as well as ionic parts were investigated in the same temperature range with IR and Raman spectroscopy in order to correlate change in the elastic constant to that in the structure.

In chapters 2 and 3, the structure of the ion aggregate in an E-MA-Zn ionomer was investigated The effect of water absorption on the structure of the ion aggregate in an E-MA-Zn was studied, since generally in ionomers a little amount of water in the specimen interacts with ionic groups and changes their

physical properties significantly. By means of SAXS and IR techniques the dimensional and local structural change of the ion aggregate on water absorption was investigated.

In chapter 4, the structural transition behaviors of series of N,N'-dialkyl-1,4-diazabicyclo(2,2,2)octane halides and 1-alkyl-4-aza-1-azoniabicyclo(2,2,2)octane bromides as model compounds of E-MA ionomers were studied by Raman and IR spectroscopy. The changes in the subcell packing and conformational order of the alkyl chains of the substances on the transition were investigated. Rotational reorientational motion of the bicycloring group was also investigated, Based on the result, the role of the ionic group in the structural transition behaviors of the non-ionic methylene chain in crystalline phase was discussed.

In chapter 5, Raman microprobe method as a new technique for polarization measurement of microdomain structures was dealt with. The basic problems of spatial resolutions and polarization analysis in the Raman microprobe were solved.

Chapter 6 summarizes the principal results and conclusions obtained from the present investigation.

References

1) H. P. Brown, Rubber Chem. Tech., 30, 1747 (1957).

2) W. E. Fitzgerald and L. E. Nielsen, Proc. R. Soc., A282, 137 (1964).

3) R. W. Rees and D. J. Vaughan, Am. Chem. Soc. Polym. Prepr., 6, 287 (1965).

4) R. W. Rees and D. J. Vaughan, Am. Chem. Soc. Polym. Prepr., 6, (1965).

5) L. Holliday, Ed., "Ionic Polymers", Applied Science Publishers, London, 1975.

6) A. Eisenberg and M. King, "Ion-Containing Polymers", Academic Press, New York, 1977.

7) W. J. MacKnight and T. R. Earnest, Jr., J. Polym. Sci., Macromol. Rev., 16, 41 (1981).

8) A. D. Wilson and H. J. Prosser, Ed., "Developments in Ionic Polymers -1", Applied Science Publishers, London, 1983.

9) A. D. Wilson and H. J. Prosser, Ed., "Developments in Ionic Polymers -2", Elsevier Applied Science Publishers, London, 1986.

10) M. Pineri and A. Eisenberg, Ed., "Structures and Properties of Ionomers", NATO ASI Series. Series C, vol.198, D. Reidel Publishing Company, Dordrecht, Holland, 1987.

11) R. Longworth and D. J. Vaughan, Nature, 218, 85 (1968).

12) C. T. Meyer and M. Pineri, J. Polym. Sci., Polym. Phys. Ed., 16, 569 (1978).

13) M. Pineri, C. Meyer, A. M. Levelut, M. Lambert, J. Polym. Sci., Polym. Phys. Ed., 12, 115 (1974).

14) J. Yamauchi and S. Yano, Macromol. Chem., 179, 2799 (1978).

15) S. Yano, H. Yamashita, H. Matsushita, K. Aoki, and J. Yamauchi, Colloid Polym. Sci., 259, 514 (1981).

16) J. Yamauchi and S. Yano, Macromolecules, 15, 210 (1982).

17) H. A. Davis, R. Longworth, and D. J. Vaughan, Am. Chem. Soc. Polym. Prepr., 9, 515 (1968).

18) C. L. Marx, J. A. Koutsky, and S. L. Cooper, J. Polym. Sci., Polym. Lett. Ed., 9, 167 (1971).

19) P. J. Phillips, J. Polym. Sci., Polym. Lett. Ed., 10, 443 (1972).

20) F. C. Wilson, R. Longworth, and D. J. Vaughan, Am. Chem. Soc. Polym. Prepr., 9, 505 (1968).

21) B. W. Delf and W. J. MacKnight, Macromolecules, 2, 309 (1969).

22) R. J. Roe, J. Phys. Chem., 76, 1311 (1972).

23) F. L. Binsbergen and G. F. Kroon, Macromolecules, 6, 145 (1973).

24) C. L. Marx, D. F. Caulfield, and S. L. Cooper, Macromolecules, 6, 344 (1973).

25) J. Kao, R. S. Stein, W. J. MacKnight, W. P. Taggert, and G. S. Cargill, III, Macromolecules, 7, 95 (1974).

26) W. J. MacKnight, W. P. Taggert, and R. S. Stein, J. Polym. Sci., Polym. Symp., 45, 113 (1974).

27) J. Shimizu, T. Nogami, and H. Mikawa, Solid State Commun., 54, 1009 (1985).

28) J. Shimizu, K. Imamura, T. Nogami, and H. Mikawa, Bull. Chem. Soc. Jpn., 59, 1443 (1986).

29) K. Imamura, J. Shimizu, and T. Nogami, Bull. Chem. Soc. Jpn., 59, 2699 (1986).

30) J. Shimizu, K. Imamura, T. Nogami, and H. Mikawa, Bull. Chem. Soc. Jpn., 59, 3367 (1986).

31) K. Imamura, T. Nogami, and Y. Shirota, Bull. Chem. Soc. Jpn., 60, 111 (1987).

32) T. P. Abbiss and F. G. Mann, J. Chem. Soc., 2249 (1964).

33) J. C. Salamone and B. Snider, J. Polym. Sci., A8, 3495 (1970).

34) G. J. Rosasco and E. S. Etz, Res. Dev. Mag., 28, 20 (1977).

35) M. Delhaye and P. Dhamelincourt, J. Raman Spectrosc., 3, 33 (1975).

36) P. Dhamelincourt, F. Wallart, and M. Leclercq, A. T. N. Guyen, and D. O. Landon, Anal. Chem., 51, 414A (1979).

37) G. J. Rosasco, E. Roedder, and J. H. Simmons, Science, 190, 557 (1975).

38) G. J. Rosasco, E. S. Etz, and W. A. Cassatt, Appl. Spectrosc., 29, 396 (1975).

39) J. J. Blaha, G. J. Rosasco, and E. S. Etz, Appl. Spectrosc., 32, 292 (1978).

40) J. L. Abrahamson and E. S. Etz, Science, 206, 716 (1979).

41) H. S. Bennet and G. J. Rosasco, J. Appl. Phys., 49, 640 (1978).

42) J. J. Blaha and G. J. Rosasco, J. Raman Spectrosc., 11, 75 (1981).

43) H. Ishida and A. Ishitani, Appl. Spctrosc., 37, 450 (1983).

44) F. F. M. de Mul, A. G. M. van Welle, C. Otto, J. Mud, and J. Breve, J. Raman Spectrosc., 15, 268 (1984).

45) P. Gard, F. Cruegel, C. Sourisseau, and O. Gorochov, J. Raman Spectrosc., 17, 283 (1986).

46) K. Furuya, Oyo Buturi, 50, 1049 (1981).

47) A. Ishitani, "Raman Microprobe", Sekigai-Raman-Shindou, Kagaku no Ryoiki, vol.140, Nanko-do, Co., Tokyo, 1983.

48) M. Kobayashi, T. Kobayashi, Y. Itoh, K. Sato, Bull. Mineral., 109, 171 (1986).

Chapter 1

Brillouin and Raman Study on Melting Process of Ethylene-methacrylic Acid Ionomers

1-1. Introduction

A series of copolymers of ethylene (E) and methacrylic acid (MA), where the MA units are partially or fully neutralized with a cation of such as Na or Zn, is known under the trade name Surlyn of Du Pont de Nemours as one of ionomers. Introduction of small amount of ionized groups into the non-ionic ethylene sequence causes profound changes in mechanical properties of the copolymers: a remarkable increase in elastic modulus as well as in melt viscosity.

In order to elucidate characteristic mechanical behaviors of ionomers from the structural view-point, many studies have been made so far, by means of various methods. The behaviors are thought to be due to aggregations of the ionic groups, called ionic clusters, occuring in the non-ionic matrix of the copolymers. Shape, size, and stability of ionic clusters have been investigated by small angle x-ray scattering (SAXS).[1,2] Infrared and Raman bands ascribed to the vibrations in ionic clusters and smaller aggregates called multiplets have been reported.[3-10] For some specific metal salts neutralized with such as Fe, Cu, and Mn ions Mössbauer and ESR spectroscopies have been used.[2] As for structures of the non-ionized MA groups, equilibrium between free (monomer) and hydrogen-bonded (dimer) states of carboxyl groups has been studied by infrared spectrosocpy.[11-14] Thus, previous workers focused their attention mainly on structures of aggregations of polar groups in ionomers, since they may act as cross-links. In addition to the polar part, structures of the non-polar polyethylene backbones that constitute the major part of the materials are also

important factor in mechanical properties.

In the present chapter, the author investigated relation between the structures and a mechanical property of E-MA ionomers. To this end, changes in an elastic constant and in structures of both ionic and non-ionic parts on the melting process are compared among three polyethylene-based polymers which resemble each other in crystallizability. They are two E-MA ionomers in which a part of the acid groups is ionized by Na or Zn cation denoted by E-MA-Na or E-MA-Zn, respectively, and a low density polyethylene (LDPE) sample as a comparison of non-ionic polymer. The three samples exhibit a low crystallinity of about 10wt% or less.

The temperature dependence of an elastic constant for the three samples is measured in the range from room temperature up to 200^{o}C by Brillouin scattering technique. In contrast with Raman scattering having the wavenumber shifts above several cm^{-1} from an excitation frequency, Brillouin scattering is with the shift below $1cm^{-1}$ (= 30GHz). A shift of the scattering is related to elastic constants of a specimen.[15] The technique has an advantage in ability of measuring elastic constants in a wide temperature range covering both solid and liquid states without break of a sample. Thermally induced structural changes in the non-ionic and the ionic part of the three samples are examined in the same temperature range (Fig.1-1). (a) Temperature dependence of the degree of crystallinity is examined through the intensity of the Raman CH_2 scissoring band. Intensity of the band at $1416cm^{-1}$ of the Ag split component of the CH_2 scis-

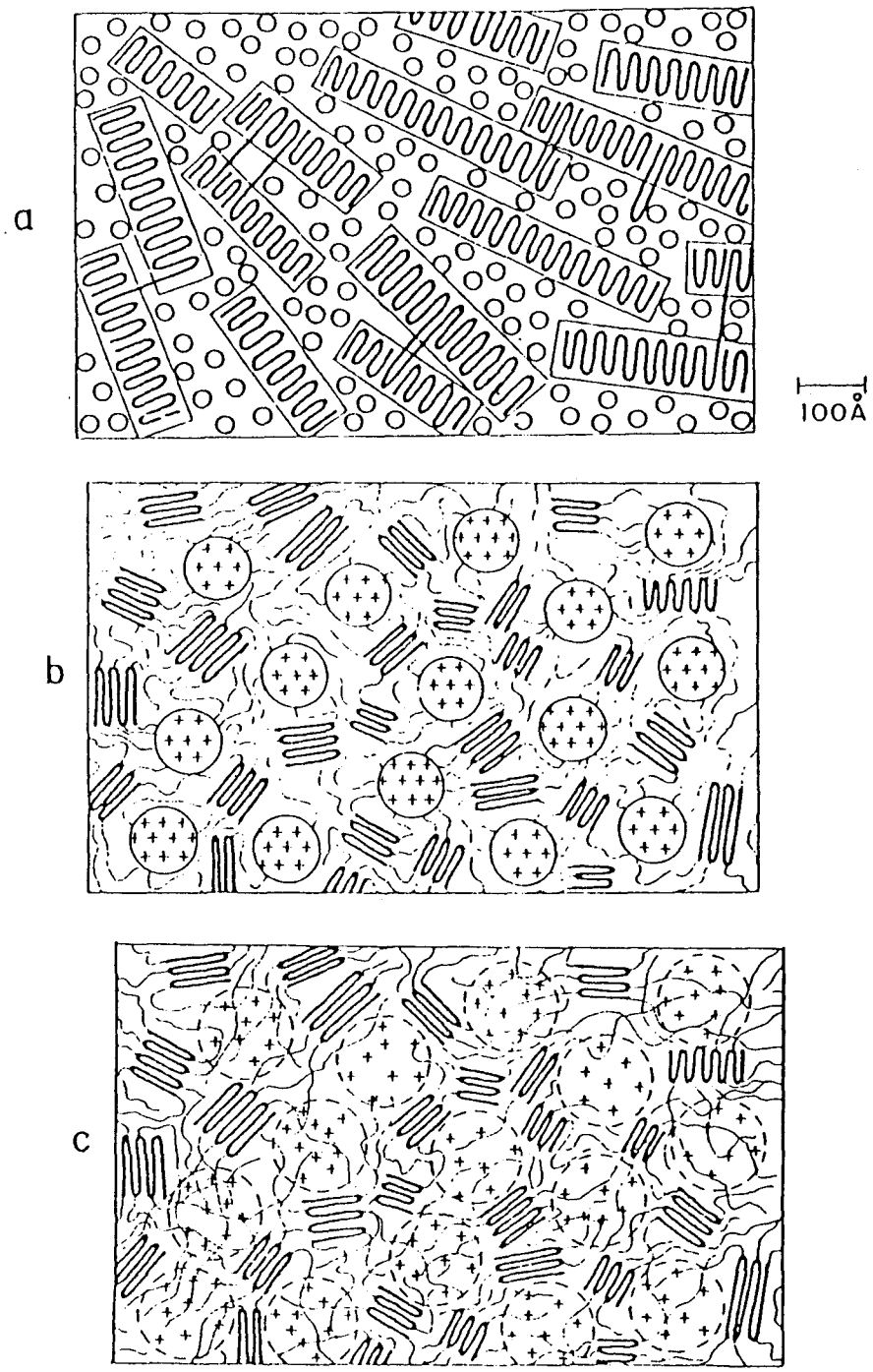

Fig.1-1. Schematic representation of the structure of an ethylene copolymer (a)folded chains of polyethylene segments interspersed with carboxyl groups, (b) the dry ionomer, (c) the wet ionomer (after Longworth and Vaughan, Nature, 218, 85 (1968)).

soring band. Intensity of the band at 1416cm^{-1} of the Ag split component of the CH_2 scissoring mode is proportional to the weight fraction of the polyethylene part carystallized in the orthorhombic form. (b) Conformational order of polyethylene segments in the non-crystalline region is measured with the Raman CH_2 twisting band. Intensity of the 1295cm^{-1} band is proportional to the amount of the methylene sequences $(CH_2)_n$ having all-trans conformation longer than a critical length of $n \geq 6$[16] both in the crystalline and in the non-crystalline region. Temperature dependence of a low-frequency Raman band characteristic of disordered polymethylene chain, named the disordered longitudinal acoustic mode (D-LAM) band,[17] is also investigated. Its intensity, frequency, and band-width have been regarded to be related to conformational order of polymethylene chains in the non-crystalline region. (c) Structural changes in ion aggregates are examined with the IR antisymmetric stretching band of the carboxylate group. Dimer-monomer equilibrium of the non-ionized carboxyl groups is investigate with the IR carbonyl stretching bands of the dimeric and the monomeric group. (d) The temperature dependence of the specific volume ($\bar{V}$) is measured and the relation between $\bar{V}$ and the conformational order of the polymethylene chains is discussed.

1-2. Experimentals

1-2-1. Samples

The ionomer samples of an E-MA-Na (Surlyn 465) and an E-MA-Zn (Surlyn 472) were purchased from Scientific Polymer Products. The acidified samples of them were prepared by dissolving the E-MA-Na and the E-MA-Zn in refluxing tetrahydrofuran (THF) containing the stoichiometric amount of hydrochloric acid. These acidified products were purified by reprecipitation with methanol from THF solution and dried at 50 °C in vacuo for 24h. The contents of methacrylic acid were determined by elementary analysis from the total amount of C of these acidified samples. The degree of neutralization of the E-MA-Na was estimated from the decrease in the integrated absorbance of the carbonyl stretching ν (C=O) infrared band compared with that of the acidified sample and that of E-MA-Zn from atomic absorption analysis for Zn. The LDPE sample (Toughmer A-4085) was supplied from Mitsui Petrochemical Ind. Co., Ltd. Three samples were molten at 150 °C and quenched in liquid N_2. Density measurements were made by the flotation method in methanol-water mixture at 16.0 °C. Variation of the specific volume with temperature was measured by dilatometry. The refractive indices at room temperature were measured on film samples using an Abbe refractometer. The data characterizing the samples are listed in Table I-I.

1-2-2. Brillouin Measurement

The Brillouin scattering experiment was made using a Fabry-Perot interferometer equipped with a pair of corner-cubes for operating in the triple-pass mode. A single-frequency beam of

Table I-I. Characteristics of samples.

$$-(CH_2CH_2)_n-\ (CH_2-\underset{\underset{COOH}{|}}{\overset{\overset{CH_3}{|}}{C}}-)_m-\ (Na^+,\ (Zn^{2+})^{1/2})$$

Sample	Composition n : m	Ionization /%	Density /gcm^{-3}	Refractive Index
E-MA-Na	95.40 : 4.60	11.1	0.955	1.520
E-MA-Zn	94.20 : 5.80	46.8	0.958	1.523
LDPE	100 : 0	——	0.898	1.528

the wavelength of 514.5nm from Ar^+ laser equipped with an ethalon (for getting the single-frequency beam) was used as the incident light. The scattered light was collected at right angle as shown in Fig.1-2 and resolved by the interferometer driven with a set of piezoelectric elements. In the space-fixed Cartesian coordinates (X, Y, Z), the directions of the wavenumber vectors for the incident and scattered lights are defined as parallel to the Y and the X axis, respectively. The measurement was made for the polarization of Y(Z Z)X plus Y(Z Y)X of the Porto notation.[18] The spectral data were accumulated in a multichannel analyzer. The scanning was controlled by a Burleigh DAS-1 system. The free spectral range was set at 18.76GHz and the averaged spectral finess was about 30.

1-2-3. Raman Measurement

Raman measurements of the spectra above $1000cm^{-1}$ were carried out with a JASCO R-500 double monochromator using the 514.5nm excitation beam from an Ar^+ laser. The scattered light at right angle was measured. During each run, the slits were kept constant at 120 μm ($3.8cm^{-1}$). Slight scrambling of polarized planes of both the incident and the scattered light occurred by a little translucency of the samples. To minimize the experimental error caused by the scrambling effect, the band intensity was measured for the two spectra with the incident light polarized parallel and perpendicular to the scattering plane and the averaged value was used as the corrected intensity.[16] The low-frequency (below $400cm^{-1}$) D-LAM band was measured by a JASCO CT 1000D double monochromator with the focal

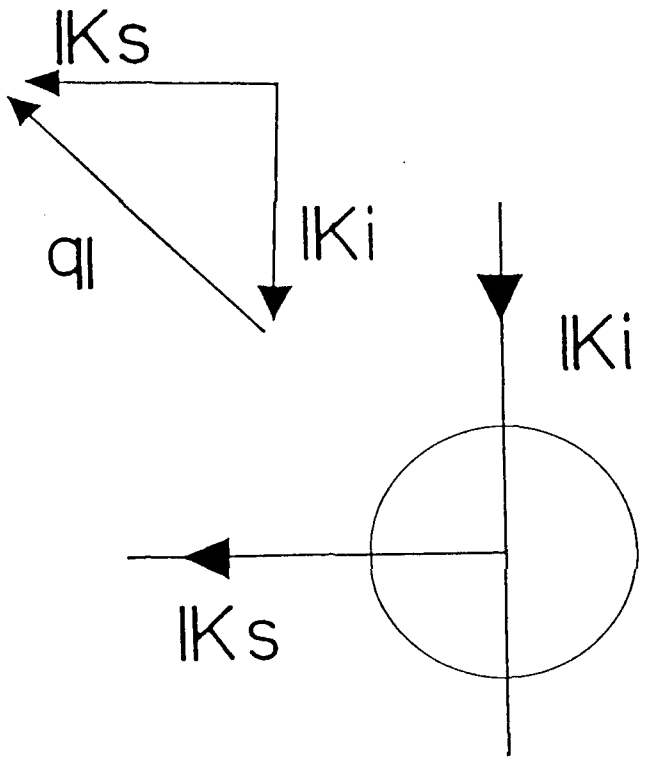

Fig.1-2. Wavenumber vectors of the incident $|K_i$ and scattered light $|K_s$ and the observed phonon $q|$.

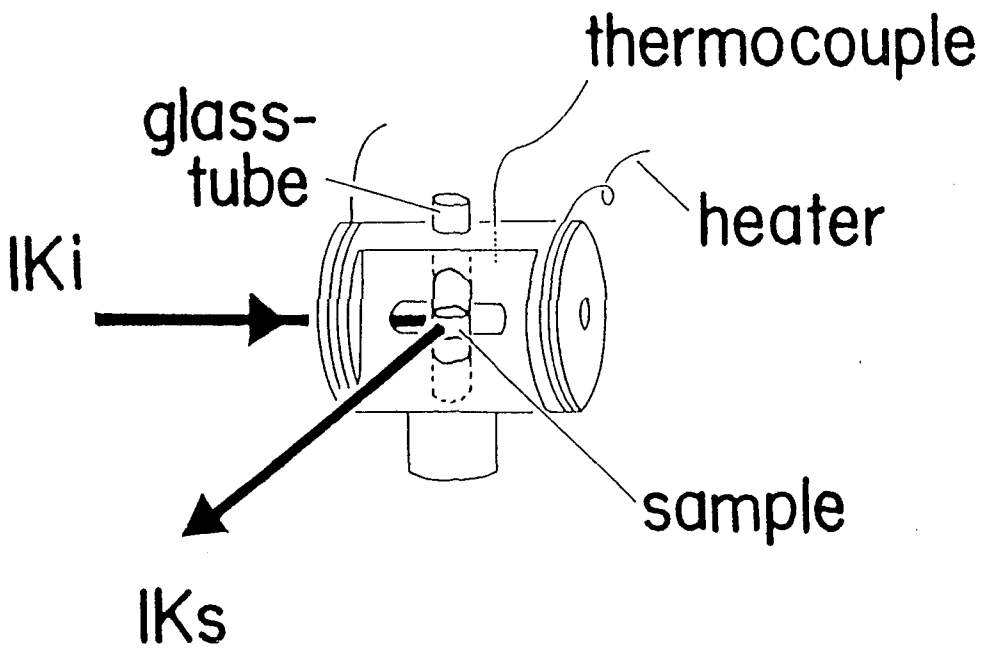

Fig.1-3. High-temperature cell.

length of 1m using the 514.5nm excitation line. A polarization scrambler plate was used to eliminate the polarization effect in the monochromator. The spectra were measured for two geometries of Y(Z Z)X (or p:polarized) and Y(X Z)X (or dp:depolarized).

The Brillouin and Raman experiments at elevated temperatures were performed with a home-made heating cell shown in Fig.1-3. Since extremely high transparency of the sample is necessary for the Brillouin scattering experiment, the polymer was molten in a fluorescence-free quartz tube and quenched in liquid N_2 to minimize the degree of crystallinity (less than 10wt%). The transparent sample thus obtained was set in the cavity of the heating cell whose temperature was controlled within $\pm 0.5^{\circ}$.

1-2-4. Infrared Measurement

Infrared absorption spectra were measured with a JASCO A-3 spectrometer. The slit-width at $1600cm^{-1}$ was $2.6cm^{-1}$. Film samples of about 20 μm of thickness were molded by a hot press with the pressure $100kg/cm^2$ at $150^{\circ}C$, then quenched in liquid N_2. The samples were sandwiched between two KBr windows and set in a heating cell. For the measurement of transmittance above $50^{\circ}C$, the contribution of thermal emission was corrected. A spectrum was recorded at a specified temperature. Temperature change was made with a heating rate of $10^{\circ}C/h$.

1-3. Temperature Dependence of Elastic Constant

Brillouion spectra of the three samples at various temperatures were observed. On the basis of the results the temperature dependence of an elastic constant was investigated.

The observed spectra of E-MA-Zn are reproduced in Fig.1-4. Two pairs of the shifts, one being due to transverse acoustic (TA) mode and the other longitudinal acousitc (LA) mode, are generally observed in an isotropic solid. One pair of bands observed in each spectrum in Fig.1-4 is assigned to the LA mode since the ratio of the intensity of the LA mode to that of the TA mode is very large, e.g., $>10^3$ [19,20]. The TA mode might be smeared in the Rayleigh wing. The Brillouin shift ν_B decreases from 10.30 to 4.60GHz as the temperature increases from 21 to 190 °C and the full-half-linewidth including the instrumental linewidth decreases from 2.0 to 0.9GHz. Substantial difference in temperature dependence of ν_B among the three samples was observed in the temperature region from 20 to 100 °C. In the molten state, the ν_B of the three samples has almost the same frequency, e.g., 5GHz at 140 °C, agrees with that of molten linear polyethylene [21]. For the right-angle scattering, the longitudinal elastic constant E (= C_{11}) is given by [22]

$$E = \rho(\nu_B \lambda_0 / \sqrt{2}\, n)^2 \qquad (1\text{-}1)$$

where λ_0 is the incident wavelength in vacuo, ρ the density, and n the refractive index of the sample. The temperature dependence of ρ was measured by dilatometry. That of n was neglected and the value of n measured at 16.0 °C was used.

The E values (in GPa) for the three samples deduced with eq 1-1 decrease with an increase of temperature as shown in Fig.1-5. For the case of E-MA-Na, E shows a plateau in the range of 60 - 90 °C followed by a sharp depression at 100°C (the melting point of

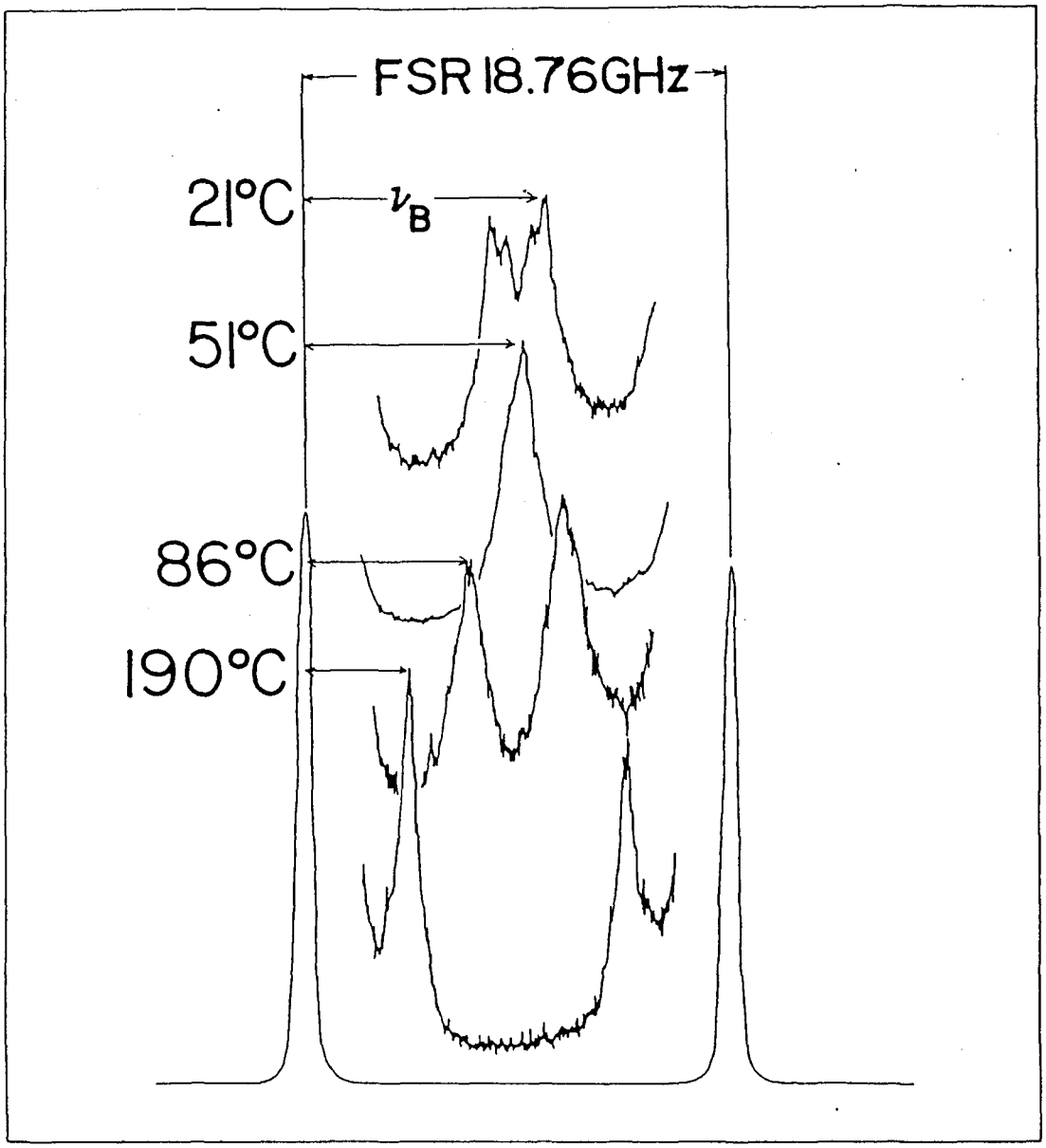

Fig.1-4. Brillouin spectra of E-MA-Zn at various temperatures. Two side sharp peaks are due to Rayleigh scattering, an inner pair of peaks to Brillouin scattering (LA mode), free spectral range (FSR) = 18.76GHz.

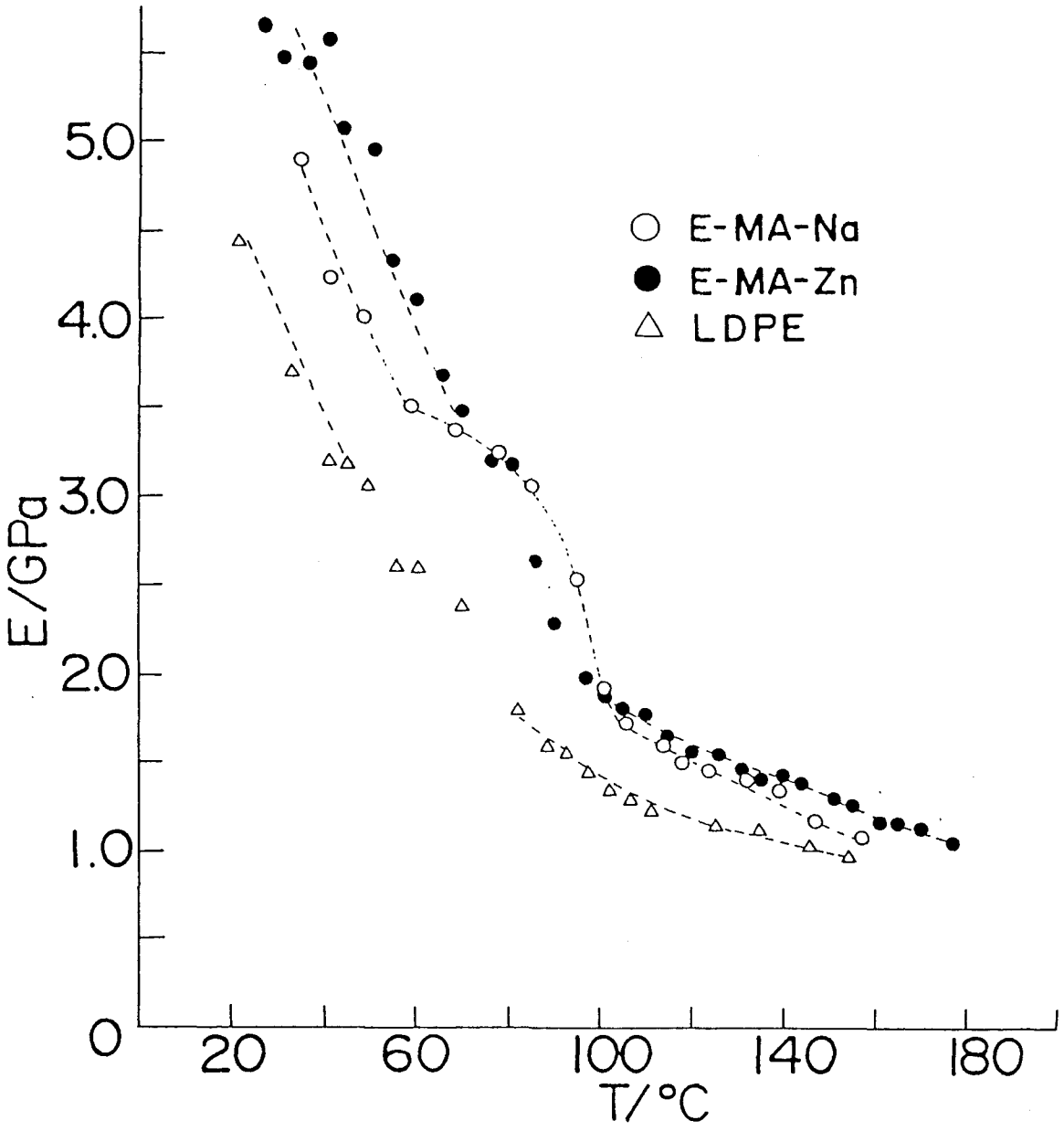

Fig.1-5. Temperature dependence of the elastic constant.

the PE crystallite). The E of E-MA-Zn is greater than that of E-MA-Na below 70 °C, and shows a smaller plateau in the range 70 - 80 °C followed by a sharp depression at 80 °C. In contrast, depression of E of LDPE occurs more gradually in a lower temperature range of 60 - 80 °C without any plateau. Thus, the elastic constant differs appreciably in the range of 70 - 100 °C among the samples. Phenomenologically speaking, the presence of the ionic group prohibits the depression of the elastic constant during the heating process in the ionomers. The aim of the present work is to clarify how the presence of the ionic group influences the structure and its thermal response in various parts of the ionomers and, as a result, changes the behavior of the elastic constant. In what follows structural changes on the heating process in three different parts, i.e. the polyethylene crystallite, the non-crystalline polymethylene segments, and the carboxylate and carboxylic acid groups will be considered based on the spectroscopic results.

1-4. Polyethylene Crystallite

The sharp depression of the elastic constant occurred at about the melting point of the polyethylene crystallite. The crystallites act as cross-linking points and increase the bulk stiffness. Therefore, the degree of crystallinity (the weight fraction of the crystalline part, α_c) is the factor to be first taken into consideration, although α_c of the present three samples is very low (10wt% or less) at room temperature.

Value of α_c can be estimated by x-ray diffraction or density measurement. In the case of polyethylene, α_c is measured

more conveniently with Raman spectrum in the region from 1000 to $1530cm^{-1}$ as shown in Fig.1-6. The bands appearing in the 1400 - $1500cm^{-1}$ region are due to the CH_2 scissoring $\delta(CH_2)$ mode and the small peak at $1416cm^{-1}$ is associated with the orthorhombic lattice of polyethylene. The CH_2 twisting $t(CH_2)$ mode exhibits a sharp band at $1295cm^{-1}$ overlapped with a broad component shifted a little high-frequency side. The sharp component is associated with all-trans methylene segments (both in the crystalline and the non-crystalline phase) and the broad one with segments having random conformation accommodated in the amorphous phase. The total integrated intensity of the sharp + broad components of the $t(CH_2)$ band denoted by $I_{t(CH_2)}$ has been confirmed to be kept constant irrespectively of the states of polymethylene chains and, therefore, used as the internal intensity standard.[23] Strobl and Hagedorn derived an empirical equation that gives α_c value in terms of the reduced intensity of the $1416cm^{-1}$ band reduced to the total intensity of the $t(CH_2)$ band [denoted by I^r_{1416} $(= I_{1416}/I_{t(CH_2)})$] as[23]

$$\alpha_c = I^r_{1416}/0.46 \qquad (1\text{-}2)$$

where 0.46 corresponds to the I^r_{1416} value at $\alpha_c = 1$. The I_{1416} band is separated graphically as indicated in Fig.1-6.

The α_c was evaluated with eq 1-2 for the three samples and plotted against temperature in Fig.1-7. Below 70^oC the curve of E-MA-Zn is located higher than that for E-MA-Na. The curve for LDPE exhibits depression at a low-temperature compared with those of two ionomers. The difference may be related to the difference in the elastic constant below 70^oC (Fig.1-5).

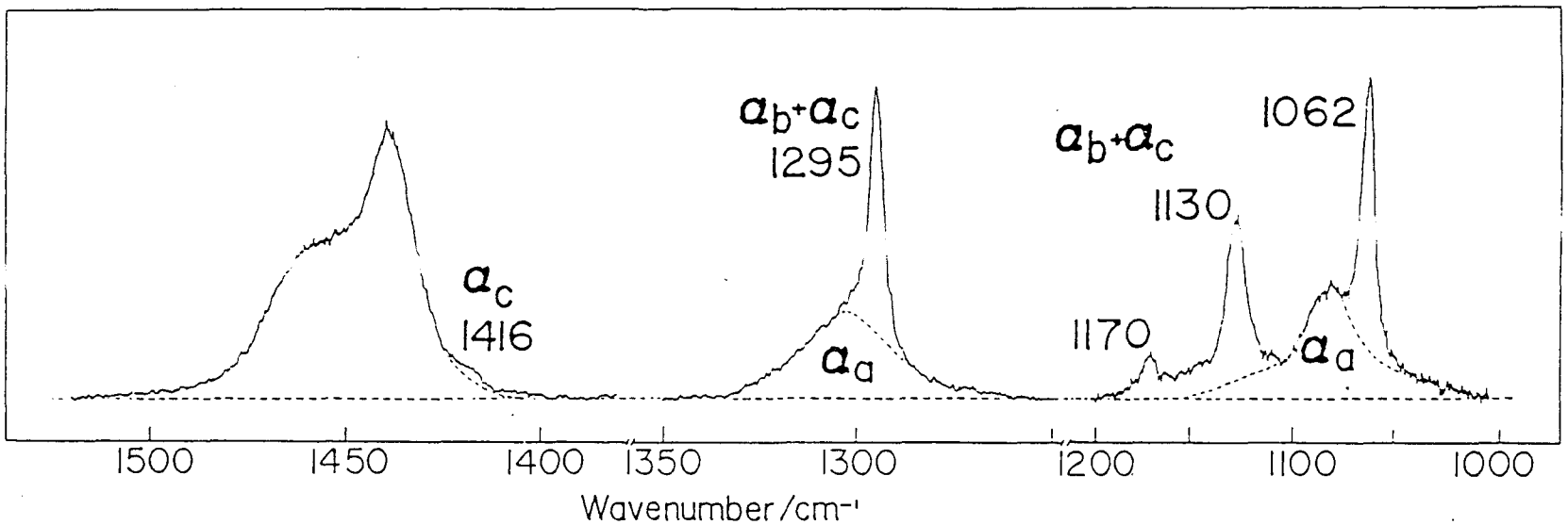

Fig.1-6. Raman spectrum of E-MA-Na measured at 24°C. The weight fraction of α_c is attributed to the intensity of the 1416cm^{-1} Ag split component. The fraction of α_a is to either the intensity of the 1305cm^{-1} broad component or that of the 1080cm^{-1} component. The fraction of $\alpha_c + \alpha_b$ is to either the intensity of the 1295cm^{-1} sharp component or the sum of the intensities of 1062, 1130, and 1170cm^{-1} components.

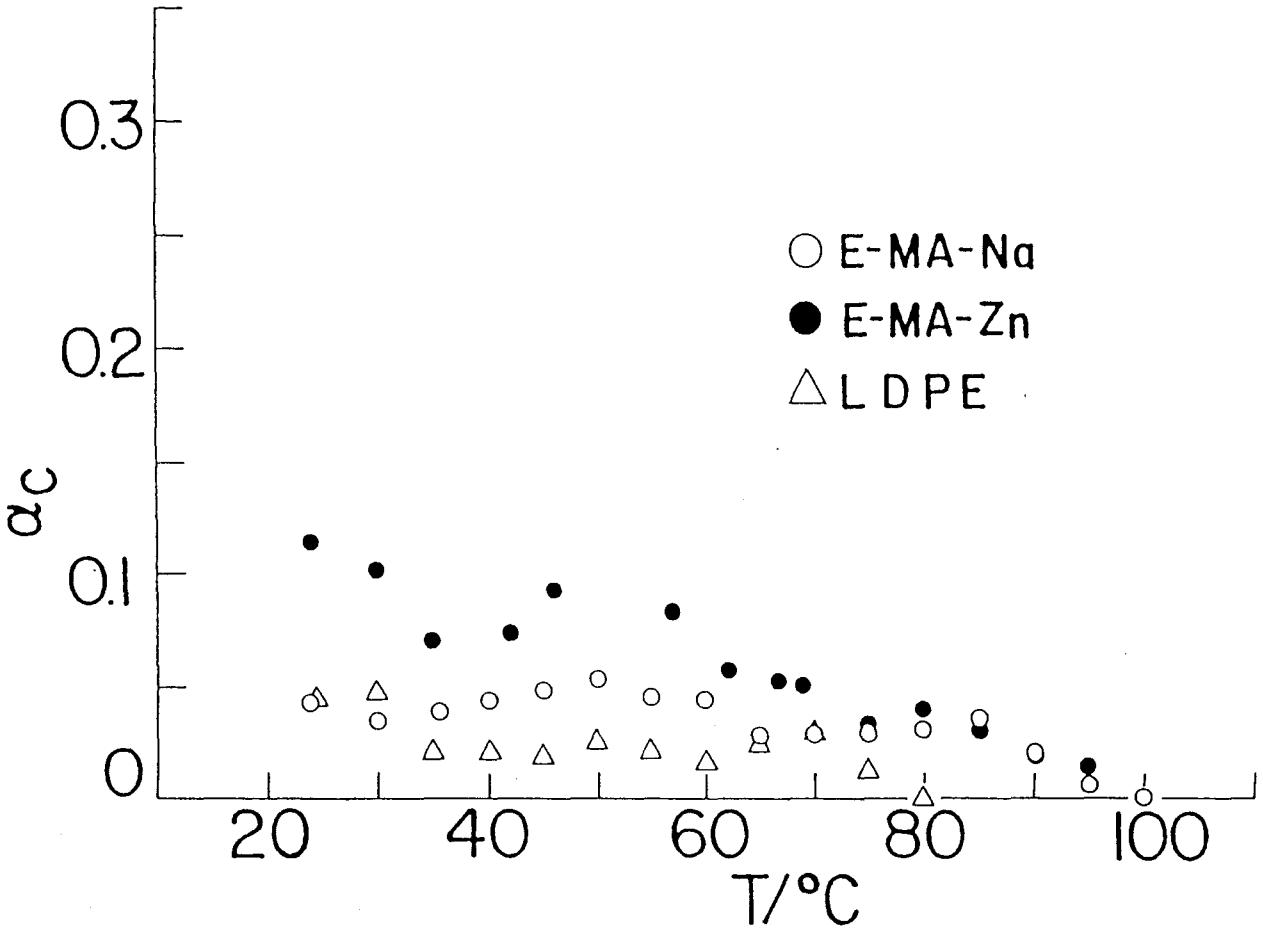

Fig.1-7. Temperature dependence of α_c.

While, no difference is found in the melting behavior of the PE crystallite between E-MA-Na and E-MA-Zn in the temperature region of 70 - 100 °C. In the region, appreciable difference of the elastic constant was observed between E-MA-Na and E-MA-Zn. Therefore the observed difference of the elastic constant between the three samples in the temperature region from 20 to 70 °C can be interpreted by the difference of α_c but that from 70 to 100 °C should not be ascribed to the difference in the melting behavior of the PE crystallite.

1-5. Structural Change of Polymethylene Molecules in Non-Crystalline Phase

The elastic constant C_{11} measured from the LA Brillouin band at a specified temperature is related to the isothermal bulk compressibility of the sample.[24] Therefore the elastic constant might be influenced by the conformations and aggregation states of polyethylene segments in the non-crystalline part which occupies more than 60wt% of each sample. The Raman spectrum of polymethylene chains in the 1000 - 1500cm^{-1} region (Fig.1-6) are sensitive to the conformational order of polymethylene chains both in the crystalline and non-crystalline regions. The sharp bands at 1295 [$t(CH_2)$], 1170 [the CH_2 rocking $r(CH_2)$], and 1130, 1062cm^{-1} [the CC stretching ν_s(CC) and ν_a(CC) bands] are assigned to Raman-active zone center modes (as described in the blackets) of an infinitely extended chain of polyethylene. The intensity of each band is proportional to the amount of the all-trans segments longer than a certain critical length characteristic of each vibrational mode. For example, the

1295cm^{-1} band is due to the all-trans sequences of six or more methylene units, and the 1062cm^{-1} band to those of seven or more units. The extended segments contribute equally to the Raman intensities regardless of whether they are accomodated in the crystalline or in the non-crystalline region.

From the Raman intensities of these characteristic bands the weight fraction of three types of polymethylene segments can be evaluated; 1) long extended chains constructing the crystalline part(α_c), 2) segments having random conformations present in the amorphous phase (α_a), and 3) rather short all-trans segments accomodated in the non-crystalline parts ($\alpha_b = 1 - \alpha_a - \alpha_c$). The third component has been considered conventionally as constructing the third phase named "the intermediate phase". Strobl and Hagedorn[22] proposed a method for deriving the weight fractions of α_a and $\alpha_c + \alpha_b$ from the Raman intensity of the t(CH_2) band based on the assumption that the fraction of the sharp component at 1295cm^{-1} to the total integrated intensity of the t(CH_2) band was equal to $\alpha_c + \alpha_b$. However, by a recent work done by Cho,[16] it has been demostrated that the 1295cm^{-1} component includes the contribution of the short segments in the amorphous phase in addition to those in the crystalline and the intermediate phases.

In the present work, the parameter α_b is used, being obtained through Strobl's method, as the measure of the amount of the trans segments accomodated in the non-crystalline (amorphous plus intermediate) phase. The value of α_b obtained as a function of temperature for the three samples are shown in Fig.1-

8. A remarkable difference was found between those for E-MA-Na and for E-MA-Zn. The α_b value for E-MA-Na is greater than that for E-MA-Zn in the whole temperature range up to 100 °C. A sharp depression of α_b for E-MA-Na and E-MA-Zn takes place in the temperature range of 90 - 100 °C and 80 - 100 °C, respectively. On the contrary, continuous depression of α_b was observed in LDPE. The behavior corresponds well to the temperature dependence of the elastic constant in the range from 70 to 100 °C shown in Fig.1-5. From this close correlation, the author concludes that the variation of the elastic constant of the three samples on heating from 70 to 100 °C reflects mainly the conformational disordering process of the polymethylene chains in the non-crystalline phase.

The elastic constant of E-MA-Zn is higher that that of E-MA-Na below 70 °C (Fig.1-5). This is due to the difference of α_c as described in section 1-4 (Fig.1-7). While the reverse trend is observed from 70 to 100 °C, i.e., the elastic constant of E-MA-Na is higher than that of E-MA-Zn. This is interpreted by the difference of α_b. It is noted that, although α_b in E-MA-Na is greater than that in E-MA-Zn in whole temperature range, the elastic constant of E-MA-Na has low value than that of E-MA-Zn below 70 °C. These indicate that α_c plays dominant role in enhancing the elastic constant. In the case that the specimen has low α_c below 5% (from 70 to 100 °C), α_c contributes to the increase of the elastic constant. The decrease in $\alpha_b + \alpha_c$ corresponds to the increase of α_a ($= 1 - \alpha_b - \alpha_c$). The values of α_a are compared among the three samples in Fig.1-8.

In order to confirm the disordering process of polyethylene

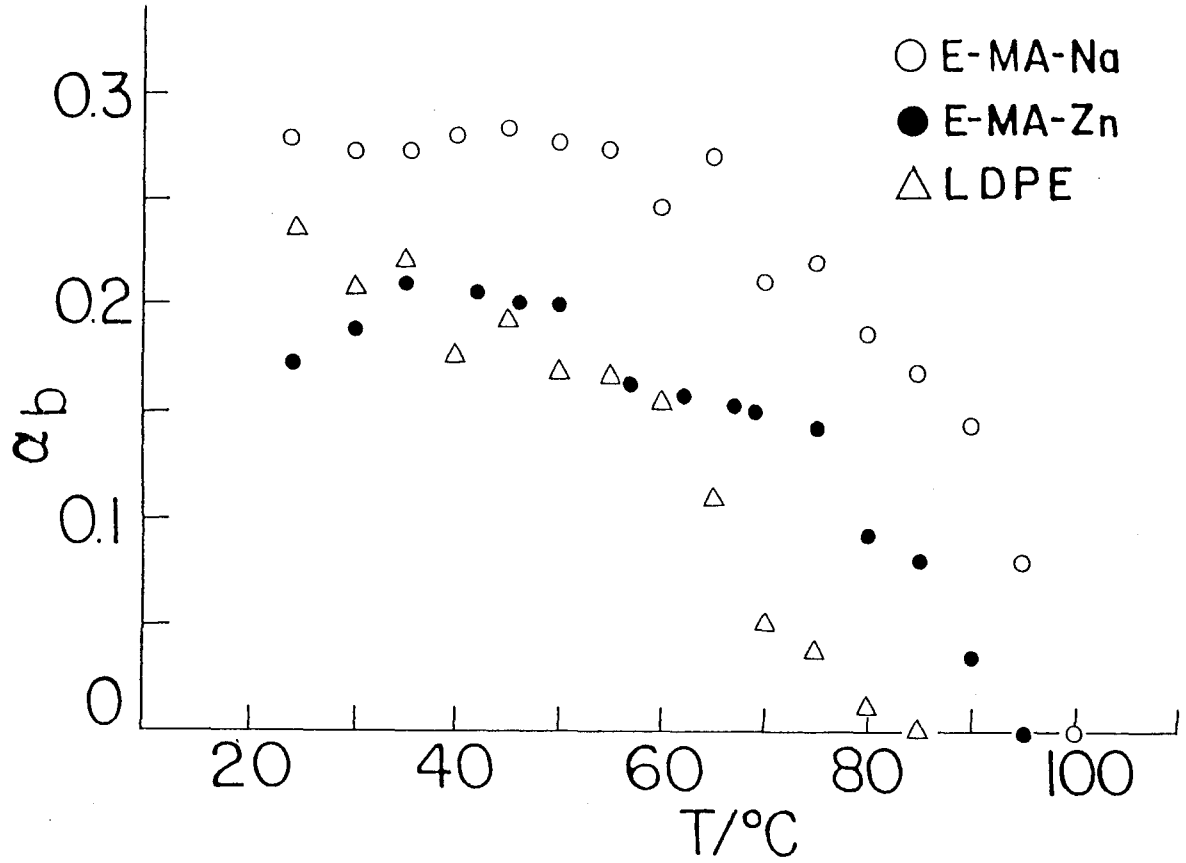

Fig.1-8. Temperature dependence of α_b.

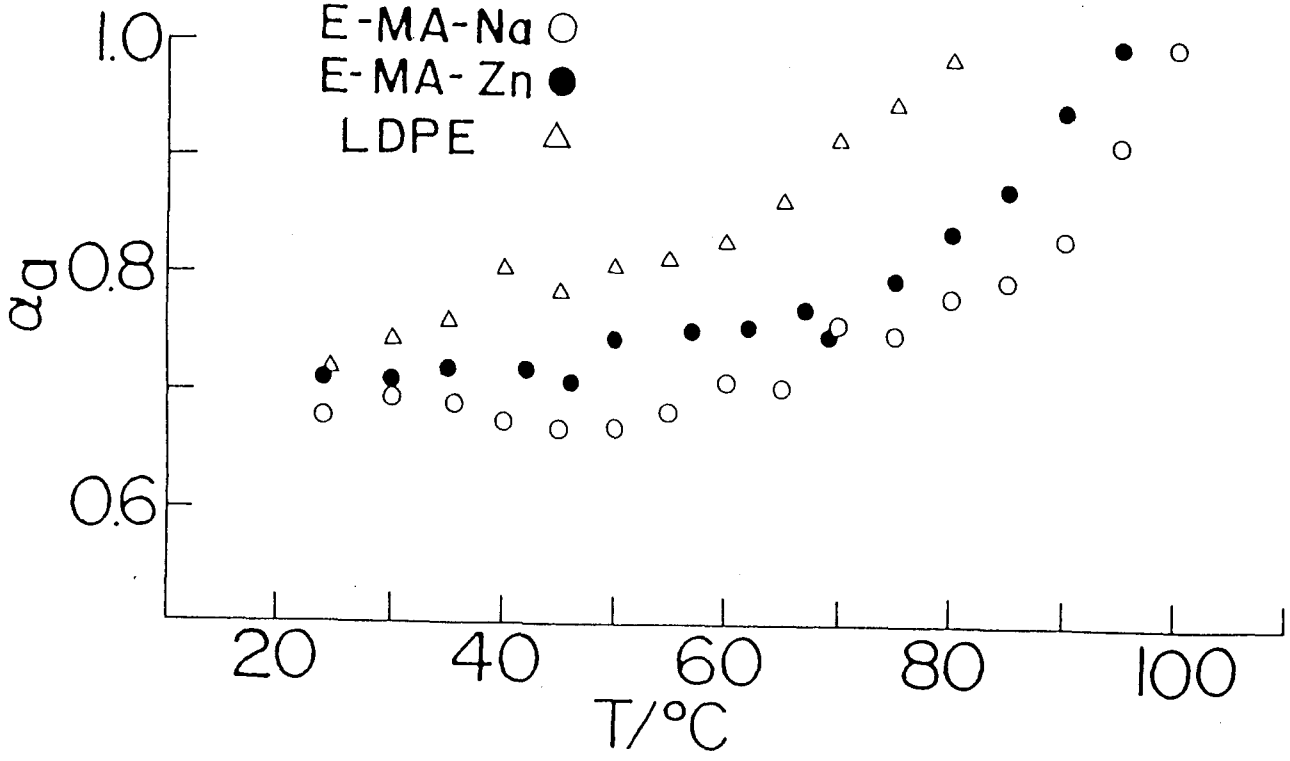

Fig.1-9. Temperature dependence of α_a.

part, another vibrational mode, D-LAM band, that reflects the amount of polymethylene chains having liquid-like conformations was investigated. The band has been found in liquid n-alkanes and molten polymers and considered to be attributed to a coupled skeletal mode of CC stretchning, ∠CCC bending, and ∠CCCC torsional vibrations, of rotational conformers. The integrated intensity of the D-LAM band reduced to that of the internal standard was suggested to be proportional to the α_a.[25] Temperature dependence of the intensity of the band was investigated for the three samples. Fig.1-10 shows the low-frequency Raman spectra of E-MA-Na measured with the p (I_p) and dp (I_{dp}) polarizations at 108 °C. Since the D-LAM band has p-component, the D-LAM band is obtained by subtracting the I_{dp} curve (background) from the I_p curve. From the observed intensity I (= $I_p - I_{dp}$), the scattering activity I' is obtained according to eq 1-3[26]

$$I \propto \frac{(\nu_0 - \nu)^4}{\nu(1 - \exp(-hc\nu/kT))} I' \qquad (1\text{-}3)$$

where ν_0 and ν are the excitation and Raman shift frequencies, respectively, k is the Boltzmann constant, h the Planck constant, T the absolute temperature. The temperature dependences of I_p obtained for E-MA-Na, E-MA-Zn, and LDPE are shown in Figs.1-11 to 1-13, respectively. A band having a peak around 210cm^{-1} was first found by Tsujita et al.[27] and is observed for the present three samples. The temperature dependence of I' is shown in Fig.1-14. The qualitative parallelism was observed for

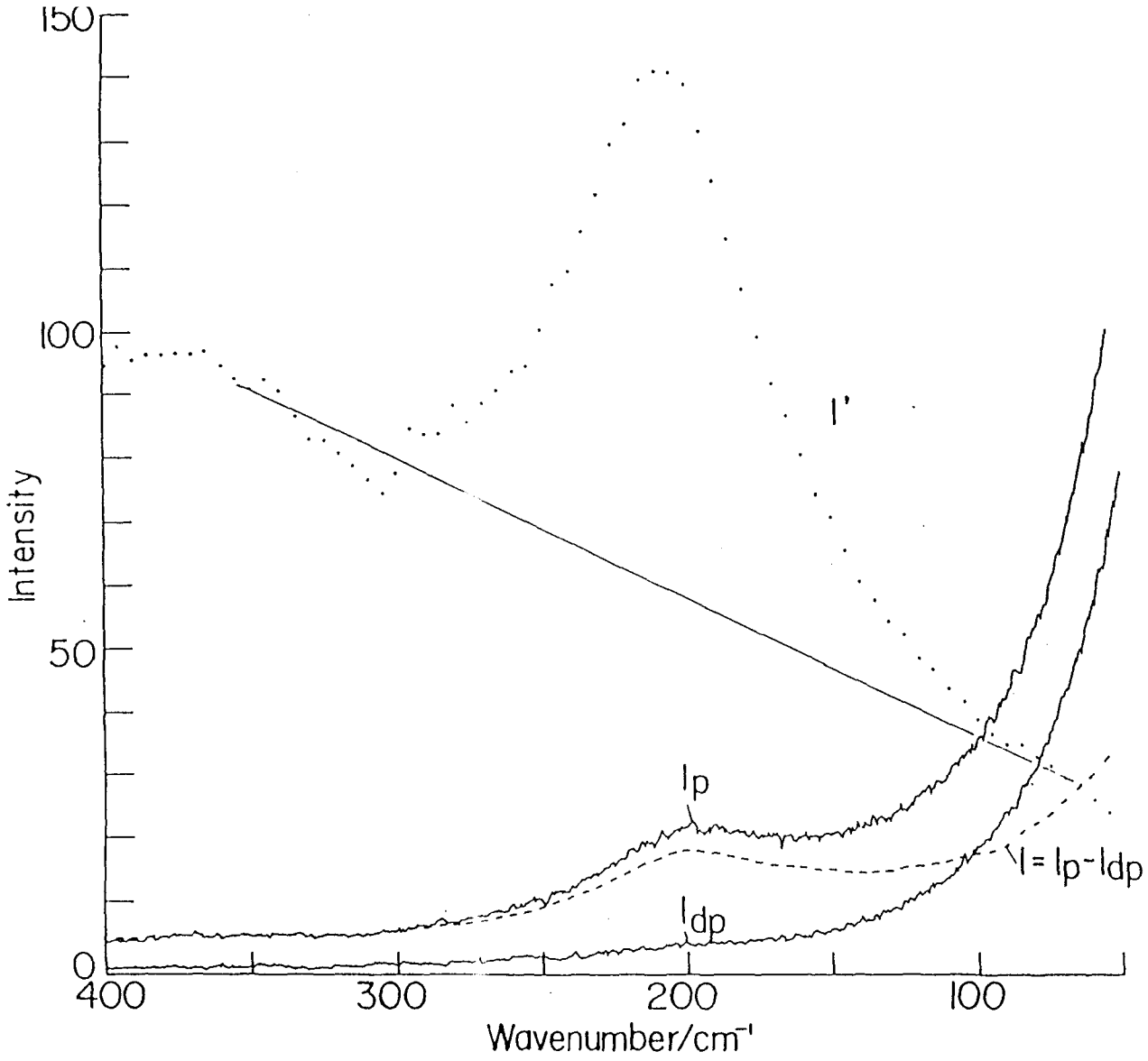

Fig.1-10. D-LAM band of E-MA-Na at 108°C.

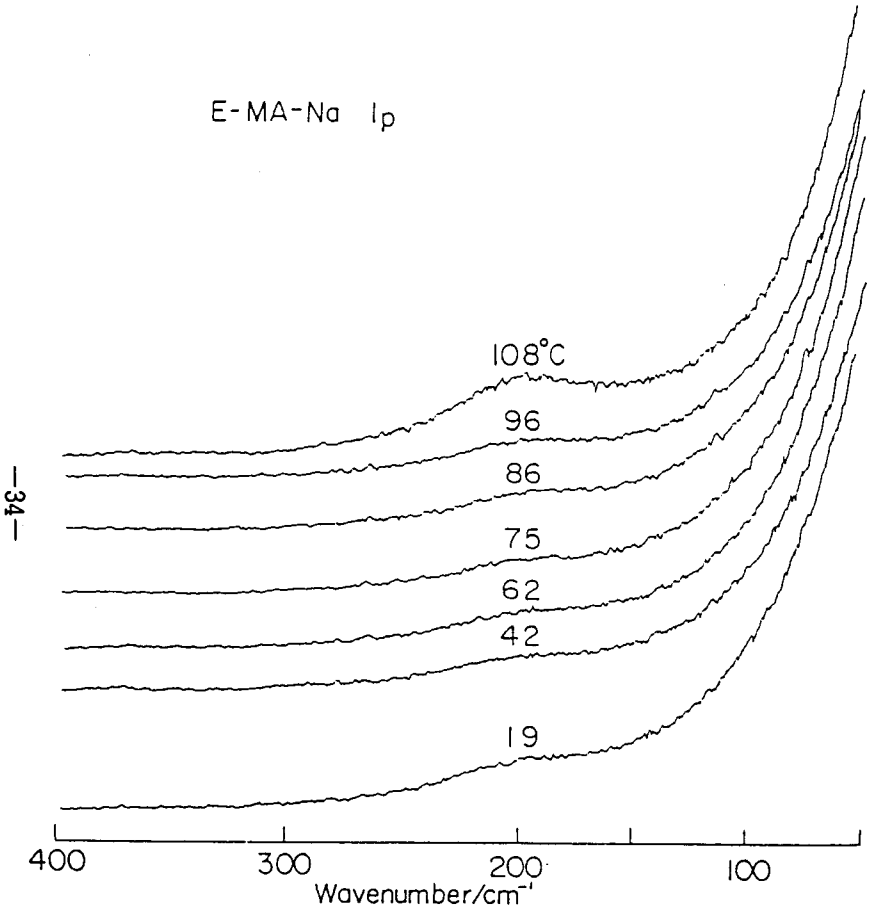

Fig.1-11. D-LAM band of p polarization for E-MA-Na at various temperatures.

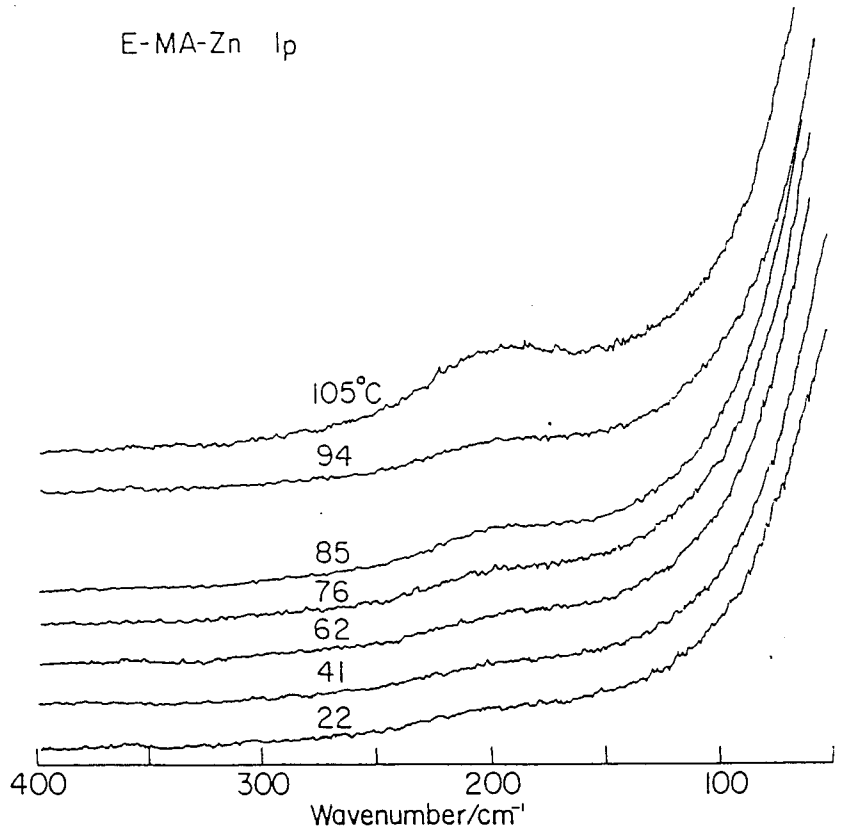

Fig.1-12. D-LAM band of p polarization for E-MA-Zn at various temperatures.

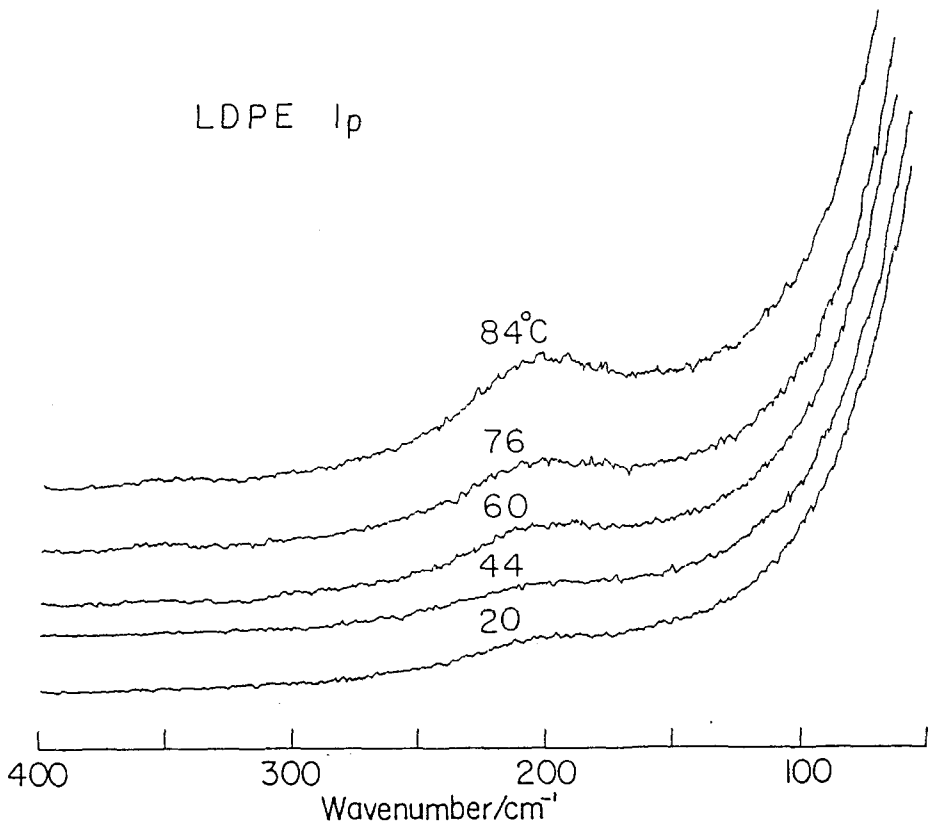

Fig.1-13. D-LAM band of p polarization for LDPE at various temperatures.

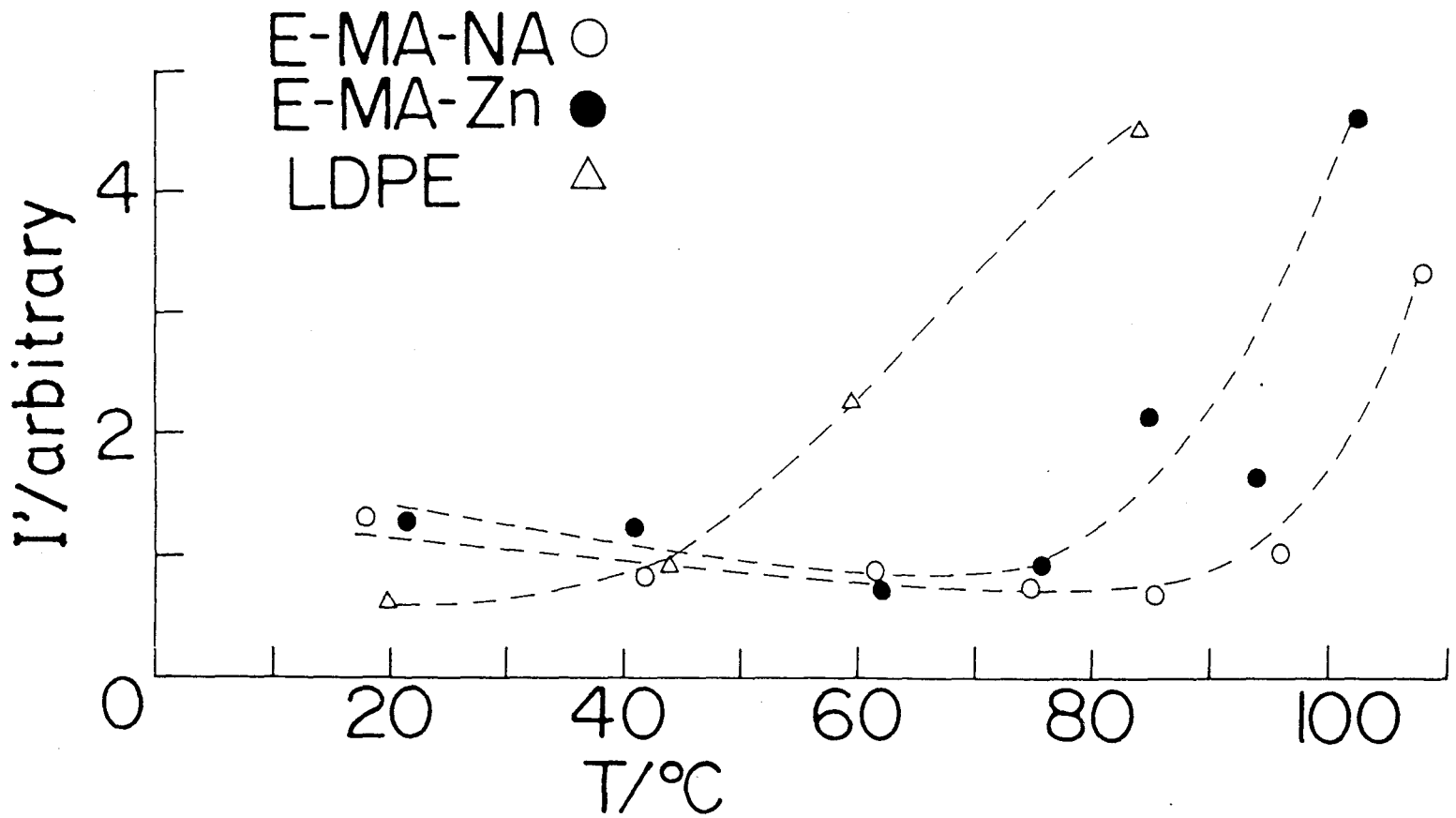

Fig.1-14. Temperature dependence of I'.

temperature dependence of I' and α_a for the three samples. Thus, the value of I' is a measure of the conformational disorder of the polymethylene chains in the non-crystalline phase and, therefore, the present conclusion about the mechanism of the sharp depression of the elastic constant in the temperature range from 70 to 100 °C is confirmed, at least qualitatively, by the behavior of the D-LAM band.

The I' increases sharply by a factor 3 - 4 as α_a increases from 0.7 (at 30 °C) to 1.0 (about the melting point) of each sample. As for the scattering power I' of the D-LAM of semicrystalline PE samples, Mandelkern et al.[28] suggested that I' is proportional to α_a. This is incosistent with the present result. However, their conclusion was derived from the experimental results obtained for the samples with α_a ranging from 0.1 to 0.6. For lower crystalline samples, as in the present case, sharper increase in I' with increase α_a was observed. The present result suggests that the D-LAM intensity is related not only to the total amount of the amorphous phase but also to the "conformational disorder" in the intermediate phase.

1-6. Structural Change of Aggregation of Ionic Groups and Dissociation of Acid Dimer

The structural changes on heating in the ionic and polar part of E-MA-Na and E-MA-Zn are investigated using the IR bands associated with the carboxylate (COO^-) and carbonyl (C=O) groups, and compared with the change in the elastic constant.

Structural change in ion cluster: Fig.1-15 shows the infrared

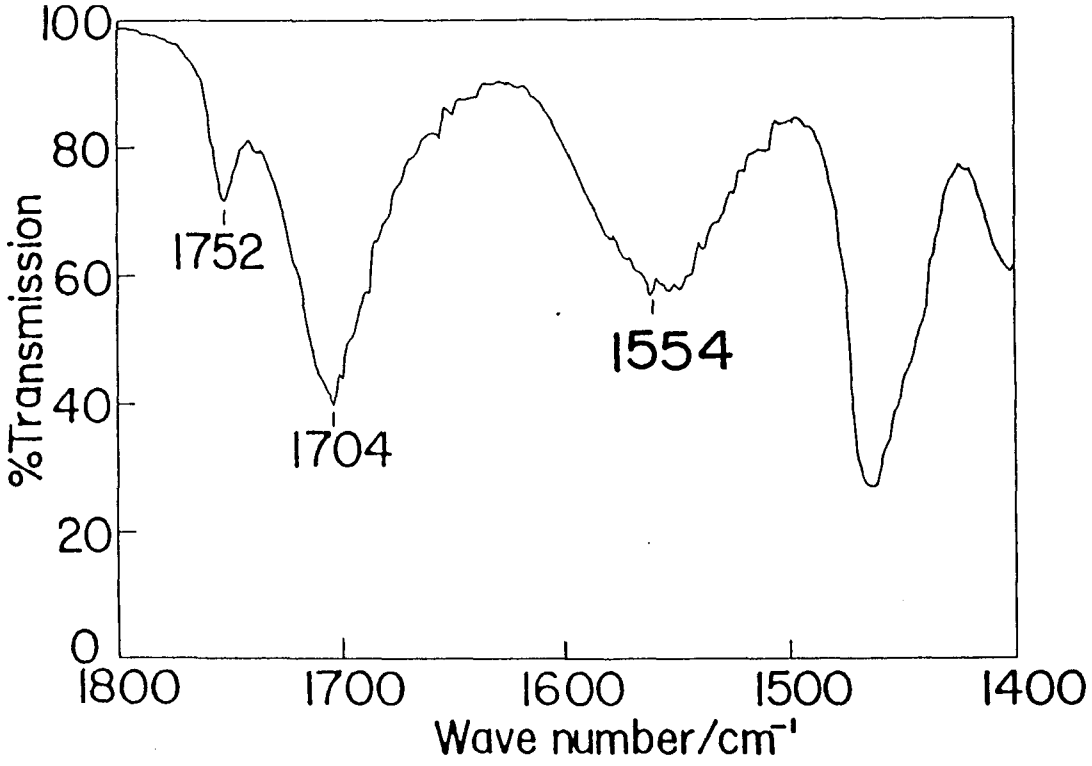

Fig.1-15.Infrared spectrum of E-MA-Na at 170°C.

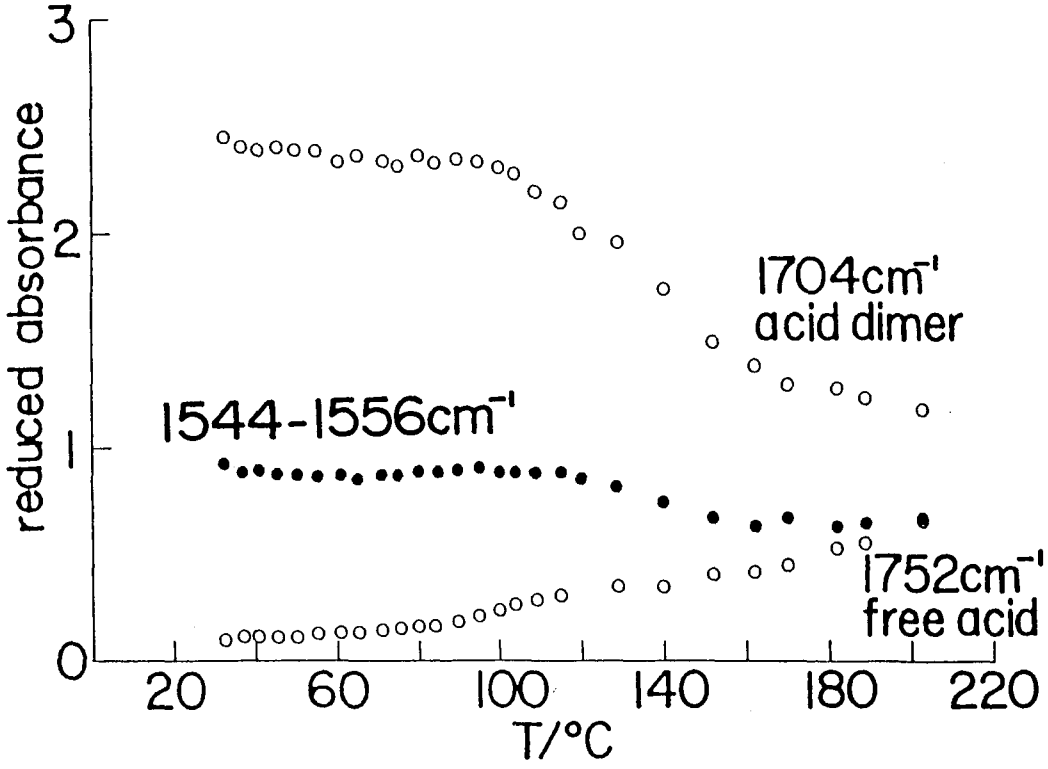

Fig.1-16.Temperature dependence of absorbance of E-MA-Na.

spectrum of E-MA-Na in the range from 1400 to 1800cm^{-1}. A broad band at 1554cm^{-1} is due to the antisymmetric stretching of the carboxylate group $\nu_a(COO^-)$. The peak position shifts from 1544 to 1556cm^{-1} continuously without any splitting as temperature rises from 33 to 183 ^{o}C, contrary to a previous result reported by Brozoski et al.[10] They found that the same band splits into 1547 and 1568cm^{-1} at a dry state and assigned them to the carboxylate groups coordinated octahedrally to the sodium cation. The peak absorbance of the band is temperature independent (Fig.1-16). This suggests that any local structural change in coordination or clustering state of the ionic groups does not occur. For E-MA-Zn, the $\nu_a(COO^-)$ absorption has four components in the 1500 - 1650cm^{-1} region (Fig.1-17). At room temperature, the intensity of the 1587cm^{-1} band is very strong compared with the other three bands at 1625, 1560, and 1539cm^{-1} (Fig.1-18). As temperature rises, the 1587cm^{-1} band decreases in intensity and the others become stronger. This suggests that a local structural change occurs in the ion cluster as will be discussed in chapter 3 in detail. It has been revealed from SAXS experiments that the ion cluster structure in E-MA-Na and E-MA-Zn is persisted up to 300 ^{o}C, far above the melting point of the polyethylene crystallites.

Dimer-monomer equilibrium of the carboxylic acid groups: Two sharp bands at 1704 and 1752cm^{-1} of E-MA-Na (Fig.1-15) are due to the carbonyl stretching $\nu(C=O)$ mode of the unionized carboxyl groups in the dimerized and free states, respectively. As the temperature rises, the intensity of the 1704cm^{-1} band decreases

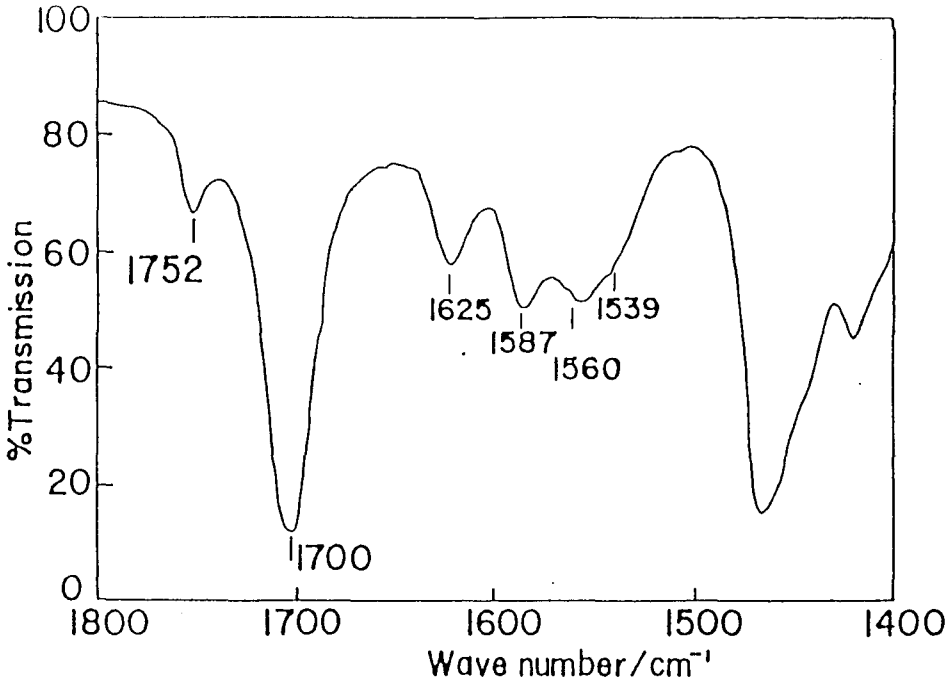

Fig.1-17. Infrared spectrum of E-MA-Zn at 100°C..

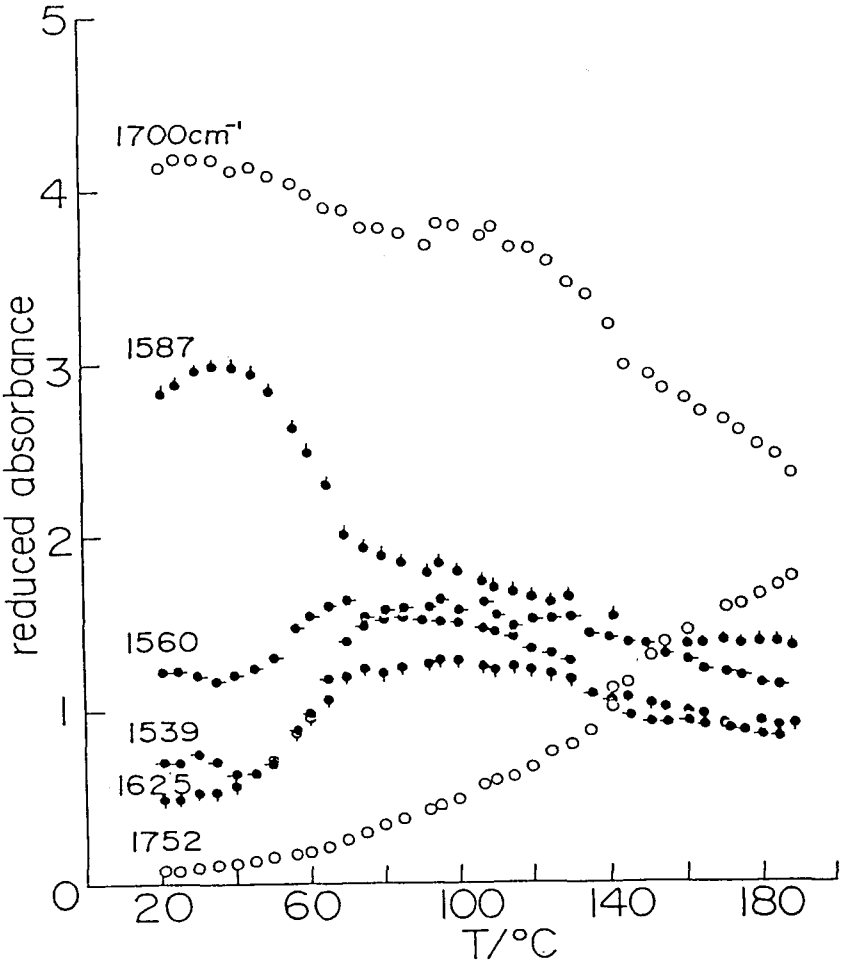

Fig.1-18. Temperature dependence of absorbance of E-MA-Zn.

and that of the 1752cm^{-1} increases through the dissociation of the dimeric groups. Above the melting point of the polyethylene crystallites (100 °C) the dissociation proceeds with rising temperature, giving an inflection point in each absorbance vs. temperature curve of the ν(C=O) bands at about 100 °C (Fig.1-16). Similar inflection was found for the case of Na salts of styrene-methacrylic acid copolymer at the glass transition temperature (T_g) and was attributed to the break down of intermolecular hydrogen bond.[13] From the temperature dependence of the intensity ratio I(1752)/I(1704) above 100 °C, the dissociation enthalpy ΔH of the carboxyl groups is deduced as 47.5kJ/dimer mol from the slope of the van't Hoff plot shown in Fig.1-18. This value is about 11kJ/mol smaller than 59±3kJ/dimer mol of liquid acetic acid measured by Matew and Sheets.[32] Earnest and MacKnight[14] obtained ΔH = 84kJ/dimer mol for an E-MA-Na ionomer. This value seems unusually high compared with the standard value for carboxylic acids (58kJ/dimer mol).[33] The difference between the dissociation enthalpies measured by the present author and by Earnest may be caused by the difference in the content of ionized groups in E-MA-Na ionomers: 0.51mol% by the author and 2.75mol% by Earnest. Similar increase in the dissociation enthalpy with an increase in the content of ionized groups was observed for Na salts of styrene-methacrylic acid copolymers.[13] The increase was from 34 to 36kJ/dimer mol as the content of ionized groups increases from 0 to 2.2mol%. This increase is very small compared with that of E-MA-Na ionomers. Thermodynamical factors causing the difference between E-MA ionomers and styrene-based ionomers are uncertain at the present stage. In E-MA-Zn, the

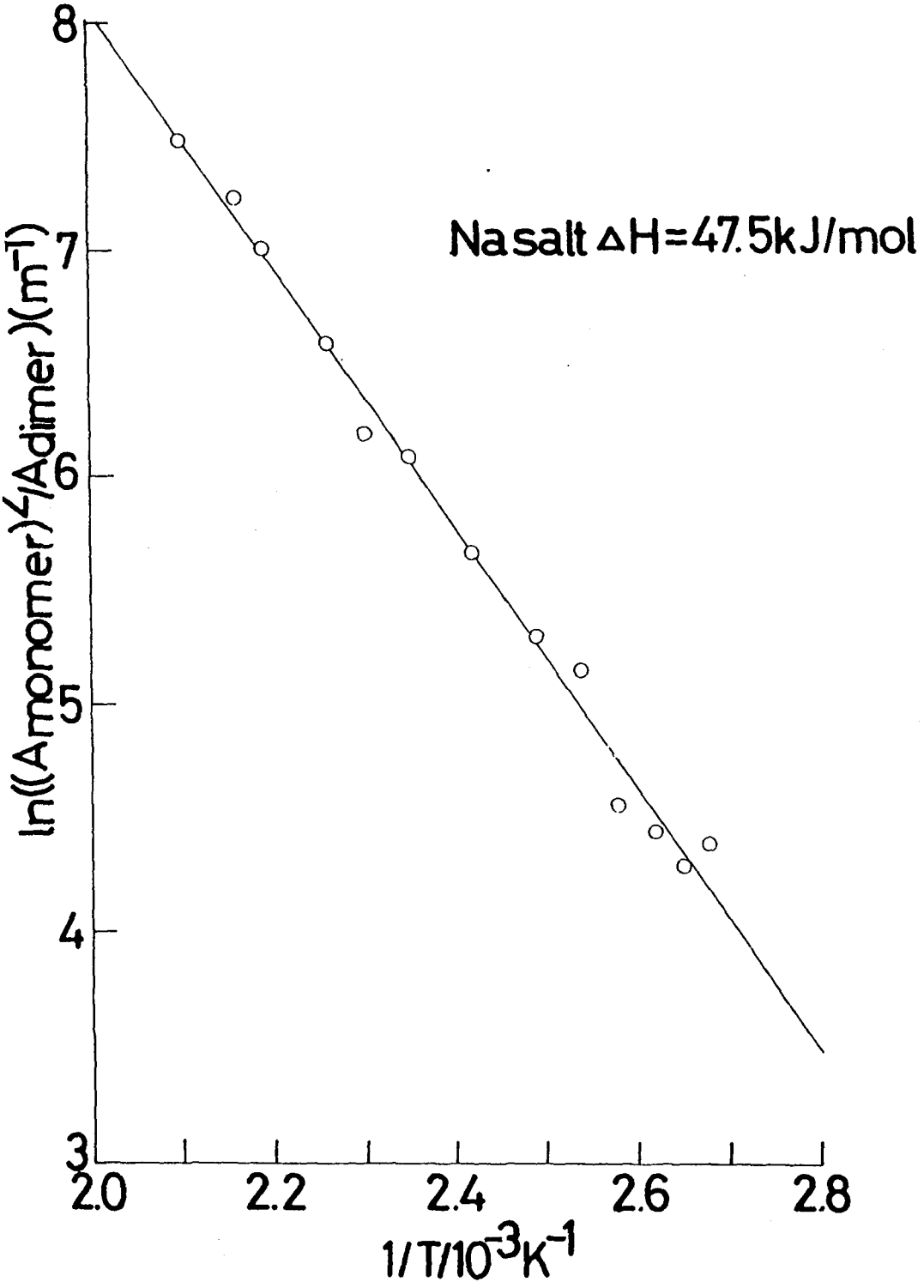

Fig.1-19. van't Hoff plot of E-MA-Na. $A_{monomer}$ and A_{dimer} are the reduced peak absorbances of the monomeric and dimeric ν (C=O) bands, respectively.

dissociation enthalpy was evaluated as 48.6kJ/dimer mol (Fig.1-20) from the intensity ratio of the 1752 and 1700cm^{-1} bands. The inflection point in the temperature depedence of the peak intensity of the dimer band is also slightly discernible but the dissociation occurs rather continuously in the whole temperature range (Fig.1-18).

The spectral changes of the carboxylate and carboxyl groups in E-MA-Na and E-MA-Zn are compared with the changes in the elastic constant. For E-MA-Na no appreciable change corresponding to a structural change in ion aggregates is detected and their melting does not occur in the whole temperature range investigated. The dissociation of the carboxyl dimer is prohibited up to 100 °C. Therefore, the continuous depression of the elastic constant in 20 - 60 °C, the plateau in 60 - 90 °C and the sharp decrease in 90 - 100 °C cannot be ascribed to structural changes in the ion aggregates and the dissociation of hydrogen bonds. In E-MA-Zn, the spectral changes in ion aggregates (due to absorption-desortption of water) occur in the 40 - 70 °C region and further changes are not observed up to 180 °C and again melting of the cluster does not occur up to 180 °C. The dissociation of the carboxyl dimer occurs continuously from 20 to 180 °C. While the elastic constant decreases very gradually from 40 to 70 °C, followed by a small plateau in 70-80 °C and then decreases sharply at 80 °C. Thus it is rather difficult to interpret the characteristic temperature dependence of the elastic constant by the structural changes in ionic and acid parts. Thus, we considered that there

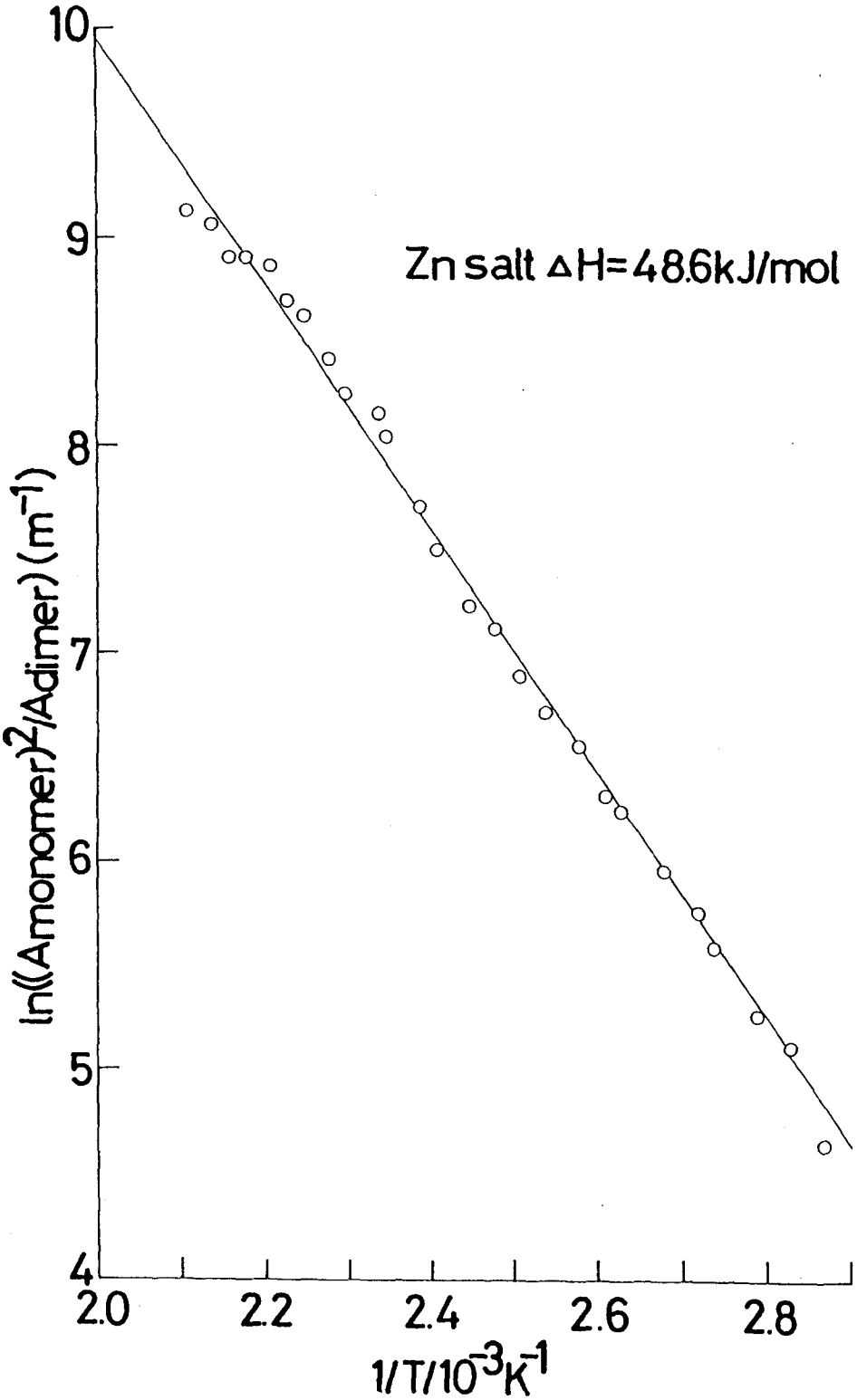

Fig.1-20. van't Hoff plot of E-MA-Zn.

is no correlation between the elastic constant and the dimerization equilibrium of acid groups. This is supported by other studies[34-36] stating that the hydrogen bonding plays a very minor role in determining the mechanical and rheological properties of polymeric acids.

1-7. Temperature Dependence of Specific Volume

It is revealed that in addition to the crystalline phase the intermediate phase plays a dominant role in enhancing the elastic constant of ionomers. The role of the crystalline region as cross-linking points is obvious, while that of the intermediate phase is still ambiguous. Here, correlation between the conformational order of the polymethylene chains and that in the specific volume ($\bar{V}$) was investigated for the three samples. Each sample used was prepared so as to possess almost the same crystallinity as the sample used for the Raman measurement. The temperature dependence of $\bar{V}$ is shown in Fig.1-21. The increase in $\bar{V}$ for the temperature rise from 30 °C to the melting point increases in the order LDPE < E-MA-Zn < E-MA-Na. Since E-MA-Zn has a larger α_c than E-MA-Na at 30 °C (Fig.1-7), the volume increase of E-MA-Zn on the melting of the polyethylene crystallites should be larger than that of E-MA-Na. However, the order of the observed increment of $\bar{V}$ is just reverse. Therefore, contribution of other phases should be considered. A good parallelism was found between $\bar{V}$ and α_a ($= 1 - \alpha_b - \alpha_c$) (Fig.1-9) for each sample. This means that the volume expansion in the melting region might be not dominantly due to the decrease in α_c alone but due to decrease in $\alpha_b + \alpha_c$.

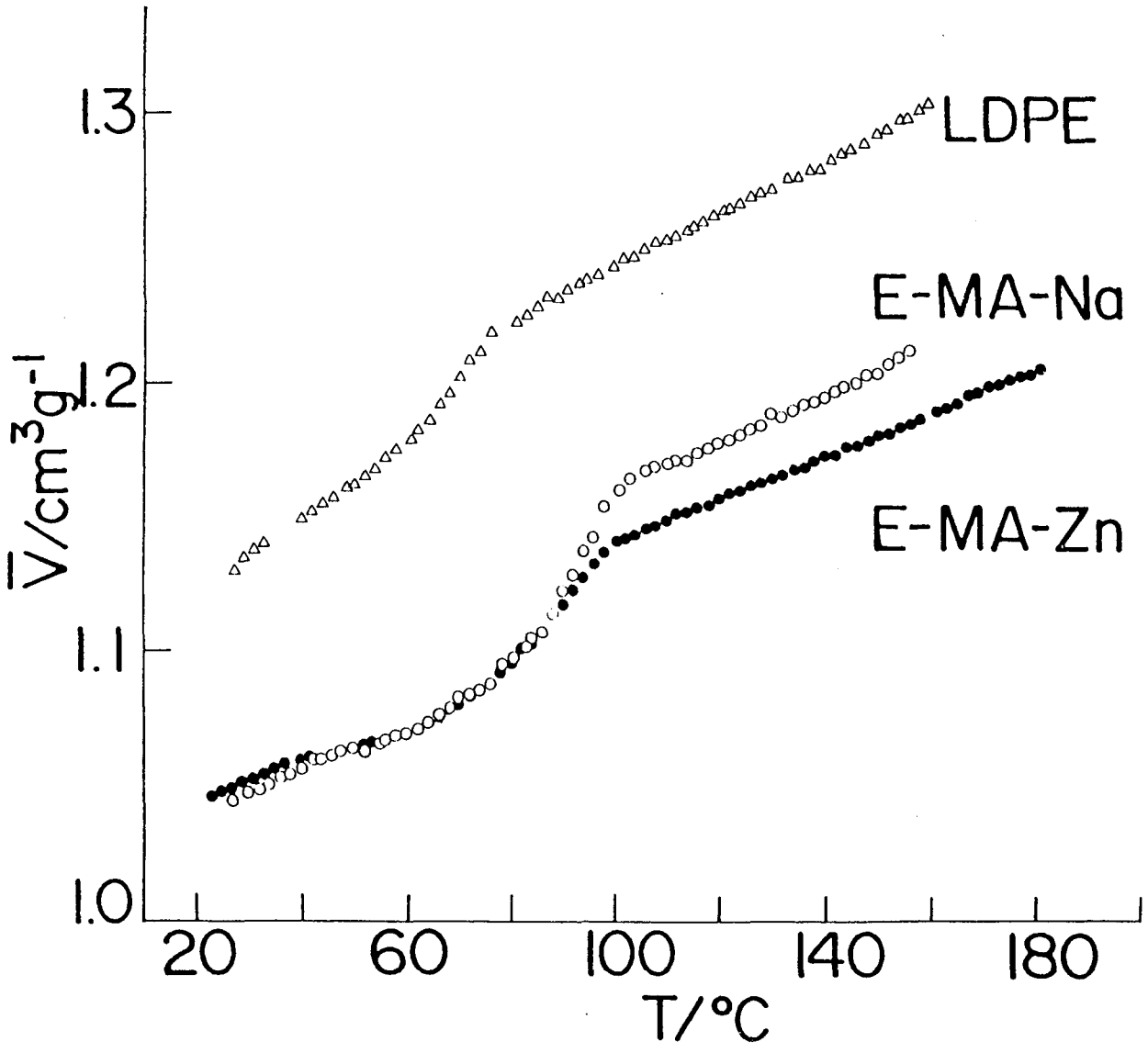

Fig.1-21. Temperature dependence of the specific volume ($\bar{V}$).

In order to reveal the structure of the intermediate phase, the author estimated the specific volume of this phase from $\bar{V}$. Assuming a three-phase-model consisting of the crystalline, the intermediate, and the amorphous phases, $\bar{V}$ is represented as

$$\bar{V} = \alpha_a \bar{V}_a + \alpha_b \bar{V}_b + \alpha_c \bar{V}_c \qquad (1\text{-}4)$$

where $\bar{V}_a$, $\bar{V}_b$, $\bar{V}_c$ are the specific volume of the amorphous, the intermediate, and the crystalline phase, respectively and α_a, α_b, and α_c are the weight fraction of the respective phase which are evaluated from Raman measurement as described above. On the basis of the result of thermal measurement MacKnight et al. indicated that the copolymeric methacrylic acid and the methacrylate groups were not contaminated in the crystalline phase of E-MA ionomers.[37] Thus, $\bar{V}_c$ is assumed here to be identical with that of the polyethylene orthorhombic lattice. The temperature dependence of $\bar{V}_c$ is given as $\bar{V}_c = 1.02+3.00\times10^{-4}$ T/cm^3 g^{-1} where T the temeperature/^oC.[38] Temperature dependence of $\bar{V}_a$ was estimated from linear extrapolation of the observed $\bar{V}_a$ above the melting point of the polyethylene crystallite as $\bar{V}_a = 1.07+9.04\times10^{-4}$ T for E-MA-Na, $1.06+7.85\times10^{-4}$ T for E-MA-Zn, $1.15+9.50\times10^{-4}$ T for LDPE by least squares fitting. It is well known that $\bar{V}_a$ becomes smaller than the values obtained by a linear extrapolation from the melt for ethylene-vinyl acetate and ethylene-acrylic acid copolymers.[39] This factor, 0.974 was multiplied by $\bar{V}_a$ of E-MA-Na and E-MA-Zn. Substituting these values of $\bar{V}_c$ and $\bar{V}_a$, and the weight fractions of α_a, α_b, and α_c into eq.1-4, the temperature dependence of the values of $\bar{V}_b$ were evaluated. The contribution of the copolymeric MA units to

α_a, α_b, α_c was neglected. The obtained values of $\bar{V}_b$ for E-MA-Na, E-MA-Zn, and LDPE averaged in the range from 24 to 50 °C are listed in Table I-II with $\bar{V}_a$ and $\bar{V}_c$.

Comparing the obtained values of $\bar{V}_a$, $\bar{V}_b$, and $\bar{V}_c$, the author considered the structure of the intermediate phase. For LDPE, $\bar{V}_c \lesssim \bar{V}_b < \bar{V}_a$, that is the specific volume of the intermediate phase is close to that in the crystalline phase. This is consistent with the result of Glotin and Mandelkern obtained by Raman and density measurement.[33] This is also the case for E-MA-Na and E-MA-Zn, i.e., $\bar{V}_b$ lies between $\bar{V}_c$ and $\bar{V}_a$. Small $\bar{V}_a$ value compared with that of LDPE may be caused by the segregation of the MA groups into the amorphous region. In the intermediate phase, the polymethylene chains take nearly all-trans conformation losing lateral packing order and have the density between those of the crystalline and the amorphous phase. This phase may act as weak cross-linking points, as a result, increase the elastic constant.

1-8. Conclusion

Relation between the temperature dependence of the elastic constant and that of the structures of the two E-MA ionomers and one non-ionic low density polyethylene (LDPE) was investigated in the range from 20 to 200 °C by Brillouin, IR, and Raman methods. As a result, it was revealed that the amount of the conformationally ordered polymethylene sequence in the ionomers was kept higher that that in LDPE up to the melting point of the polyethylene crystallites. This kept the value of the elastic constant of the ionomers higher than that of LDPE and prohibited

Table I-II. The specific volume of $\bar{V}_a$, $\bar{V}_b$, and $\bar{V}_c/cm^3g^{-1}$ of E-MA-Na, E-MA-Zn, and LDPE averaged in the range from 24 to 50°C.

	E-MA-Na	E-MA-Zn	LDPE
$\bar{V}_a$	1.08	1.06	1.19
$\bar{V}_b$	1.03	1.05	1.04
$\bar{V}_c$	1.01	1.01	1.01

the depression of the elastic constant during the heating process in the ionomers. The characteristic mechanical behavior of the ionomers was largely affected by the conformational order of the methylene sequence both in the crystalline and the non-crystalline region. In chapter 4, the author will further investigate how the presence of ionic groups affects the structure and the thermal transition behavior of the polymethylene chain in crystalline low molecular weight compounds consisting of ionic groups and non-ionic alkyl chains.

1-9. References

1) L. Holliday, Ed., "ionic Polymers", Applied Science Publishers, London, 1975.

2) A. Eisenberg and M. King, "Ion-Containing Polymers", Academic Press, New York, 1977.

3) A. T. Tsatsas, J. W. Reed, and W. M. Risen, Jr., J. Chem. Phys., 55, 3260 (1971).

4) G. B. Rouse, W. M. Risen Jr., A. T. Tsatsas, and A. Eisenberg, J. Polym. Sci., Polym. Phys. Ed., 17, 81 (1979).

5) A. Neppel, I. S. Butler, and A. Eisenberg, J. Polym. Sci., Polym. Phys Ed., 127, 2145 (1979).

6) A. Neppel, I. S. Butler, and A. Eisenberg, J. Polym. Sci., Polym. Phys. Ed., 20, 1069 (1982).

7) P. C. Painter, B. A. Brozoski, and M. M. Coleman, J. Polym. Sci., Polym. Phys. Ed., 20, 1069 (1982).

8) B. A. Brozoski, M. M. Colemann, and P. C. Painter, J. Polym. Sci., Polym. Phys. Ed., 21, 301 (1983).

9) B. A. Brozoski, M. M. Coleman, and P. C. Painter, Macromolecules, 17, 230 (1984).

10) B. A. Brozoski, P. C. Painter, and M. M. Coleman, Macromolecules, 17, 1591 (1984).

11) W. J. MacKnight, L. W. McKenna, B. E. Reed, and R. S. Stein, J. Phys. Chem., 72, 1122 (1968).

12) K. Ogura and H Sobue, Polym. J., 3, 153 (1972).

13) K. Ogura, H. Sobue, and S. Nakamura, J. Polym. Sci., Polym. Phys. Ed., 11, 2079 (1973).

14) T. R. Earnest, Jr., and W. J. MaKnight, Macromolecules, 13, 844 (1980).

15) R. Vacher and L. Bayer, Phys. Rev. B, 6, 639 (1972).

16) Y. Cho, Doctral Thesis, Osaka University, 1986.

17) R. G. Snyder, J. Chem. Phys., 76, 3921 (1982).

18) S. P. S. Porto, J. Opt. Soc. Am., 56, 1585 (1966).

19) L. N. Durvasula and R. W. Gammon, J. Appl. Phys., 50, 4339 (1979).

20) S. M. Lindsay, B. Halawith, and G. D. Patterson, J. Polym. Sci. Polym. Lett. Ed., 20, 583 (1982).

21) G. D. Patterson and J. P. Latham, Macromolecules, 10, 736, (1977).

22) C. H. Wang, D. E. Cavanaugh, and Y. Higashigaki, J. Polym. Sci., Polym. Phys. Ed., 19, 941 (1981).

23) G. R. Strobl and W. Hagedorn, J. Polym. Sci., Polym. Phys. Ed., 116, 181 (1978).

24) E. M. Brody, C. T. Lubell, and C. L. Beatty, J. Polym. Sci., Polym. Phys. Ed., 13, 295 (1975).

25) R. G. Snyder, N. E. Schlotter, R. Alamo, and L. Mandelkern, Macrommolecules, 19, 621 (1986).

26) R. G. Snyder, S. L. Krause, and J. R. Scherer, J. Polym. Sci., Polym. Phys. Ed., 16, 1593 (1978).

27) Y. Tsujita, S. L. Hsu, and W. J. MacKnight, Macromolecules, 14, 1824 (1981).

28) L. Manderkern, R. Alamo, W. L. Mattice, and R. G. Snyder, Macromolecules, 19, 2404 (1986).

29) F. C. Wilson, R. Longworth, and D. J. Vaughan, Am. Chem. Soc. Polym. Prepr., 9, 505 (1968).

30) B. W. Delf and W. J. MacKnight, Macromolecules, 2, 309 (1969).

31) D. J. Yarrusso and S. L. Cooper, Polymer, 26, 371 (1985).

32) D. M. Mathew and R. W. Sheets, J. Chem. Soc., A2203 (1969).

33) G. C. Pimentel and A. L. McCllelan, "The Hydrogen Bond", W. H. Freeman and Co., San Fransisco, 1960.

34) W. E. Fitzgerald and L. Nielsen, Proc. Roy. Soc. London, A282, 137 (1962).

35) A. V. Tobolskyl, D. W. Carlson, N. Indictor, and M. C. Shen, J. Polym. Sci., 61, S23 (1962).

36) A. V. Tobolsky and M. C. Shen, J. Phys. Chem., 67, 1886 (1963).

37) W. J. MacKnight, W. P. Taggert, and L. McKenne, J. Polym. Sci., Syme., 46, 83 (1974).

38) F. Bueche, J. Polym. Sci., 22, 113 (1956).

39) G. Kortleve, C. A. F. Tuijnman, and C. G. Vonk, J. Polym. Sci., A-2. 10, 123 (1972).

40) M. Glotin and L. Mandelkern, Colloid & Polymer Sci., 260, 182 (1982).

Chapter 2

Small-angle X-ray Scattering Study on Structural Changes of Ion Cluster in Zinc Salt of Ethylene-methacrylic Acid Copolymer on Water Absorption

2-1. Introduction

Chapter 1 deals with a specific role of ion aggregates in the charactersitic mechanical behavior of E-MA ionomers. Thus, elucidation of molecular-level structure and stability of the ion aggregates is the next step. However, the techniques of x-ray diffraction and vibrational spectroscopy which are commonly used for the structural analysis of crystalline materials are not so powerful for non-crystalline of poorly crystalline ionomer samples. Moreover, content of ionic groups is very small, usually less than 10 mol%, so that it is difficult to pick up convincible informations about ionic groups from the experimental results. It happens very often that weak signals due to ionic parts are strongly interfered by those of major non-ionic components. In the present work the author used two techniques; small-angle x-ray scattering (SAXS) for investigating the behavior of a reflection peak due to the ion cluster and infrared spectroscopy for analysing the absorption bands associated with the carboxylate anion (COO^-) (Chapter 3). Both signals are related directly to the ionic part and separated well from those of the non-ionic part. Most ionomers are, more or less, hygroscopic, and their physical properties are strongly influenced by the water content. Water molecules seem to be absorbed preferentially on the ionic groups and affect their aggregation state. Investigation of the changes in the SAXS peak and the COO^- infrared absorptions during the water absorption-desorption process gives us valuable information about the ion agrgregate.

Most ionomers, both crystalline and non-crystalline, give

rise to a characteristic x-ray reflection called "ionic peak" in the small-angle region (for example, E-MA-Na gives a reflection at the spacing of ca.20Å).[1-17] This is attributed to cluster formation of ionic groups. In order to explain the appearance of the reflection, two basically different models have been proposed: one is based on the interference between neighboring clusters and the other on the interference within individual cluster. Wilson et al.[1] first proposed that the peak position corresponded to the distance (of ca.20Å) between neighboring clusters arranged in an ionic domain. They considered that at least five repeat units (i.e. clusters) were required for the appearance of the SAXS peak. Thus, the size of the ionic domain present in ionomers was estimated to be of 100Å in diameter. Thereafter, Marx et al.[2] proposed a different model in which aggregates of 5-10Å diameter comprising a few ion pairs were distributed randomly in non-crystalline matrix, and the observed Bragg spacing should correspond to the averaged distance between the neighboring aggregates. On the contrary, MacKnight[3] proposed another scattering model, i.e. the intracluster scattering model in which the cluster consists of a spherical ionic core of radius 3-13Å surrounded by a hydrocarbon shell of radius 20-35Å. The "ionic peak" was considered to be caused by the difference in the electron density of the cluster and that of the surrounding amorphous matrix. For such hydgroscopic ionomers as poly(tetrafluro-ethylene)-based Nafion ionomers[11] and polystyrene-based ionomers,[15] the SAXS peak was found to shift to the smaller Bragg angle side as the water content increased.

For the hygroscopic systems adequancy of the above models was checked thorugh a quantitative analysis of the variation of the SAXS profile with water content. As a result, the experimental results of Nafion were well interpreted by the intracluster model, whereas those of polystyrene-based ionomers by the intercluster model. In the case of less hygroscopic polyethylene-based E-MA ionomers, little have been known so far about the effect of water. This chapter deals with changes in SAXS profile of E-MA-Zn ionomer accompanied with moisture absorption and with heat treatment.

2-2. Experimentals

2-2-1. Sample

Ionomer sample E-MA-Zn (Surlyn 472) was the same as that described in chapter 1.

2-2-2. SAXS measurement

A Rigaku Denki sealed tube x-ray generator operating at 40kV and 30mA was used for the SAXS experiment. The Cu-K_α radiation (λ = 1.542Å) was monochromatized with a Ni foil filter of 10 μm thickness. The x-ray beam was line focused (0.1x8mm^2) by a set of nickel-coated bent glass mirrors. The sample-to-detector distance was 30.2cm. Scattered intensity was measured by a Rigaku Denki one-dimensional position-sensitive proportional counter (delay-line type). The detector length was devided into 512 channels (0.1265mm/channel) on a multichannel analyzer. On each sample of about 2mm thickness, the intensity data were accumulated for 5000 seconds. The data were corrected for the sensitivity of the detector (the linearity was calibrated with Fe isotope and the dead time was 0%) and also for the transmittance of the sample specimen according to the standard method.[19] Slit desmearing procedure was made using the method of Glatter.[20] The absolute intensity was not observed. In order to estimate the background arising from density fluctuations, the middle-angle data were measured by a Searle small-angle x-ray diffraction camera in the 2θ region from 1.8 to 17.8°. However, because of the broadness of the ionic peak and the overlap by the tail of the strong (110) reflection of the polyethylene lattice, the contributions from the fluctuations were not separated and assumed to be constant in the 2θ range mentioned in the profile

analysis. The scattering arising from voids and inhomogeneous distribution of the isolated ionic groups which mainly causes a sharp upturn near zero angle was not considered.

Experiments of moisture absorption of the specimens used for the measurement were carried out in a desiccator held at a constant temperature (60.0 °C) under saturated vapor pressure. The amount of water absorbed by the specimens were weighed using a Mettler B-6 balance with the sentitivity 10^{-5} g in an open state. The equilibrium was achieved for about 5 days for the specimens as thick as 2mm. The weight loss or gain of the samples during the measurement was confirmed to be negligible.

2-3. Result and Discussion

The E-MA-Zn sample was melted at 150 °C and quenched in liq. N_2, then kept at ambient condition for 24h before the measurement. A broad "ionic peak" appeared around $2\theta = 4°$ as shown in the curve 1 of Fig.2-1. After drying the sample at 69 °C for 22h in vacuo, the curve 2 was obtained. The peak shifted a little to the low-angle side and a new reflection apperaed around $2\theta = 0.72°$. The latter reflection was ascribed to the polyethylene-lamellae phase having the long spacing of 103Å (evaluated with Lorentz correction) formed during the drying process. The intensity of the ionic peak was very weak compared with that of polyethylene-lamellae peak.

In order to obtain precise scattering profile of the ionic peak free from the interference by the lamellae peak, it is desirable to keep the polyethylene-lamellae peak at a constant

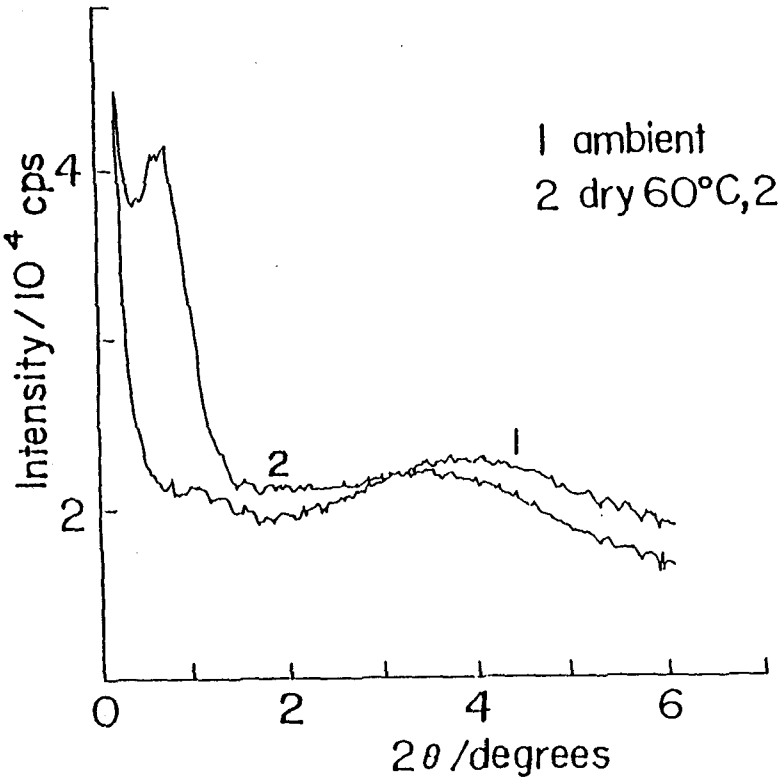

Fig.2-1. SAXS curves for E-MA-Zn.

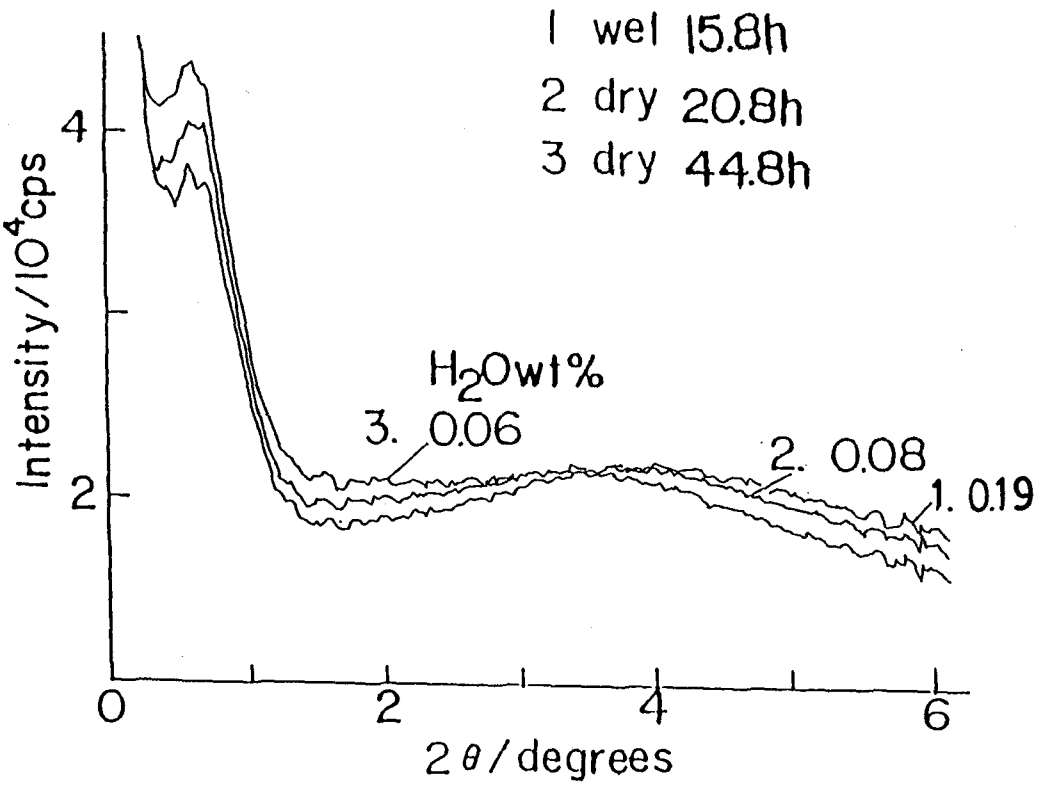

Fig.2-2. SAXS curves for E-MA-Zn on desorption at 60.0°C.

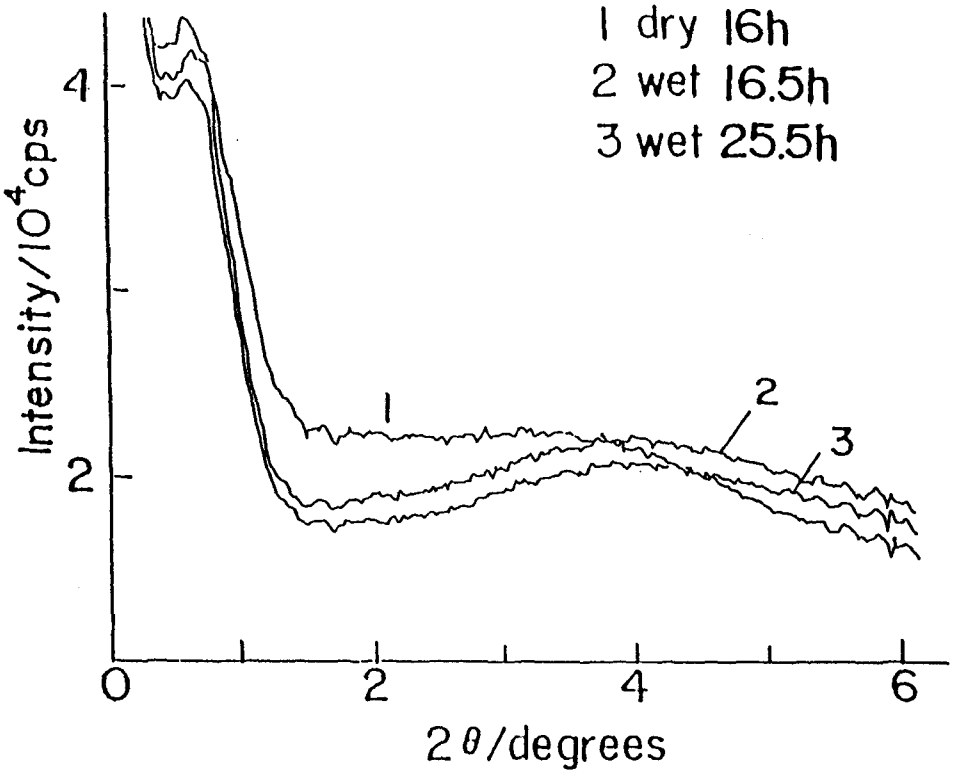

Fig.2-3. SAXS curves for E-MA-Zn on adsorption at 60.0°C.

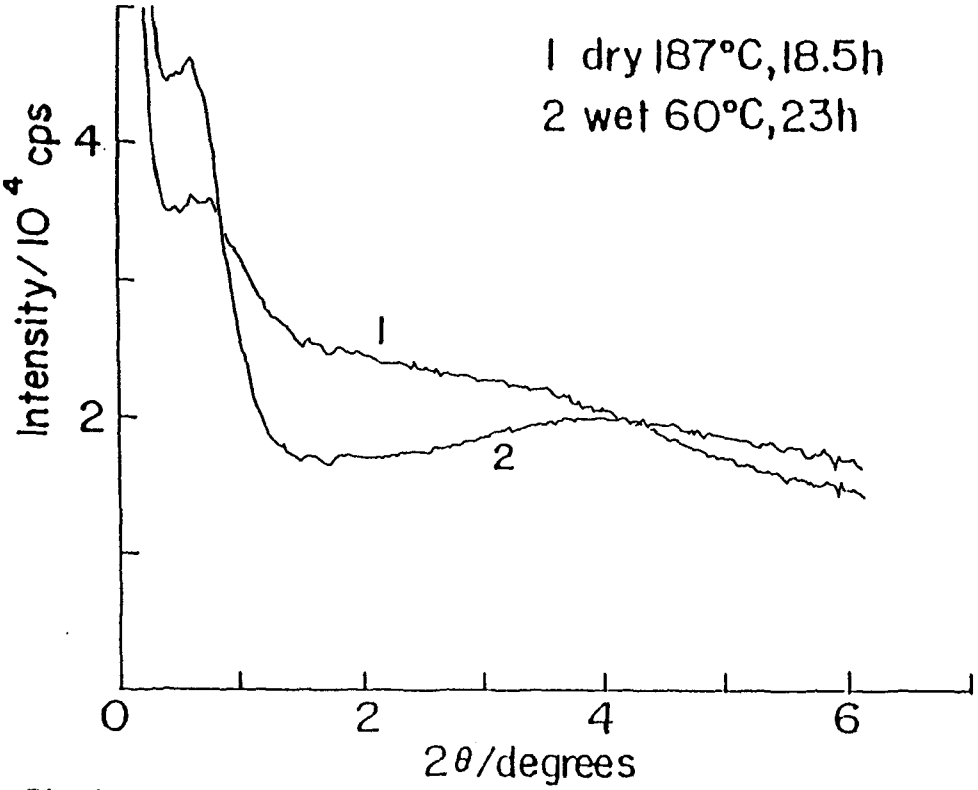

Fig.2-4. SAXS curves for E-MA-Zn.

position enough distant from the ionic peak and to keep its intensity constant throughout the absorption-desorption cycle for one sample specimen. For this purpose, dependence of the polyethylene-lamellae peak position and intensity on the temperature of sample treatment was investigated in the range from 10 to 90 °C, and a suitable temperature (60.0 °C) for the moisture desorption-absorption procedure was chosen. The changes in SAXS pattern on the moisture desorption and absorption processes are shown in Fig.2-2 and 2-3, respectively. A sample quenched from the melt and then exposed to water for 16h (having the water content 0.19wt%) gave the curve 1 in Fig.2-2. The curves 2 and 3 are of the same sample after drying for 21h (0.08wt%) and 45h (0.06wt%), respectively. The scattering angle 2θ of the ionic peak shifted from 3.95 to 3.48° as the water content decreased from 0.19 to 0.06%. This shift corresponds to an increase of the Bragg spacing from 22.4 to 25.4Å, indicating that the apparent cluster size or the distance between neighboring clusters expands on drying. In Fig.2-3, the curve 1 is of a melt-quenched sample dried for 16h. Here the ionic peak located at about 3.31° and was superimposed by a broad tail at the low-angle side. After moisture absorption (the curves 2 and 3) the ionic peak was recovered to that of curve 1 in Fig.2-2. Thus, the peak shift on moisture desorption-absorption process occurs reversibly. Yarrusso et al.[15] analysed quantitatively the temperature dependence of the SAXS pattern of E-MA-Zn ionomers, but effects of two factors, the amount of absorbed water and the degree of crystallinity were not taken into consideration. As for the polyethylene-lamellae phase, increase

in annealing time resulted an increase in intensity as shown by curves 1-3 of Fig.2-2 and curves 1, 2 of Fig.2-3. The intensity depression from curve 2 to curve 3 in Fig.2-3 cannot be explained. This might be due to some experimental artifacts.

For the sample which was heated at 187 °C for 19h and then cooled to room temperature, the SAXS pattern of curve 1 in Fig.2-4 was obtained. In this curve the ionic peak spreads in a wide scattering angle. This indicates that at the temperature higher than the melting point of the polyethylene crystallites, a reconstruction of ion clusters takes place. Yarrusso et al.[15] observed similar spreading of the ionic peak for an E-MA-Zn sample measured above 100 °C and interpreted that this was due to an increase either in the radius of the ion cluster or in the averaged volume available to each cluster.[15] The large-size aggregates formed are frozen even after cooling to room temperature as indicated by a broad profile covering the low-angle region. When this sample was stored in water at 60 °C for 23h, the SAXS pattern is recovered to the starting one (the curve 2).

In the cases of Nafion[9-11] and polystyrene-based ionomers,[16] the ionic peak shifted to the lower angle side on moisture absorption. This shift was interpreted in terms of the inter-cluster as well as intra-cluster models. Based on the inter-cluster model, it is expected that the distance between the neighboring clusters increases on moisture absorption, since the entrance of water increases the dielectric constant of the medium and reduces the attractive electrostatic forces between

clusters.[18] Based on the intra-cluster model, the shift can be explained as the result of the swelling of individual clusters. The shift found in the present sample is in the opposite direction and seems difficult, at first sight, to be explained by any previous cluster models.

In order to interpret the observed results, the scattered intensity I(q) was calculated using the equation for the model of closely assembled hard spheres having a uniform radius (Fig.2-5) with the interference factor derived by Percus and Yevick.[21] Using the same model but with Fournet's interference factor,[22-24] Yarusso reproduced the measured profiles of a series of ionomers.[15] The equation is expressed as

$$I(q) = I_e(q)V \frac{1}{v_p} v_1^2 \rho_1^2 \Phi^2(qR_1) \frac{1}{1 + 24(v_{CA}/v_p)(G(A)/A)} \qquad (2\text{-}1)$$

where $I_e(q)$ is the scattered intensity for a single electron as a function of the scattered angle q (= $4\pi\sin\theta/\lambda$, λ : the incident wavelength) and V the irradiated sample volume. R_1 is the radius of the spherical particle having the electron density ρ_1 (= the core electron density - the mean medium electron density), $A = 2qR_{CA}$ where R_{CA} the closest approach distance between two particles. The corresponding spherical volumes are given as $v_1 = (4/3)\pi R_1^3$ and $v_{CA} = (4/3)\pi R_{CA}^3$, v_p the sample volume per particle. G(A) is given by

$$G(A) = (\alpha/A^2)(\sin A - A\cos A) + (\beta/A^3)(2A\sin A + (2 - A^2)\cos A - 2)$$

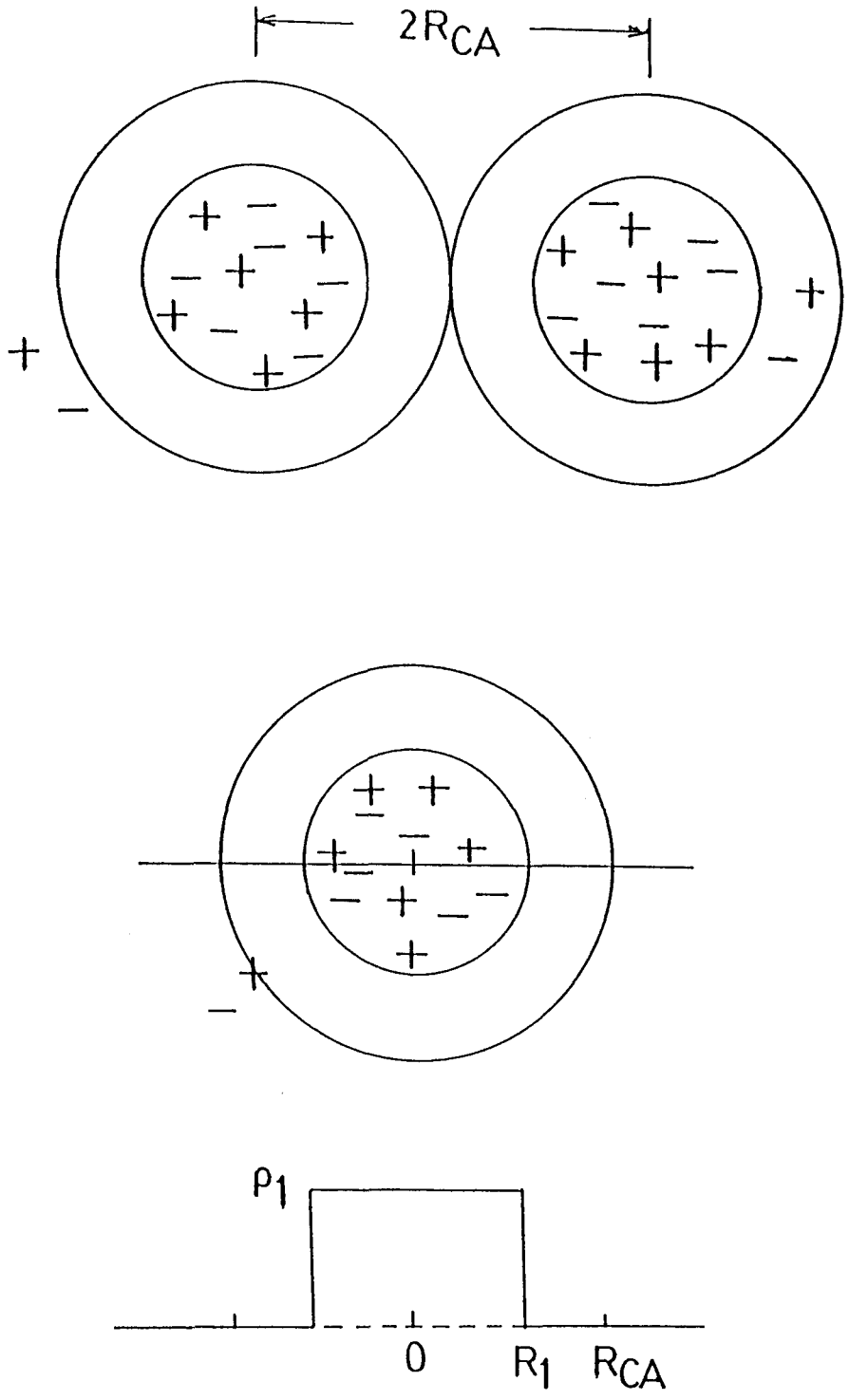

Fig.2-5. Schematic representation of the cluster structure and corresponding electron density distribution where ρ_1 is the electron density of the core and R_1 the radius of the core, R_{CA} the closest approach distance between the clusters. (after Yarusso et al. 1985).

$$+ \left(\gamma/A^5 \right)\left(-A^4 \cos A + 4[(3A^2 - 6)\cos A + (A^3 - 6A)\sin A + 6] \right) \quad (2\text{-}2)$$

where

$$\alpha = (1 + 2\eta)^2/(1 - \eta)^4$$

$$\beta = -6\eta(1 + \eta/2)^2/(1 - \eta)^4 \quad (2\text{-}3)$$

$$\gamma = \eta(1 + 2\eta)^2/2(1 - \eta)^4$$

Here, η is the hard-sphere volume fraction $(4/3)\pi R_{CA}^3/v_p$. $\Phi(x)$ is the scattering factor of a spherical particle given by

$$\Phi(x) = \frac{\sin x - x\cos x}{x^3}$$

By using eqs 2-1 to 2-3 the variation of the scattering profile of the E-MA-Zn ionomer with water content was examined. The equation involves four variable parameters, R_1, R_{CA}, ρ_1, and v_p.

The fitting of the observed scattering curves to eq 2-1 was performed as described in what follows. The observed curves in Fig.2-2 were converted to the desmeared ones using a computer program, although desmearing did not change the scattering profile so significantly in the region of $2\theta = 1 - 6^o$. Since we measured only the relative intensities, rather than absolute ones, we used a scale factor common to the three curves and discussed only relative values of ρ_1. The value of v_p was fixed to be $13nm^3$ by the reason described below. The other two parameters R_1 and R_{CA} were adjusted for each curve by the trial-and-error method so as to obtain a good agreement between the observed and calculated results (Fig.2-6). The values of the

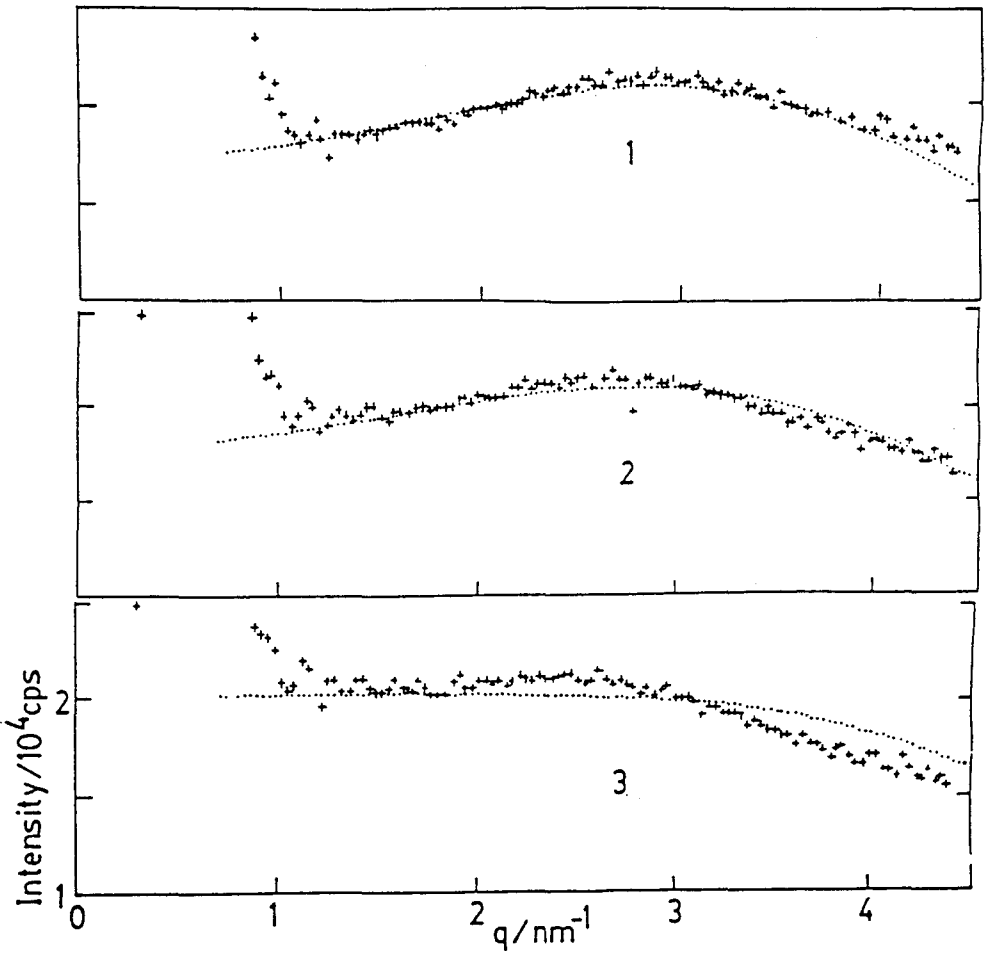

Fig.2-6. Variation of the small-angle x-ray scattering profile of E-MA-Zn as a function of water content, (1) 0.19H_2Owt%, (2) 0.08%, (3) 0.06%, + : obs, .:calc.

Table II-I. Parameter values which determine small-angle x-ray scattering profile of E-MA-Zn at various water contents.

H_2Owt%	R_1/nm	R_{CA}/nm	v_p/nm^3	ρ_1/nm^{-3}	ion group mole%
0.19	0.38	0.84	13	1.16*	2.71
0.08	0.39	0.80	13	1.08*	2.71
0.06	0.40	0.75	13	1.00*	2.71
——	0.44	0.63	26	225	0.90^{15}
——	0.43	0.76	10	225	2.45^{15}
——	0.45	0.76	11	225	3.25^{15}
——	0.45	0.74	11	225	3.25^{15}
——	0.47	0.73	14	225	3.25^{15}

* : relative values.

parameters obtained for the three samples are summarized in Table II-I. The result tells us that as the water content increases the R_{CA} and ρ_1 increase, while the R_1 remains almost constant. This may be interpreted as follows. The water molecules absorbed in the ion core increase the core electron density, and those absorbed outside the cluster increase R_{CA} by the electrostatic (due to lowering the attractive intercluster forces) and steric effects.

Yarusso et al. analyzed the SAXS profile of zinc salts of E-MA ionomers having three different ion group contents and obtained the parameters as listed in Table II-I.[15] In the case of low ion concentration, as in the present sample, v_p is nearly reciprocally proportional to the ion concentration if the cluster size is kept constant. Yarusso showed that the v_p increased from 12 to 26nm^3 as the ion concentration decreased from 3.25 to 0.90mol%. Thus, for the present sample, v_p was assumed to be 13nm^3 from its concentration of 2.71mol%.

Dimensional change of the ion cluster in E-MA-Zn during the moisture absorption was investigated by SAXS technique. Unlike the cases of previously investigated hygroscopic ionomers, it was found that the apparent peak maximum position of the ionic peak shifted toward the high angle side with an increase in the water content. This observed shift can be interpreted as follows. Although the intercluster distance (R_{CA}) increased a little with water content as expected, the inter-particle interference and minor change in other structural parameters perturbed the scattering profile in an unexpected manner, since the scattering

intensity was so weak. The apparent extraordinary shift may be ascribed to the combined change in the position and the broadness of the profile with the variation in R_{CA}. The effect of the change in ρ_1 may take a part.

2-4. references

1) F. C. Wilson, R. Longworth, and D. J. Vaughan, Am. Chem. Soc. Polym. Prepr., 9, 505 (1968).

2) C. L. Marx, D. F. Caulfield, and S. L. Cooper, Macromolecules, 6, 344 (1974).

3) W. J. MacKnight, W. P. Taggert, and R. S. Stein, J. Polym. Sci., Polym. Sym., 45, 113 (1974).

4) A. Moudden, A. M. Levelut, and M. Pineri, J. Polym. Sci., Polym. Phys. Ed., 15, 1707 (1977).

5) E. J. Roche, R. S. Stein, and W. J. MacKnight, J. Polym. Sci., Polym. Phys. Ed., 18, 1035 (1980).

6) E. J. Roche, R. S. Stein, T. P. Russel, and W. J. MacKnight, J. Polym. Sci., Polym. Phys. Ed., 18, 1497 (1980).

7) S. P. Rowland, Ed., "Water in Polymers", ACS Symposium Series 127, Washington, D. C., 1980.

8) E. J. Roche, M. Pineri, R. Duplessix, and M. Levelut, J. Polym. Sci., Polym. Phys. Ed., 19, 1 (1981).

9) T. D. Gierke, G. E. Munn, and F. C. Wilson, J. Polym. Sci., Polym. Phys. Ed., 19, 1687 (1981).

10) M. Fujimura, T. Hashimoto, and H. Kawai, Macromolecules, 14, 1309 (1981).

11) M. Fujimura, T. Hashimoto, and H. Kawai, Macromolecules, 15, 136 (1982).

12) E. J. Roche, M. Pineri, and R. Duplessix, J. Polym. Sci., Polym. Phys. Ed., 20, 107 (1982).

13) D. J. Yarusso and S. L. Cooper, Macromolecules, 16, 187 (1983).

14) W. C. Forsman, W. J. MacKnight, and J. S. Higgins,

Macromolecules, 17, 490 (1984).
15) D. J. Yarusso and S. L. Cooper, Polymer, 26, 371 (1985).
16) M. Pineri, F. Volino, and M. Escoubes, J. Polym. Sci., Polym. Phys. Ed., 23, 2009 (1985).
17) C. E. Williams, T. P. Russel, R. Jerome, and J. Horrison, Macromolecules, 19, 2877 (1986).
18) A. Eisenberg, Macromolecules, 3, 147 (1970).
19) International Table for X-ray Crystallography, Vol. III, The Kynoch Press, England, 1962.
20) O. Glatter, J. Appl. Crystallogr., 7, 147 (1974).
21) D. J. Kinning and E. L. Thomas, Macromolecules, 17, 1712 (1984). K. O. Hodgson, R. A. Register, and S. L. Cooper, Macromolecules, 21, 1698 (1988).
22) G. Fournet, Compt. Rend., 228, 1421 (1949).
23) G. Fournet, ibid., 229, 1071 (1949).
24) G. Fournet, Acta Crystallogr., 4, 293 (1951).

Chapter 3

Infrared Study on Intra-cluster Structural Changes in Zinc Salt of Ethylene-methacrylic Acid Copolymer on Water Absorption

3-1. Introduction

This chapter deals with the molecular level structure within an ion cluster of E-MA-Zn. This has been studied with various experimental methods.[1-27] Eisenberg postulated that there were two types of ion aggregate in some ionomers.[28,29] At low ion concentrations (below 5 - 6mol%) aggregates of a few ionic units called "multiplet" is formed. The multiplet consists of only ionic groups and does not contain hydrocarbon chains. When the ion concentration becomes sufficiently high (above 5 - 6mol%), association of the multiplets occurs, forming cluster where the constituent multiplets are separated from each other by non-ionic matrix. In order to elucidate internal structures of multiplet or ion cluster, various spectroscopic studies have been performed. Ion concentration dependence of far-infrared spectra[19,20] and low-frequency Raman spectra of polystyrene-based ionomers[21-23] was investigated and some characteristic bands were assigned to the translational vibrations of the cation in anionic electrostatic field in either multiplet or ion cluster. As for vibrations of the anionic groups, the $\nu_a(COO^-)$ mode was found to be sensitive to the amount of hydration and the coordination structure. Brozoski et al. investigated extensively the $\nu_a(COO^-)$ infrared spectra of E-MA ionomers with various water contents.[24-27] In a dry state, splitting of the $\nu_a(COO^-)$ band was observed for Na, Mg, Ca, Sr, and Ba salts but not for K, Cs, and Zn salts. The split must be indicative of the existence of a locally ordered structure (multiplet). Several bands were tentatively assigned to those of mutiplet or cluster, but the detailed structures of multiplet and cluster are still uncertain.

In chapter 1, the spectral change of the $\nu_a(COO^-)$ band of E-MA-Zn with rising temperature is suggested to be caused by the desorption of water. The split bands at 1539, 1560, and 1625cm^{-1} were found at high temperature. In this chapter, the spectral change for E-MA-Zn with water content is discussed with the aim to obtain information about the intracluster structure.

3-2. Experimentals

3-2-1. Sample

Ionomer sample E-MA-Zn (Surlyn 472) was the same as that described in chapters 1 and 2.

3-2-2. Infrared Measurement

Infrared spectra were measured with a JASCO A-3 spectrophotometer. The resolution at 1600cm^{-1} was 2.6cm^{-1}.

Experiment of moisture absorption of the specimen used for the IR measurements was carried out in a desiccator held at 60.0±0.05 ^{o}C under the saturated vapor pressure. Film specimens for IR measurement were dried first at 41.0^{o}C under vacuum (10^{-3} Torr) over 2 weeks until they approached to their respective constant weight, i.e. to the "equilibrium dried weight". These dried samples still contained residual water. The "absolutely dry weight" was estimated by an extrapolation of the infrared intensities as will be described below. Then, the film specimens were subjected to moisture absorption-desorption process at 60.0^{o}C. To keep the degree of crystallinity of the sample constant throughout the measurement, the films were annealed beforehand at 60.0^{o}C over 10h, and the absorption-desorption procedure was carried out at the same temperature. The equilibrium was achieved over 30h. The amount of water absorbed by the specimens was weighed as described in chapter 2. To get enough accuracy, 20 pieces of films were weighed at the same time.

3-3. Result and Discussion

On the moisture absorption-desorption process a substantial

spectral change was observed in the 1500 - 1630cm^{-1} region (Fig.3-1). At water content of 0.03wt% (the value is based on the "equilibrium dried weight"), there appear plural bands assignable to the $\nu_a(COO^-)$ mode. As the water content increases to 0.24% these bands tend to collapse each other into one band centered at 1587cm^{-1}. This spectral change occurs reversibly with respect to the water content.

The IR absorption curve was separated into four bands by assuming a Gaussian + Lorentzian function for each band, expressed as

$$I(\nu) = h_1 \exp\left(-\ln 2\left(\frac{\nu - \nu_0}{\sigma}\right)^2\right) + h_2 \frac{\sigma^2}{(\nu - \nu_0)^2 + \sigma^2} \qquad (3\text{-}1)$$

where ν_0 is the peak position. The Gaussian and Lorentzian components have the peak absorbances of h_1 and h_2, respectively. In order to decrease the number of adjustable parameters, the two components are assumed to have the same half-width σ. Two peaks at 1625cm^{-1} (at 0.03%) and at 1587cm^{-1} (at 0.24%) are easily distinguished from other peaks. The two bands have almost the same half-width. By trial and error method, the observed spectra for four water contents were reproduced by assuming four bands centered at 1625, 1587, 1560, and 1539cm^{-1} having nearly the same half-width. The ratio of the Lorentzian/Gaussian components (h_2/h_1) was fixed to 4.10 for every band and the relative heights (h_2) of the three bands at 1539, 1560, and 1625cm^{-1} were fixed at 9 : 8 : 7. The ratio was confirmed to remain constant independently of the water content. In other

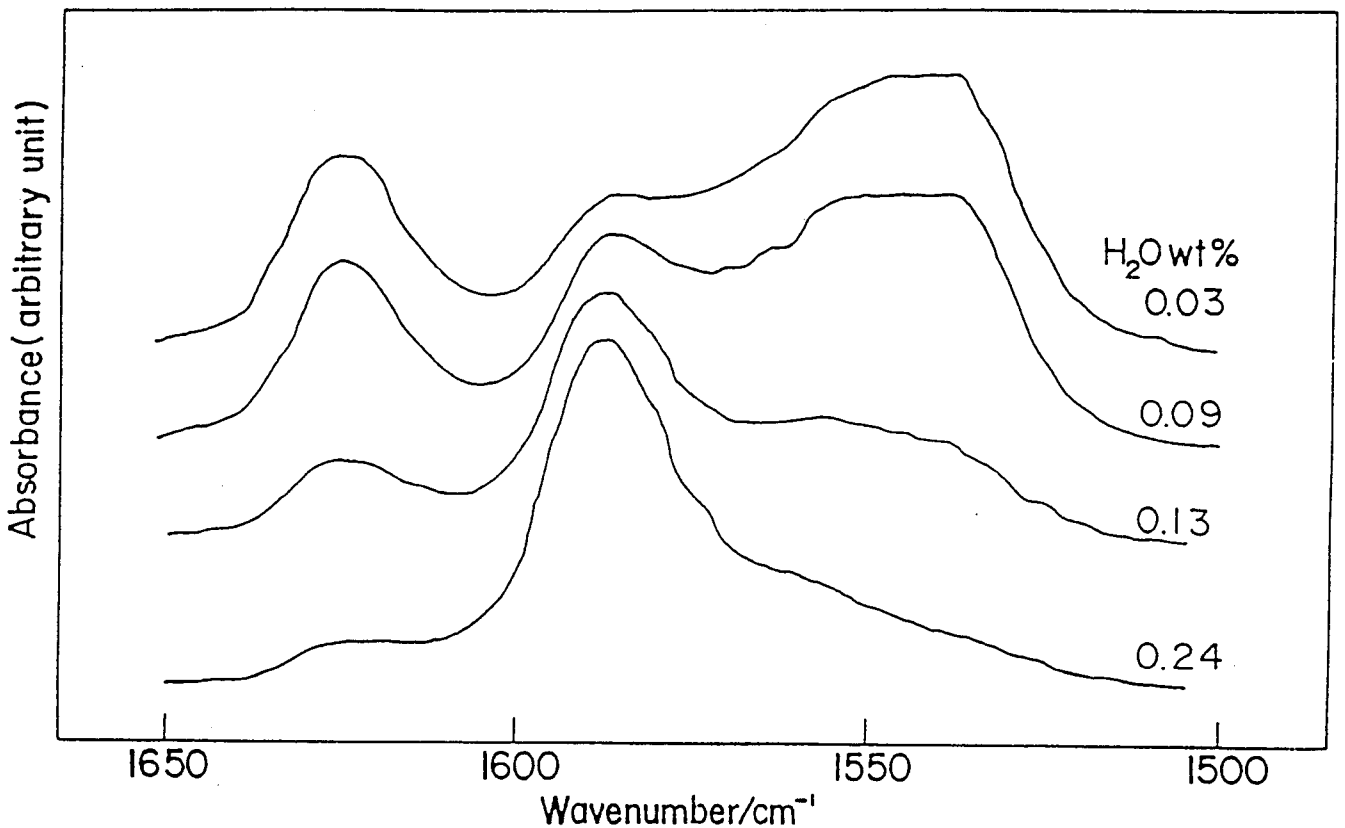

Fig.3-1. Changes of contours in $\nu_a(COO^-)$ region for E-MA-Zn at various H_2Owt%s.

word, the intensities of these bands varies (increase with decreasing water content) in a parallel way. Therefore, the triplet should be assigned to a specific structure of the carboxylate groups in the dry state. On the other hand, the singlet at 1587cm^{-1} whose intensity increases with increasing water content should be assigned to those in the moistened state. The slit-function distortion and the contribution of asymmetric component were not considered. The parameters used are listed in Table III-I. The resultant band separations were shown in Fig.3-2.

By using relative integral intensities of the triplet and the singlet, the equilibrium between the dry and the wet state was considered. The integrated intensities of the dry and wet states are denoted by K_{dry} and K_{wet}, respectively. If the thickness and the density of the film are kept constant on the moisture absorption, K_{dry} is expressed as

$$K_{dry} = \varepsilon_{dry} x_{dry} \qquad (3\text{-}2)$$

where ε_{dry} denotes the integrated molar absorption coefficient of the triplet and x_{dry} the mole fraction of the COO^- groups in the dry-state. Similarly, for the wet-state,

$$K_{wet} = \varepsilon_{wet} (1 - x_{dry}) \qquad (3\text{-}3)$$

where ε_{wet} denotes the molar absorption coefficient of the 1587 cm^{-1} band. With eqs 3-2 and 3-3, the following equation is obtained.[30,31]

$$K_{wet} = \varepsilon_{wet} - K_{dry}(\varepsilon_{wet}/\varepsilon_{dry}) \qquad (3\text{-}4)$$

Table III-I. h_2 and σ of bands at 1539, 1560, 1587, and 1625cm^{-1} at various water contents: ( ) is referred to "absolutely dried weight".

H_2Owt%	ν_o/cm^{-1}	1539	1560	1587	1625
	σ/cm^{-1}	11.8	11.8	11.2	10.2
		h_2			
0.03 (0.17)		9.56	8.50	5.40	7.44
0.09 (0.23)		9.00	8.00	7.80	7.00
0.13 (0.27)		3.94	3.50	9.80	3.06
0.24 (0.38)		2.48	2.20	14.00	1.93

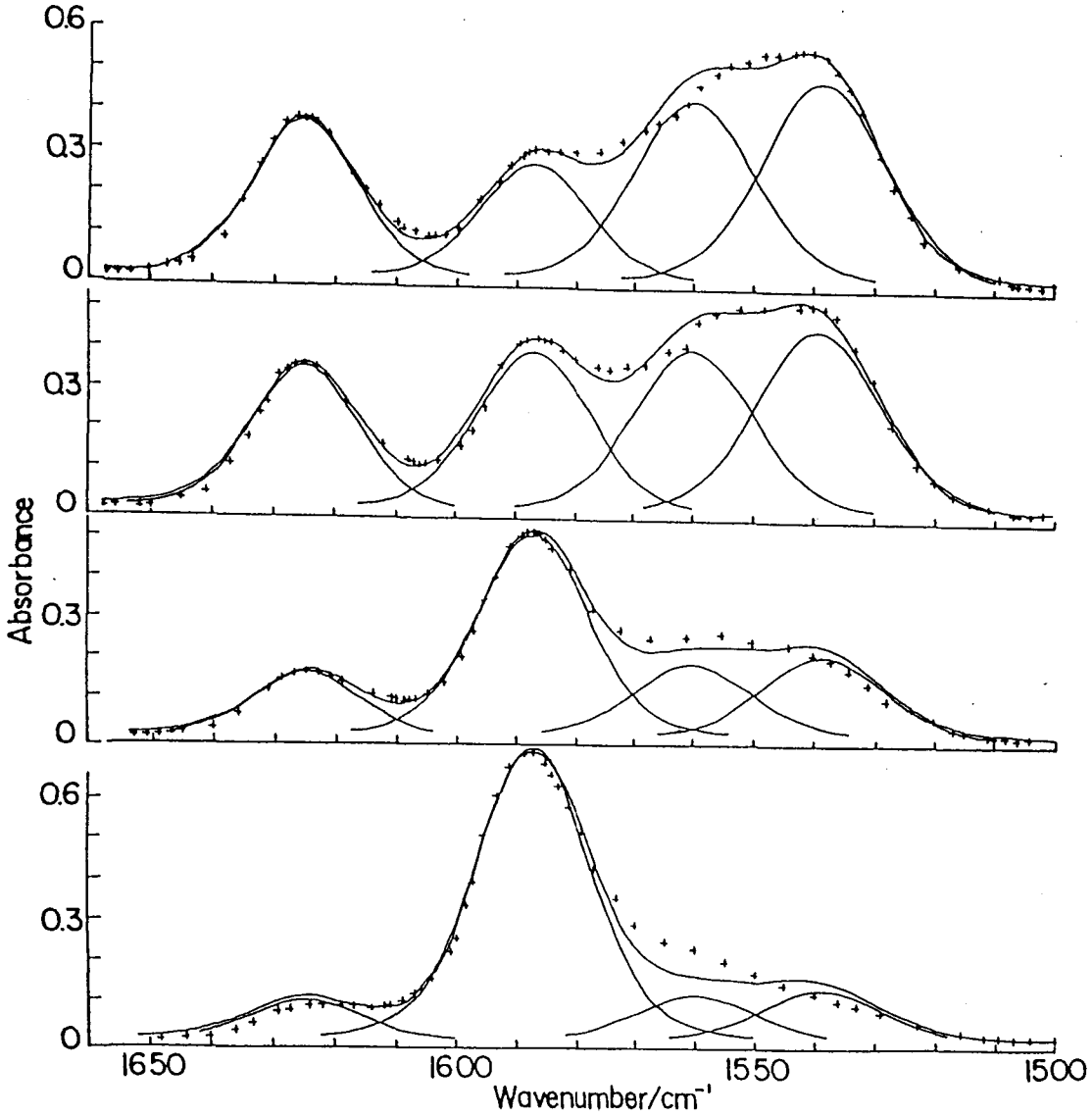

Fig.3-2. Separated contour of $\nu_a(COO^-)$ for E-MA-Zn at 0.03 % (upper), 0.09 %, 0.13 %, and 0.24 H_2Owt% (lower), +: obs, -: calc.

Thus, the K_{wet} vs. K_{dry} plot gives a straight line as shown in Fig.3-3. From the slope, the ratio $\varepsilon_{wet}/\varepsilon_{dry}$ is obtained as 0.343. From eqs 3-3 and 3-4, x_{dry} is given as[32]

$$x_{dry} = 1/(1 + K_{wet}\ \varepsilon_{dry}/K_{dry}\ \varepsilon_{wet}) \qquad (3\text{-}5)$$

x_{dry} (or $x_{wet} = 1 - x_{dry}$) for each water content (based on the equilibrium dried weight) is evaluated as shown in Fig.3-4. The intercept of the straight line on the negative side of the abscissa is considered to correspond to the amount of residual water in the equilibrium dried state. By subtracting this value 0.751×10^{-4}mol/g from the water content based on the "equilibrium dried weight", the water contents based on the "absolutely dried weight" of the specimen can be obtained. From Fig.3-4 we are able to derive the hydration number to the ionic group in the wet state. The molar amount of the COO^- group in the wet state equals to x_{wet} times the total molar amount of the COO^- in the sample, the latter being evaluated from the comparison of the sample as 8.41×10^{-4}mol/g. From the line slope in Fig.3-4 the molar ratio (COO^-/H_2O) in the wet state is obtained as 3.56. This value indicates that in the wet state about one water molecules are absorbed per four carboxylate groups, or one H_2O molecules are absorbed per two Zn^{2+} ion. In the absorption of heavy water the $\nu_a(COO^-)$ singlet due to the wet state appears at the same position as the case of normal water, suggesting that hydration takes place preferentially to Zn cation, not to the carboxylate groups.[33]

It is necessary to mention a remarkable difference in molar

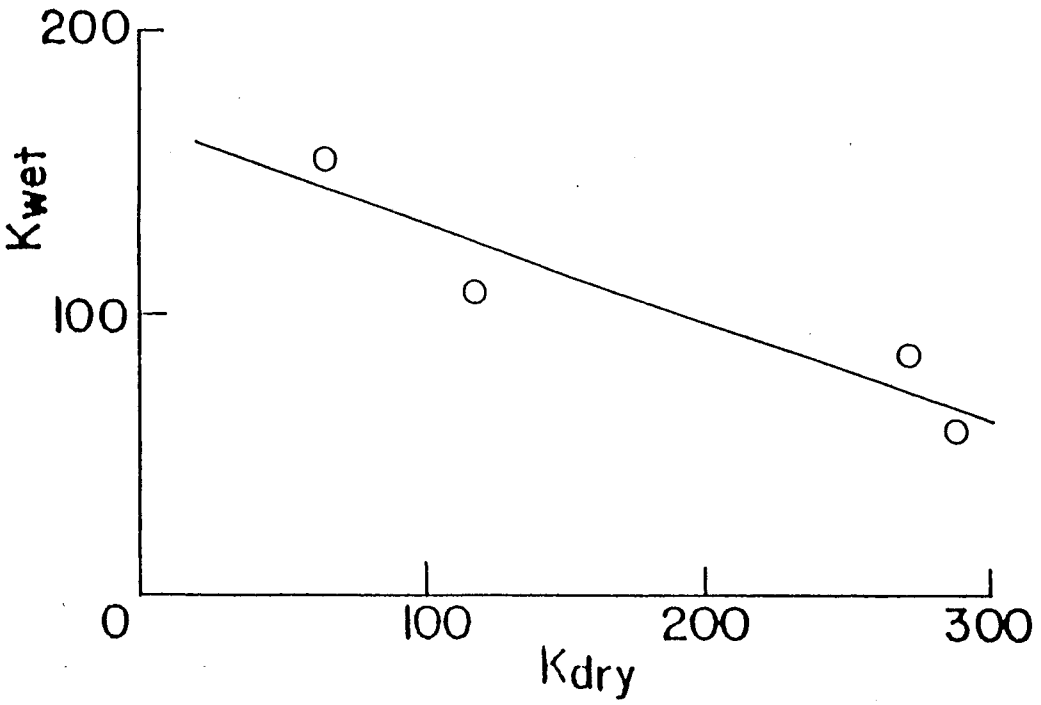

Fig.3-3. Relation between K_{wet} and K_{dry}.

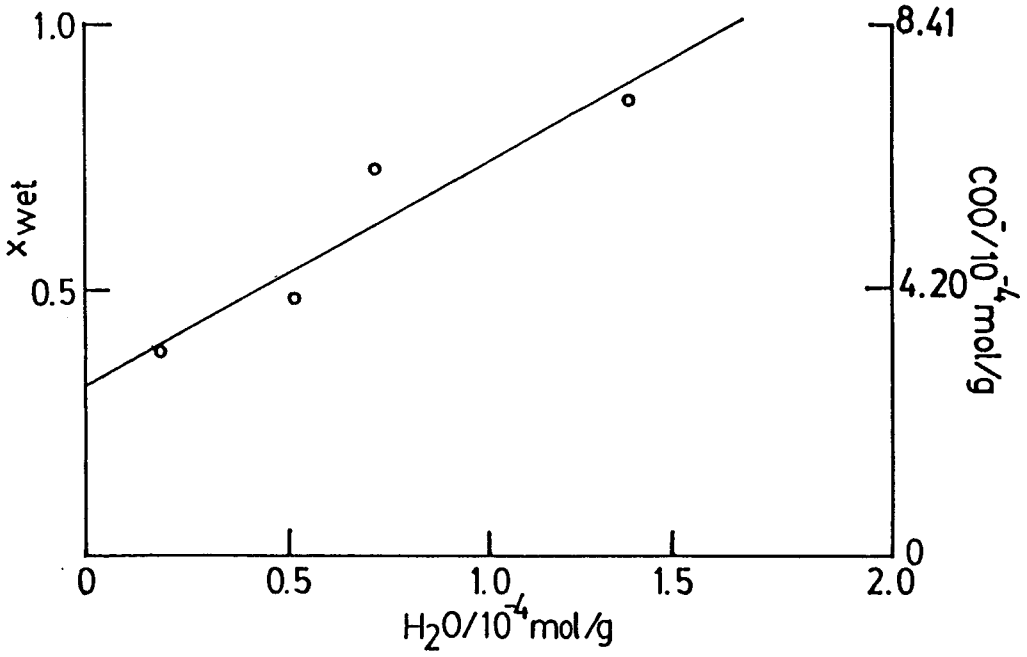

Fig.3-4. Relation between x_{wet} and molar amount of H_2O adsorbed.

absorption coefficient of the $\nu_a(COO^-)$ bands between the dry and wet states; ε_{wet} is only one third of ε_{dry}. As one of the origins of such a big difference, the dielectric field effect may be considered. In general, the integrated intensity ratio of a certain infrared band in liquid (A_l) and gaseous (A_g) phase is described based on Debye's theory[34] as

$$\frac{A_l}{A_g} = \frac{1}{n}\left(\frac{n^2 + 2}{3}\right)^2 \qquad (3\text{-}6)$$

where n is the refractive index of the liquid phase. Another expression was given by Menke[35] as

$$\frac{A_l}{A_g} = \frac{1}{n}\left(\frac{3n^2}{2n^2 + 1}\right)^2 \qquad (3\text{-}7)$$

Polo and Wilson[36] revealed that the eq 3-7 is reduced to eq 3-6 when the reaction field in Onsager's theory[37] is properly applied. In the case of E-MA-Zn the intensty ratio of the $\nu_a(COO^-)$ band in the dry and wet states may be expressed as

$$\frac{\varepsilon_{wet}}{\varepsilon_{dry}} = \frac{n_{dry}}{n_{wet}}\left(\frac{n_{wet}^2 + 2}{n_{dry}^2 + 2}\right)^2 \qquad (3\text{-}8)$$

where n_{dry} and n_{wet} are the refractive indices of the dry and wet states, respectively. In order to estimate the intensity ratio caused by this origin, the cases of $ZnSO_4$ and $CaCO_3$ and their hydrates were considered. The averaged n value of $ZnSO_4$ is 1.666 and that of $ZnSO_4.7H_2O$ is 1.474 for λ = 589nm.[38] The difference in n for $ZnSO_4$ and $ZnSO_4.7H_2O$ may be caused by the

difference in the density between the two compounds. Assuming a linear relationship between n and the hydration number, n = 1.652 for $ZnSO_4 \cdot \frac{1}{2}H_2O$. This value gives the ratio $\varepsilon_{wet}/\varepsilon_{dry}$ as 0.989. From the values of n for $CaCO_3$ (calcite) (n = 1.572) and $CaCO_3.H_2O$ (n = 1.567) for λ = 589nm,[38] the corresponding ratio is evaluated as 0.998.

Thus, the dielectric field effect cannot interpret the big difference in absorptivity between the two states. The second origin may be related to the vibrational coupling between the carboxylate groups and water molecules. This may cause an "intensity borrowing" from the $\nu_a(COO^-)$ to the internal and/or external (librational) modes of water molecules. Unfortunately, at present there are no experimental evidence supporting this idea.

The multipeak structure in dry state (Fig.3-2) is very specific to this sample. It may be due to the vibrational coupling between COO^- groups constructing a definite local structure. On the contrary, in the wet state the local structure is disturbed by hydration and the coupling between the neighboring groups may be averaged, resulting a single band. With the observed split frequencies in the dry state the interacting force constants between the vibrational units were estimated based on a simple vibrational model consisting of three units as depicted in Fig.3-5. The validity of postulating such a cluster structure consisting of three units will be examined by comparing the spectroscopic result with that of SAXS analysis (chapter 2). The circles 1, 2, and 3 correspond to the vibrational units. The kinetic energy T is expressed by

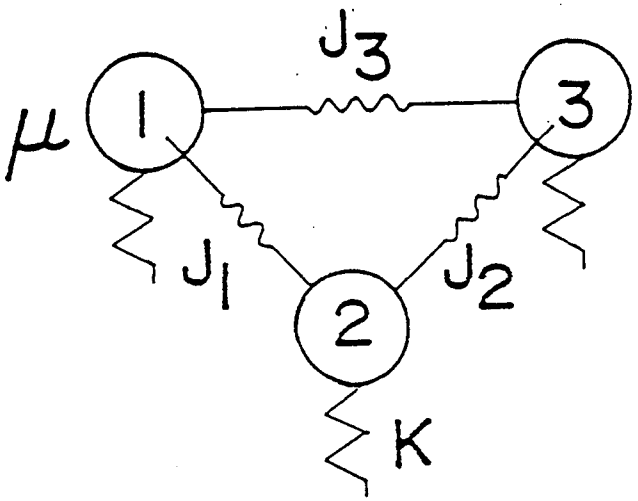

Fig.3-5. Vibrational model of multiplet.

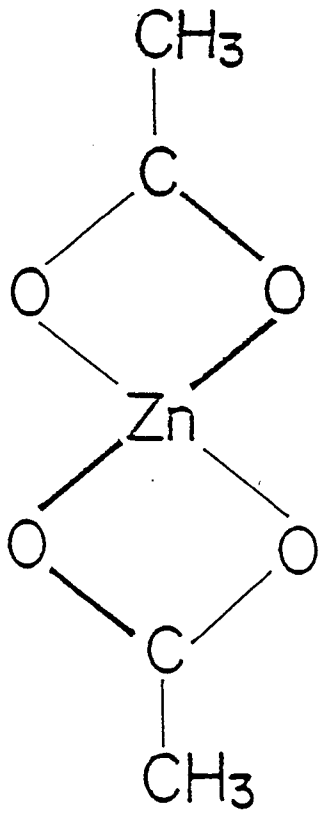

Fig.3-6. Structure of zinc acetate anhydride.

$$2T = (\dot{Q}_1^2 + \dot{Q}_2^2 + \dot{Q}_3^2)\mu \qquad (3\text{-}9)$$

where Q_1, Q_2, and Q_3 are the normal coordinates of the $\nu_a(COO^-)$ mode in the three vibrational units, respectively. A dot means the derivative with respect to the time, μ the corresponding reduced mass. The potential energy V is given by

$$2V = K(Q_1^2 + Q_2^2 + Q_3^2) + 2(J_1Q_1Q_2 + J_2Q_2Q_3 + J_3Q_3Q_1) \qquad (3\text{-}10)$$

where K is the force constant of the unperturbed $\nu_a(COO^-)$ mode, J_1, J_2, and J_3 the cross-terms between the units 1-2, 2-3, and 3-1, respectively. The secular equation is described as

$$\begin{vmatrix} K-\lambda & J_1 & J_3 \\ J_1 & K-\lambda & J_2 \\ J_3 & J_2 & K-\lambda \end{vmatrix} = 0 \qquad (3\text{-}11)$$

where λ is one of three roots of the cubic equation of

$$(K-\lambda)^3 - (J_1^2 + J_2^2 + J_3^2)(K-\lambda) + 2J_1J_2J_3 = 0 \qquad (3\text{-}12)$$

With three eigenvalues λ_1, λ_2, and λ_3, the following equations are defined.

$$(K-\lambda_1) + (K-\lambda_2) + (K-\lambda_3) = 0 \qquad (3\text{-}13)$$

$$(K-\lambda_1)(K-\lambda_2)+(K-\lambda_2)(K-\lambda_3)+(K-\lambda_3)(K-\lambda_1) = -(J_1^2+J_2^2+J_3^2) \qquad (3\text{-}14)$$

$$(K-\lambda_1)(K-\lambda_2)(K-\lambda_3) = -2J_1J_2J_3 \qquad (3\text{-}15)$$

The force constant K and λ_is (i = 1, 2, or 3) are represented by the vibrational frequencies ν_i, i = 0, 1, 2, 3, respectiely, as

$$K = (2\pi\ \nu_0)^2\mu \qquad (3\text{-}16)$$

$$\lambda_i = (2\pi\ \nu_i)^2\mu \qquad i = 1,\ 2,\ 3 \qquad (3\text{-}17)$$

where ν_0 is the unpertubed frequency, ν_1, ν_2, and ν_3 the observed frequencies. By substituting eqs 3-16 and 3-17 into eq 3-13, ν_0 is written as

$$\nu_0 = \sqrt{(\nu_1^2 + \nu_2^2 + \nu_3^2)/3} \qquad (3\text{-}18)$$

With the observed frequencies ν_1 = 1625, ν_2 = 1560, and ν_3 = 1539cm^{-1}, ν_0 is evaluated as 1575cm^{-1}. This cauclated ν_0 value agrees well with the $\nu_a(COO^-)$ frequency of zinc acetate anhydride (1572cm^{-1}).[39] Therefore, the structure of the unit is speculated to be similar to that of zinc acetate anhydride shown in Fig.3-6, although in the case of E-MA-Zn the vibrational unit is zinc methacrylate anhydride. The ordered structure present in the dry state is considered as an aggregate of three units. Such small aggregate may be regarded as a multiplet rather than a cluster. The unit cell (0.837nm^3) of $Zn(CH_3COO)_2.2H_2O$ crystal contains four formular units.[40] Corresponding radius of a sphere containing three units is 0.53nm. The result of SAXS analysis (chapter 2) indicates that the radius of the spherical ionic particle is R_1 = 0.38 - 0.40nm. Thus, the spectroscopic result is quantitatively consistent with that of the SAXS. Four oxygen atoms of the carboxylate groups in one unit are supposed to be coordinated tetrahedrally to the Zn ion with the D_{2d} point group symmetry as in zinc acetate anhydride.[39] Two $\nu_a(COO^-)$ modes in one unit belong to the doubly degenerate E species. The vibrational degeneracy within the unit is assumed to remain

unresolved by the inter-unit vibrational coupling.

Here, the magnitudes of the interunit force constants and multiplet structure will be considered. Eqs 3-16 and 3-17 give the following equation.

$$\lambda_1 / K = (\nu_1 / \nu_0)^2 \qquad (3\text{-}19)$$

With the experimental values ν_1 = 1625 and ν_0 = 1575cm^{-1}, λ_1 was obtained as 1.06K. Similarly, λ_2 = 0.981K and λ_3 = 0.955K are obtained. By substituting these values into eqs 3-14 and 3-15, two relations between J_is and K were derived.

$$J_1^2 + J_2^2 + J_3^2 = 32.4\times10^{-4}K^2 \qquad (3\text{-}20)$$

$$J_1J_2J_3 = 27.4\times10^{-6}K^3 \qquad (3\text{-}21)$$

From eqs 3-20 and 3-21, the real sets of $|J_1|$, $|J_2|$, and $|J_3|$ are limited on the solid line written in Fig.3-7 where broken lines are the projections on the $|J_3|$-$|J_1|$, $|J_1|$-$|J_2|$, and $|J_2|$-$|J_3|$ planes. The values of $|J_i|$s are two order smaller than K. At points B and C, the two of three $|J_i|$s have the same value.

$|J_i|$ corresponds to the strength of vibrational interaction between the vibrational units. Normal mode analysis for several carboxylate ions have been done and the force constants have been determined using a Urey-Bradley potential field.[41-43] However the direct comparison between these values and the present $|J_i|$s is rather difficult. From the relative magnitude of $|J_i|$s, possible structures of the multiplet are speculated. The case where the three units interact equivalently with each other $|J_1|=|J_2|=|J_3|$ (Fig.3-8 A) is not realized from eqs 3-20 and 3-21.

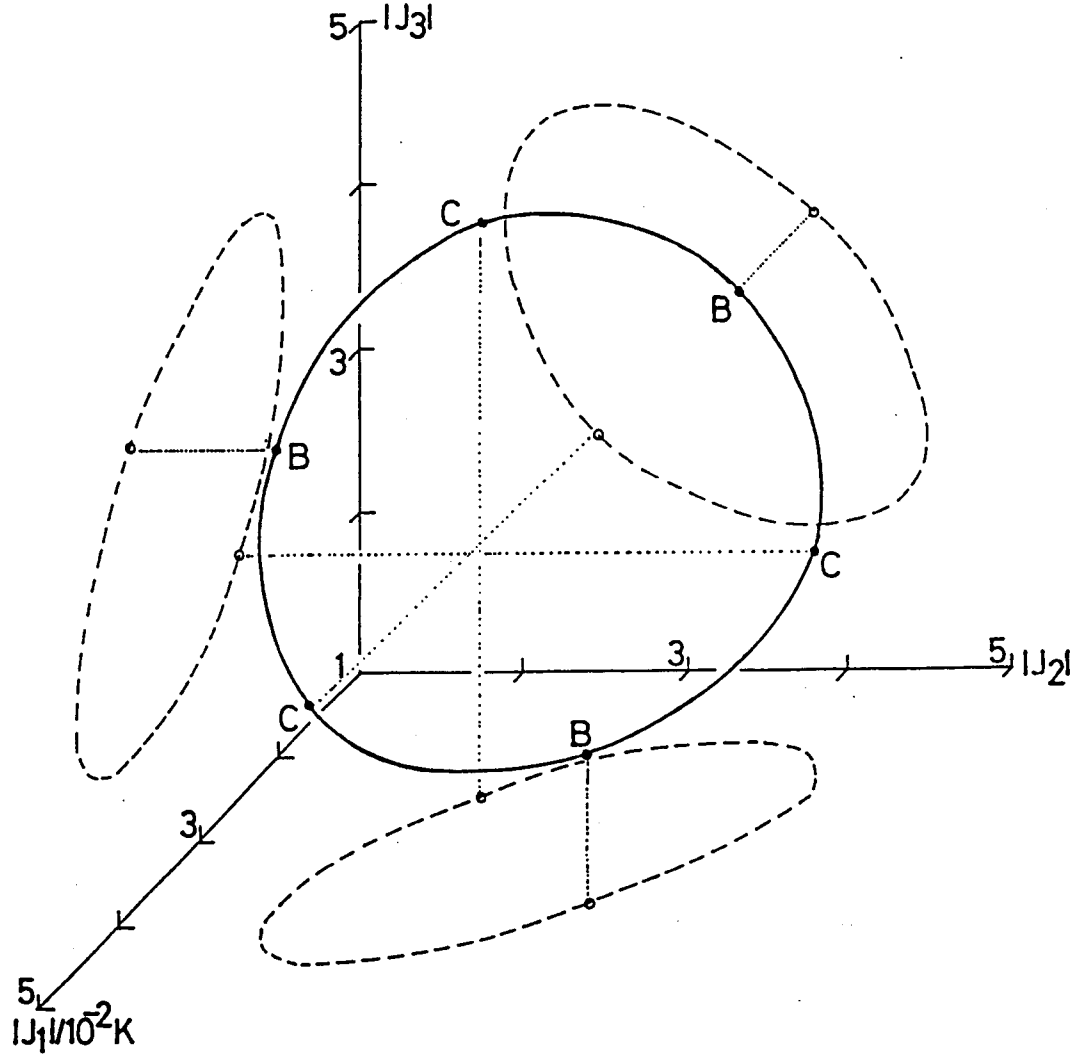

Fig.3-7. Numerical relations between $|J_1|$, $|J_2|$, and $|J_3|$. At points B and C, two of three $|J_i|$s have the same value where $i = 1, 2, 3$. Broken lines are the projections of the solid line on $|J_3| - |J_1|$, $|J_1| - |J_2|$, and $|J_2| - |J_3|$ planes.

A

$|J_1| = |J_2| = |J_3|$

no exist

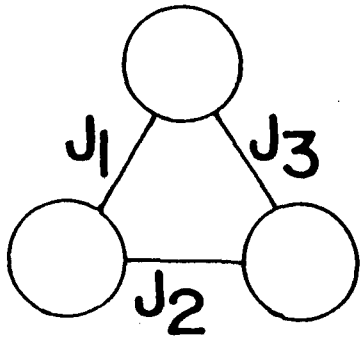

B

$|J_1| = |J_2| = 3.8 \times 10^{-2} K,$

$|J_3| = 1.9 \times 10^{-2} K.$

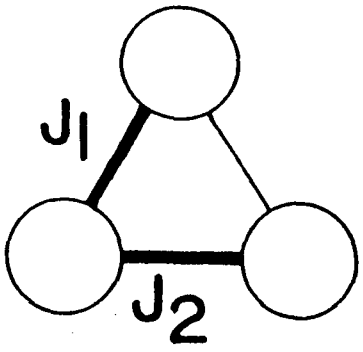

C

$|J_2| = 4.5 \times 10^{-2} K,$

$|J_1| = |J_3| = 2.5 \times 10^{-2} K.$

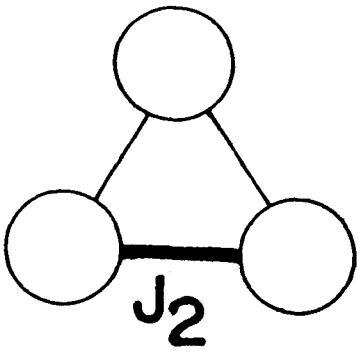

Fig.3-8. Possible structures of mutiplet, where i of J_i (i = 1, 2, 3) is not specified to that shown in B and C.

There are two cases in which two of three $|J_i|$s have the same values as shown in Fig.3-8 B and C. In the case B (corresponding to the points B in Fig.3-7), three units are aligned linearly and the interactions between the adjacent units are strong and that between the end units is weak. In the case C (points C), two units form dimer structure and the third unit interacts to the dimer. Other possible structures corresponding to the other points on the solid curve in Fig.3-7 are the intermediate between the above two extremes.

In the hydrated state of E-MA-Zn, the $\nu_a(COO^-)$ mode appears at $1587cm^{-1}$ as singlet, and $\nu_s(COO^-)$ at $1420cm^{-1}$. The single $\nu_a(COO^-)$ frequency may indicate that the vibrational interaction between the neighboring units is smeared and the three split $\nu_a(COO^-)$ components observed in dry state collapse into one band. As Nakamoto have proposed, the frequency separation between $\nu_a(COO^-)$ and $\nu_s(COO^-)$ modes, $\Delta\nu$, is often used as a measure of the coordination state of the COO^- groups to metal cation.[44] The $\nu_a(COO^-)$ and $\nu_s(COO^-)$ of a free acetate ion (structure I) are ca. 1560 and $1416cm^{-1}$, respectively and the separation is $144cm^{-1}$. In the unidentate complex (structure II) $\nu(C=O)$ is higher than $\nu_a(COO^-)$ and $\nu(C-O)$ is lower than $\nu_s(COO^-)$. As a result, $\Delta\nu$ becomes larger. The opposite trend is found in the bidentate (chelate) complex (structure III). In the bridging complex (structure IV) however two $\nu(COO)$ frequencies are close to those of free ion. These results are summarized in Table III-II.

Table III-II. Frequencies of $\nu_a(COO^-)$ and $\nu_s(COO^-)$ modes of several hydrated carboxylates and their unhydrides.

compounds	$\nu_a(COO^-)$	$\nu_s(COO^-)$	$\Delta\nu/cm^{-1}$	structure
CH_3COO^-, (ac)	1560	1416	144	free ion
$Rh(ac)(CO)(PPH_3)_2$	1604	1376	228	unidentate[45]
$Ru(ac)_2(CO)_2(PPh_3)_2$	1613	1315	298	unidentate[45]
$[Pd(ac)_2(PPh_3)]_2$	1629	1314	315	unidentate[46]
$Co(ac)_2.4H_2O$	1550	1395	155	unidentate[47]
$Ni(ac)_2.4H_2O$	1550	1425	125	unidentate[47]
$RuCl(ac)(CO)(PPh_3)_2$	1507	1465	42	bidentate[45]
$RuH(ac)(PPh_3)_2$	1526	1449	77	bidentate[45]
$Zn(ac)_2.2H_2O$	1558	1450	108	bidentate[39]
$Zn(ac)_2$	1572	1453	119	bidentate[39]
$[Pd(ac)_2(PPh_3)_2]_2$	1580	1411	169	bridging[46]
$Rh_2(ac)_2(CO)_3(PPh_2)$	1580	1440	140	bridging[48]
E-MA-Zn wet	1587	1420	167	
E-MA-Zn dry	1575†	1420	155	

†: intrinsic value.

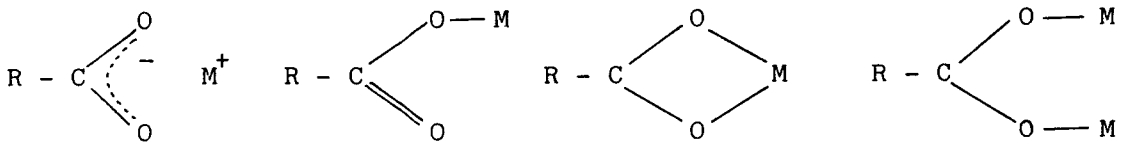

I II III IV

free ion structue | unidentate structure | chelating bidentate structure | bridging bidentate structue

By comparing the $\nu(COO^-)$ frequencies of E-MA-Zn with those of the listed carboxylate compounds, the coordination state of the COO^- groups in the moistened E-MA-Zn was considered. In the case of wet E-MA-Zn, $\Delta\nu$ is 167cm^{-1} indicating that the COO groups have unidentate character. However, the $\Delta\nu$ of E-MA-Zn is rather small compared with those of Rh, Ru, and Pd complexs. The similar tendency of small $\Delta\nu$ values was observed for $Co(CH_3COO)_2.4H_2O$ and $Ni(CH_3COO)_2.4H_2O$.[44] In a hydrated state of the E-MA-Zn about (1/2) water molecule are adsorbed on a zinc cation. Therefore the zinc cation may be surrounded tetrahedrally by two oxygens of unidentate carboxylate groups and a water molecule may be located between two zinc cations.

In a dry state of E-MA-Zn, $\Delta\nu$ is 155cm^{-1}, somewhat higher than 144cm^{-1} of free ion, indicating that the COO^- groups have a little unidentate character. The three split components observed at 1625, 1560, and 1539cm^{-1} are interpreted to be caused by the vibrational coupling between the three units. Mesubi investigated the infrared spectrum of $\nu_a(COO^-)$ band of zinc decanoate.[49] A $\nu_a(COO^-)$ band centered at 1543cm^{-1} was observed at room temperature. This band was assigned to the unsymmetric bidentate structure which corresponds to the intermediate coordination between the unidentate and the

symmetric chelating bidentate.

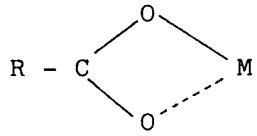

Unsymmetric chelating

bidentate structure

In the melt, the band becomes broader with the peaks at 1549, 1594, and 1634cm^{-1} like in the present ionomer. The 1634cm^{-1} component was assigned to the unidentate structure produced at high temperature, while the 1594cm^{-1} band was not assigned. Thus, in the molten state zinc decanoate was considered to be in an equilibrium between two coordination structures and the multipeak $\nu_a(COO^-)$ pattern was ascribed to their coexistence. In the case of E-MA-Zn ionomer, the multipeak $\nu_a(COO^-)$ absorption appears even in the sample dried at low temperature and parallel intensity change of the three split components occurs with the variation of water content and, therefore, the splitting should be ascribed to the vibrational coupling.

3-4. References

1) M. Pineri, C. Meyer, A. M. Levelut, and M. Lambert, J. Polym. Sci., Polym. Phys. Ed., 12, 115 (1974).

2) C. T. Meyer and M. Pineri, J. Polym. Sci., Polym. Phys. Ed., 13, 1057 (1975).

3) C. T. Meyer and M. Pineri, J. Polym. Sci., Polym. Phys. Ed., 16, 569 (1978).

4) D. J. Yarrusso, S. L. Cooper, G. S. Knapp, and P. Georgopoulos, J. Polym. Sci., Polym. Lett. Ed., 18, 557 (1980).

5) B. Rodmacq, M. Pineri, J. M. Coey, and A. Meagher, J. Polym. Sci., Polym. Phys. Ed., 20, 603 (1982).

6) J. Yamauchi and S. Yano, Macromolecules, 15, 210 (1982).

7) H. K. Pan, D. J. Yarrusso, G. S. Knapp, and S. L. Cooper, J. Polym. Sci., Polym. Phys. Ed., 21, 1389 (1983).

8) H. K. Pan, D. J. Yarrusso, G. S. Knapp, M. Pineri, A. Maegher, J. M. D. Cey, and S. L. Cooper, J. Chem. Phys., 79, 4736 (1983).

9) R. A. Weiss, J. Lefelar, and H. Toriumi, J. Polym. Sci., Polym. Lett. Ed., 21, 661 (1983).

10) H. Toriumi, R. A. Weiss, and H. A. Frank, Macromolecules, 17, 2104 (1984).

11) D. J. Yarrusso, Y. S. Ding, H. K. Pan, and S. L. Cooper, J. Polym. Sci., Polym. Phys. Ed., 22, 2073 (1984).

12) H. K. Pan, G. S. Knapp, and S. L. Cooper, Coll. Polymer Sci., 262, 734 (1984).

13) R. Jerome, G. Vlaic, and C. E. Williams, J. Physique, 44, L717 (1983).

14) G. Vlaic, C. E. Williams, R. Jerome, M. R. Tant, and G. L. Wilkes, Polymer, 29, 173 (1988).

15) A. T. Tsatsas and W. M. Risen, Jr., Chem. Phys. Lett., 7, 354 (1970).

16) A. T. Tsatsas, J. M. Reed, and W. M. Risen, Jr., J. Chem. Phys., 55, 3260 (1971).

17) M. Boyarchuk, E. D. Andreeva, L. V. Konovapov, and V. N. Nikitin, Z. Prikl. Spektr., 23, 1 (1975).

18) E. D. Andreeva, V. N. Nikitin, and Y. M. Boyartchuk, Macromolecules, 9, 238 (1976).

19) G. B. Rouse, W. M. Risen, Jr., A. T. Tsatsas, and A. Eisenberg, J. Polym. Sci., Polym. Phys. Ed., 17, 81 (1979).

20) D. G. Peiffer, B. L. Hager, R. A. Weiss, P. K. Agarwal, and R. D. Lundberg, J. Polym. Sci., Polym. Phys. Ed., 23, 1869 (1985).

21) A. Neppel, I. S. Butler, and A. Eisenberg, Macromolecules, 12, 948 (1979).

22) A. Neppel, I. S. Butler, and A. Eisenberg, J. Polym. Sci., Polym. Phys. Ed., 17, 2145 (1979).

23) A. Neppel, I. S. Butler, N. Brockman, and A. Eisenberg, J. Macromol Sci. -Phys., B19, 61 (1981).

24) P. C. Painter, B. A. Brozoski, and M. M. Coleman, J. Polym. Sci., Polym. Phys. Ed., 20, 1069 (1982).

25) B. A. Brozoski, M. M. Coleman, and P. C. Painter, J. Polym. Sci., Polym. Phys. Ed., 21, 301 (1983).

26) B. A. Brozoski, M. M. Coleman, and P. C. Painter, Macromolecules, 17, 230 (1984).

27) B. A. Brozoski, P. C. Painter, and M. M. Coleman, Macromolecules. 17, 1591 (1984).

28) A. Eisenberg, Macromolecules, 3, 147 (1970).

29) A. Eisenberg, J. Polym. Sci., polym. Symp., 45, 99 (1974).

30) K. O. Hartman, G. L. Carlson, R. E. Witkowski, and W. G. Fateley, Spectrocim. Acta, 24A, 157 (1968).

31) M. Okazaki, I. Hara, and T. Fujiyama, J. Phys. Chem., 80, 64 (1976).

32) M. Kobayashi and S. Kawabata, Spectrocim. Acta, 33A, 549 (1977).

33) T. Ishioka and M. Kobayashi, Rep. Pro. polym. Phys. Jpn., 29, 195 (1986).

34) P. Debye, Polar Molecules (Chemical Catalog Campany Inc., New York, 1929).

35) R. Menke, Discussion Faraday Soc., 9, 161 (1950).

36) S. R. Polo and M. K. Wilson, J. Chem. Phys., 23, 2376 (1955).

37) L. Onsager, J. Am. Chem. Soc., 58, 1486 (1936).

38) Landort-Börnstein, "Zahlenwerte und Funktionen aus Physik, Chemie, Astoronomie, Geophysik und Technik", Sechste Auflage, II. Band, Eigenschaften der Materie in Ihren Aggregatzuständed, 8 Teil, Optishe Konstanten, Springer-Verlag, Berlin, 1962.

39) M. K. Johnson, D. B. Powell, and R. D. Cannon, Spectrochim. Acta, 37A, 899 (1981).

40) J. N. Niekerk, F. R. Schoening, and H. Talbot, Acta Cryst., 6, 720 (1953).

41) T. Miyazawa, J. Chem. Soc. Jpn., 77, 381 (1956).

42) K. Nakamura, ibid., 79, 1411 (1958).

43) K. Nakamura, ibid., 79, 1420 (1958).

44) K. Nakamoto, "Infrared and Raman Spectra of Inorganic and Coordination Compounds", 3rd Ed., Wiley-Interscience, New York, 1978.

45) S. D. Robinson and M. F. Uttley, J. Chem. Soc., 1912 (1973).

46) T. A. Stephensen and G. Wilkinson, J. Inorg. Nucl. Chem., 29, 2122 (1967).

47) D. A. Edwards and R. N. Hayward, Can. J. Chem., 46, 3443 (1968).

48) G. Csontos, B. Heil, and C. Marko, J. Organometal. Chem., 37, 183 (1972).

49) N. A. Mesubi, J. Mol. Struct., 81, 61 (1982).

Chapter 4

Phase Transition of Ion-containing Long-chain Compounds

4-1. Introduction

In chapter 1, it is revealed that presence of the ionic groups affected the thermally induced disordering process of trans methylene chains accomodated in the non-crystalline region of the polyethylene-based E-MA ionomers. In order to clarify in more detail the role of ionic groups, investigation of some model compounds may give us more convinced information. The author investigates crystalline low molecular-weight compounds having alkyl chains and an ionic group in the individual molecule in this chapter. Long-alkyl carboxylate salts are the most suitable materials for the purpose because of structural similarity between them and the E-MA ionomers. But it has been known that their structures and transition behaviors were significantly influenced by the trace amount of residual water in the specimen and complete dehydration of them was difficult as described in chapter 3. In stead of them, the author investigated the N, N'-dialkylbicyclo(2,2,2)octane (DABCO) halides and 1-alkyl-4-aza-1-azoniabicyclo(2,2,2)octane bromides having the alkyl chains and the quaternary ammonium ions in the bicycloring group in an individual molecule. Their structures and phase transition behaviors are also affected by the content of water but their anhydrides are preparable more easily than those of alkyl carboxylates.

A series of them was synthesized by Nogami et al.[1-5] These compounds exhibit charactersitic solid-state phase transitions accopanied by an abrupt increase of ionic conductivity. A series of symmetric bis-alkyl DABCO halides having two identical alkyl chains R and quaternary ammonium ions in the bicycloring

exhibits a one-step transition.

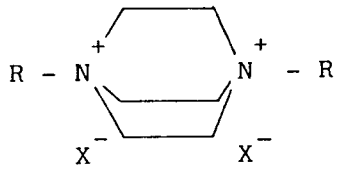

R = n-C$_n$H$_{2n+1}$

X = Cl, I, Br

For example, the low-temperature (LT) form of N, N'-distearyl-1,4-diazabicyclo(2,2,2)octane bromide with R = n-C$_{18}$H$_{37}$ (abbreviated as C$_4$-DABCO-C$_{18}$-Br$_2$ according to the notation by Shimizu et al.) transforms to the high temperature (HT) form at 93^{o}. The ionic conductivity increases abruptly by three order of magnitude (from 10^{-8} to 10^{-5} Sm^{-1}) at the transition temperature. The enthalpy and entropy changes of this transition have been measured as 105.5kJmol^{-1} and 288Jmol^{-1}K^{-1} (8.00Jmol^{-1}K^{-1} per CH$_2$ group), respectively.

On the contrary, 1-alkyl-4-aza-1-azoniabicyclo(2,2,2)octane bromides (denoted as C$_n$-DABCO-Br) having only one R = n-C$_n$H$_{2n+1}$ substituent, exhibits a two-step transition. The transition temperature are denoted as T_{c1} (lower) and T_{c2} (higher).

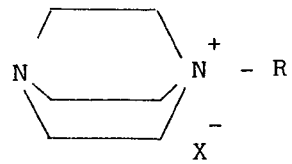

The transition enthalpy at T_{c1} was almost common to the homologous series (30kJmol^{-1}) irrespective of the chain length of R. The conductivity jump by about one order of magnitude occurs only at T_{c2}.

In this chapter, the molecular mechanism of these very characteristic transitions was investigated by means of

vibrational spectroscopic method. Efforts are focused to clarify the changes in conformation and packing of the hydrocarbon chains as well as in mobility of the bicycloring which occur on each step of the phase transition. The structures and their changes are considered in relation to the electric conductivity and the thermal behaviors. Based on the results, the effect of the ionic groups on the non-ionic alkyl chain groups is discussed.

4-2. Experimentals

4-2-1. Samples

C_{18}-DABCO-C_{18}-Br_2 synthesized by the method of Shimizu et al.[1,2] was recrystallized from methanol, and dried at 60 °C under vacuum until a constant weight is obtained. Absence of residual water was confirmed by the elementary analysis. A rectangular-shaped single-crystal of C_{22}-DABCO-C_{18}-Br_2 having a size of 4x2mm x50 μm (thickness) was grown from a methanol solution. Diazabicyclo(2,2,2)octane was purchased from Tokyo Kasei. Powder samples of C_n-DABCO-C_n-I_2, n = 1, 2, 10, 12, 16, C_{16}-DABCO-C_{16}-Cl_2, C_{22}-DABCO-C_{22}-Br_2, C_{17}-DABCO-Br, and C_{22}-DABCO-Br supplied from Prof. Nogami were used without further purification. The absence of water in the powder samples was confirmed by Nogami from the neglect contribution of the proton conduction of water to their ionic conductivity.

4-2-2. Raman and IR Measurements

The instruments used in the Raman and IR measurements are described in chapter 1. Powder sample sealed in a glass capillary was subjected to the Raman measurement. The fluorescence background was removed by irradiating the sample by the incident laser beam for several hours at a temperature above the transition point of the respective sample. The widths of the entrance and intermediate slits of the spectrometer were fixed at 200 μm (3.9cm^{-1}). Spectra at elavated temperature were taken using a home-made heating cell controlled with a deviation less than ±0.5 °C. Infrared spectra of the powder samples were taken by the nujol-mull method. A single-crystal specimen

having a rectangular plate shape was subjected to the polarization measurement using a wire-glid polarizer. The brank area of the optical path was masked with an aluminum foil.

4-3. Results and Discussion

4-3-1. Structures and Assigment of the Spectral Bands

The present compounds have one or two alkyl chains linked to a bicycloring of DABCO. The spectral bands are divided approximately into three classes: those associated with (1) the alkyl chains, (2) the bicycloring, and (3) the chain-ring coupling. The Raman spectra of C_{18}-DABCO-C_{18}-Br (as a typical example of the series of C_n-DABCO-C_n-X_2) measured at room temperature is reproduced in Fig.4-1. The strong bands appearing in the frequency ranges 3000 - 2800, 1500 - 1400, 1300, and 1130- 1050cm^{-1} are associated with the hydrocarbon chains. They are assigned as follows; the 2895cm^{-1} band: the antisymmetric CH stretch $\nu_a(CH_2)$, the doublets in 1500 - 1400cm^{-1} : the CH scissoring $\delta(CH_2)$, the 1298cm^{-1} : the CH twisting $t(CH_2)$, the 1130cm^{-1} band: the symmetric CC stretch $\nu_s(CC)$, the 1060cm^{-1} band: the antisymmetric CC stretch $\nu_a(CC)$. The intensities and shapes of these bands are sensitive to the conformation of the alkyl chains; they appear as very sharp and strong bands only when the alkyl chains are in the all-trans conformation, and decrease in intensity with an increase of the amount of the conformational defects (containing the gauche conformation).[6-10] In the chains having a disordered form like in liquid paraffins, the sharp band profiles disappear and are converted to very broad bands. Therefore, the intensities of

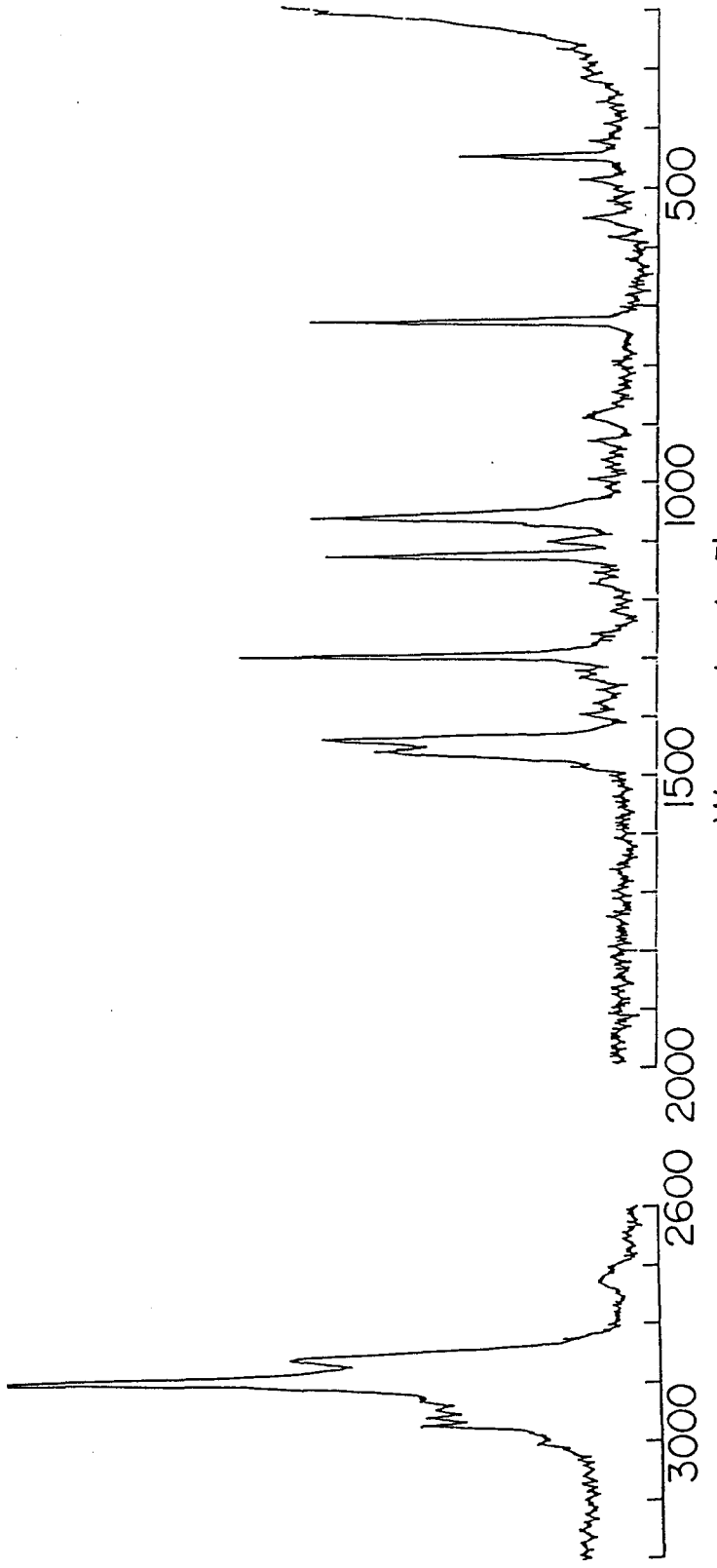

Fig.4-1. Raman spectrum for C_{18}-DABCO-C_{18}-Br_2 at room temperature.

these sharp bands are used as a measure of the conformational orderliness of the hydrocarbon chains.

In solid states, the hydrocarbon chains pack together forming one of the specific subcell structures. The subcell are roughly divided into three classes as shown in Fig.4-2: (1) the $O_{\perp}$ type where the zig-zag planes of the nearest neighboring chains are located nearly perpendicular to each other, (2) the $T_{//}$ type where the zig-zag planes are parallel to each other, and (3) the hexagonal type with rotationally disordered orientation of the zig-zag planes.

The parallel (//) and perpendicular ($\perp$) alignments of the hydrocarbon chains produce quite different patterns of the band splitting due to the interchain interactions, giving rise to different profiles of the δ(CH$_2$) and CH$_2$ rocking r(CH$_2$) bands. In Raman spectrum, the $O_{\perp}$ type subcell gives rise to a sharp band with the (c_{-1s} c_s) polarization, where subscript s means subcell, at 1416cm^{-1} in addition to the rather broad band with the (a_s b_s) polarization having two or three peaks (due to the Fermi resonance splitting with the overtones of the r(CH$_2$) modes) in the 1500 - 1450cm^{-1} range. In infrared spectrum, the r(CH$_2$) band splits into two components at 731 B_{1u} (a_s-polarized) and 720cm^{-1} B_{2u} (b_s-polarized), and the δ(CH$_2$) band into the 1473 B_{1u} (a_s) and 1463cm^{-1} B_{2u} (b_s) components.

In the $T_{//}$ subcell, the 1416cm^{-1} Raman band of δ(CH$_2$) A_g is absent and the infrared δ(CH$_2$) and r(CH$_2$) bands appear as singlet and show polarization perpendicular and parallel to the a_s axis of the $T_{//}$ subcell, respectively. In the hexagonal packing, the spectra pattern is very similar to that of the $T_{//}$

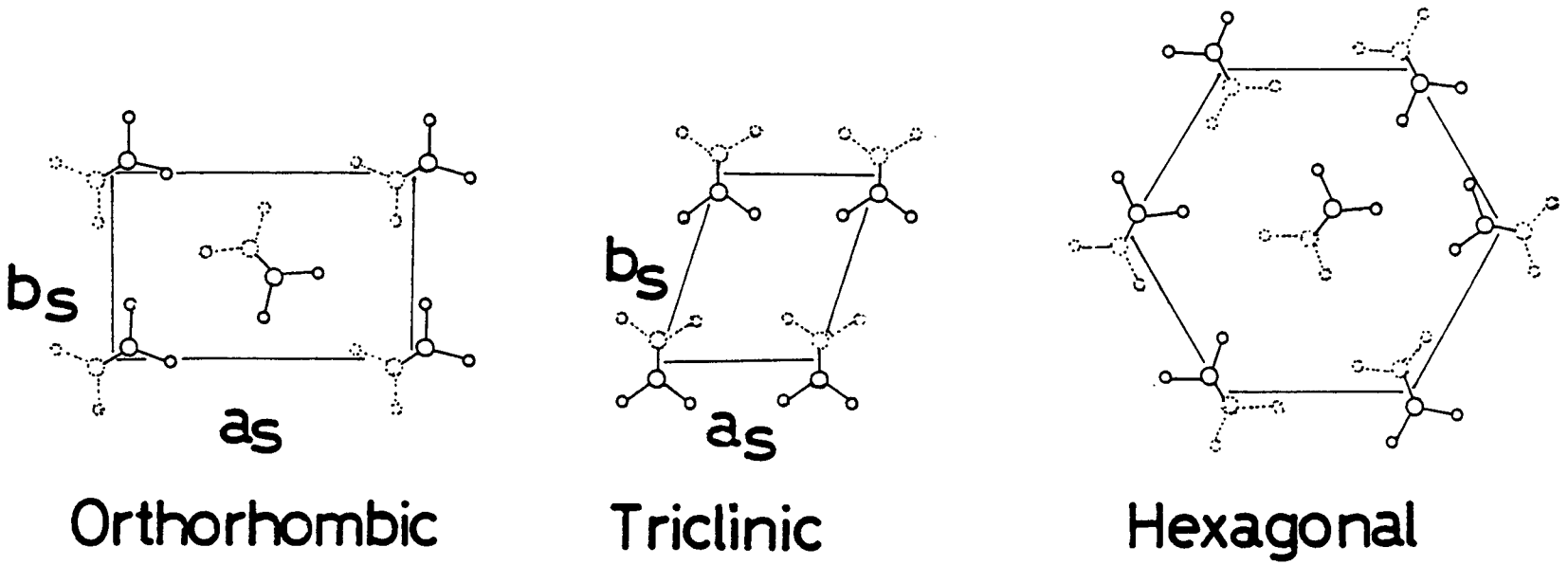

Fig.4-2. Orthorhombic ($O_{\perp}$), triclinic ($T_{//}$), and hexagonal subcell structures of the hydrocarbon chains.

type, but there are no specific polarization. Thus, from the infrared and Raman spectral profiles of $\delta(CH_2)$ and $r(CH_2)$ bands, the type of the packing of the alkyl chains in the present components can be distinguished.

In the Raman spectra of all the C_n-DABCO-C_n-X_2 samples, there are three bands at about 446, 727, and 888cm^{-1}. As a typical example, the spectra of C_n-DABCO-C_n-I_2, n = 1, 2, 12, 16, and that of DABCO as a reference are shown in Fig.4-3. These band positions are almost independent of the chain length and are shifted a little toward the low-frequency side as the halogen anion varies from Cl^- to Br^- and I^- as shown in the spectra of C_{16}-DABCO-C_{16}-X, X = Cl, Br, I (Fig.4-4). The molecular symmetry of DABCO is and also of C_{16}-DABCO-C_{16}-X may be D_{3h} having Raman active A_1', E', E'' symmetry species. Although the molecular symmetry of C_n-DABCO-C_n-X ($n \geq 2$) may be lowered to C_{2v} by the presence of two alkyl chains, local C_{3v} symmetry of the bicyclo ring group having Raman active A_1 and E species may still persist. $A_1'(C_{3v})$ corresponds to A_1' and A_1'' (D_{3h}) and $E(C_{3v})$ to E' and E'' (D_{3h}), respectively. Based on this fact along with the result of the vibrational analysis of DABCO,[11,12] these bands are assigned to the bicycloring modes; the 446cm^{-1} band: the symmetric CNC bending $\delta(CNC)$ A_1, the 727cm^{-1} band: the totally symmetric NC stretch $\nu(NC_4)$ A_1, and the 888cm^{-1} band: the degenarate NC stretch $\nu(NC_4)$ E. The splittings observed in the spectrum for C_2-DABCO-C_2-I in Fig.4-3 might be caused by the intermolecular interactions (crystal field splitting).

4-3-2. Transition of C_{18}-DABCO-C_{18}-Br

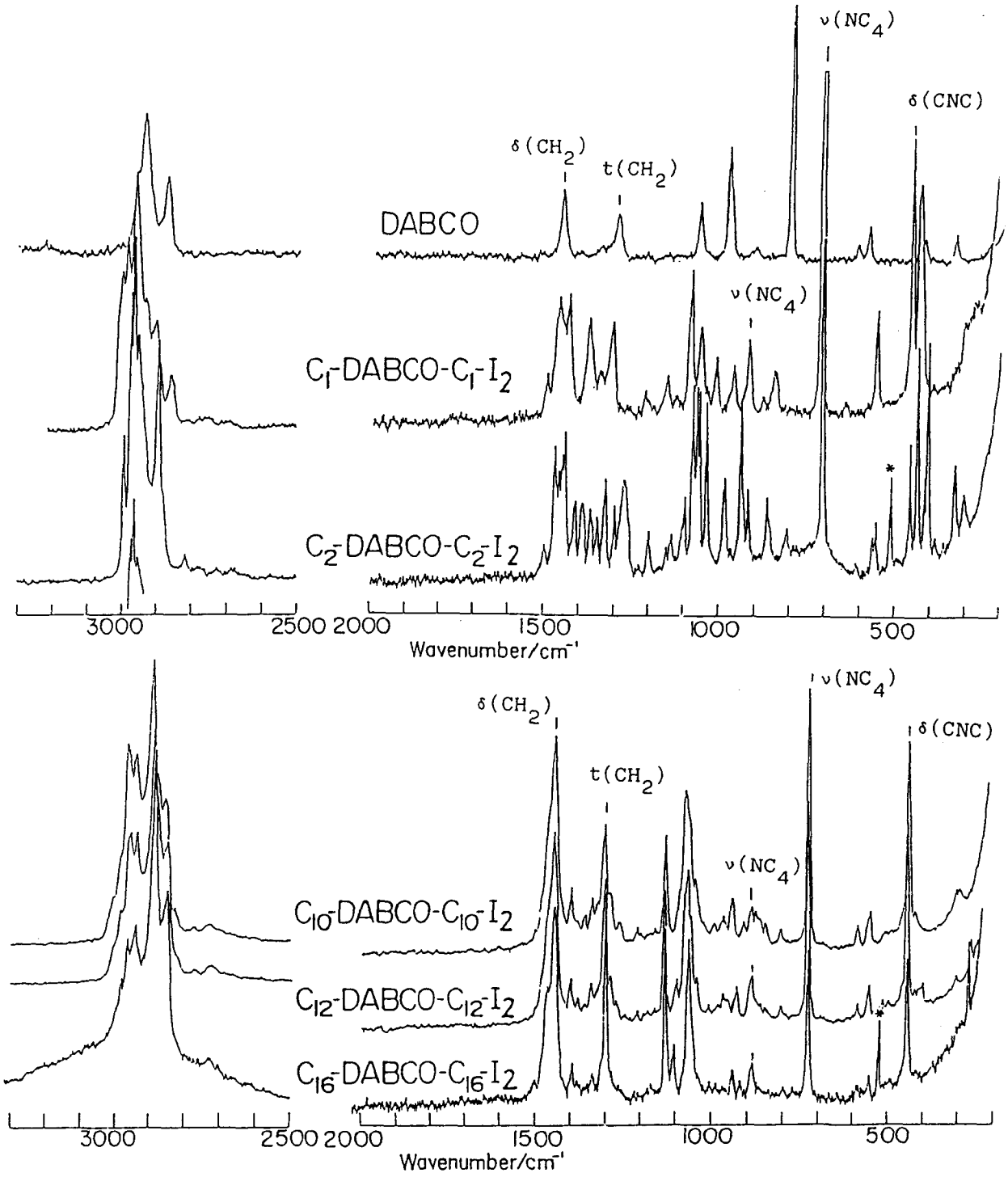

Fig.4-3. Raman spectra for DABCO and C_n-DABCO-C_n-I_2, n = 1, 2, 10, 12, 16 at room temperature. Lines marked with asterisks are due to the natural emission from Ar^+ laser.

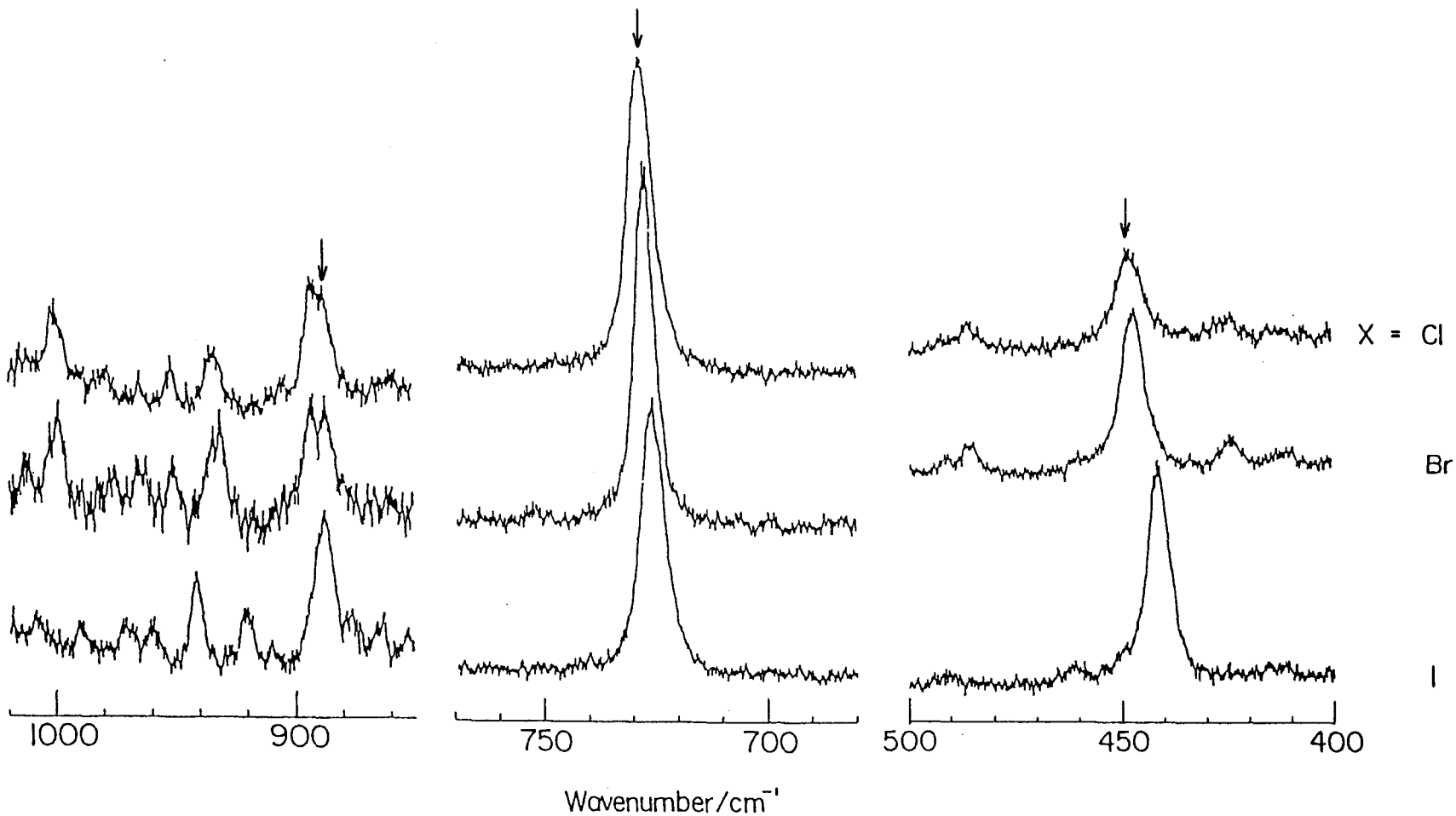

Fig.4-4. Raman spectra for C_{16}-DABCO-C_{16}-X_2, X = Cl, Br, I at room temperature.

a) Structural Changes of Alkyl Chain

The infrared and Raman band shapes in the $\delta(CH_2)$ region reflect the subcell structure of the hydrocarbon chain. In the powder Raman spectrum measured at 14 °C (Fig.4-5) the band with the peaks at 1439, 1461, and 1489 cm^{-1} is characteristic of the $T_{//}$ or hexagonal sublattice.[13-17] Two types of sublattices are not distinguished by this Raman spectrum of the powder sample. In order to decide the sublattice type, polarized IR spectra were observed on a single-crystal specimen. The infrared bands due to the $\delta(CH_2)$ ($\perp$) and $r(CH_2)$ mode and the rocking-twisting progressive band series (//) of the rectangular crystal of C_{18}-DABCO-C_{18}-Br_2 show dichroism perpendicular and parallel, respectively, to the longer edge of the single crystal (Fig.4-6), indicating that the subcell is of the $T_{//}$ type.

A broadening of the band occurs above the transition point (Fig.4-5) indicating that the packing becomes disordered. On heating, the 1295 cm^{-1} $t(CH_2)$, 1130 cm^{-1} $\nu_s(CC)$, and 1060 cm^{-1} $\nu_a(CC)$ bands keep their intensities almost unaltered up to immediately below the transition temperature (Fig.4-7) and disappear abruptly at the transition point. The spectral change takes place reversibly with a certain hysteresis on a cyclic temperature change. The abrupt melting behavior of the alkyl chains occurs in the homologous series of C_n-DABCO-C_n-X_2, temperature dependence of the Raman spectra for X = I (n = 10, 12), X = Cl (n = 16), and X = Br (n = 22) being shown in Fig.4-8. This structural change of the alkyl chains in C_n-DABCO-C_n-X_2 is similar to that in phospholipids from L_β, to L_α phase.[18]

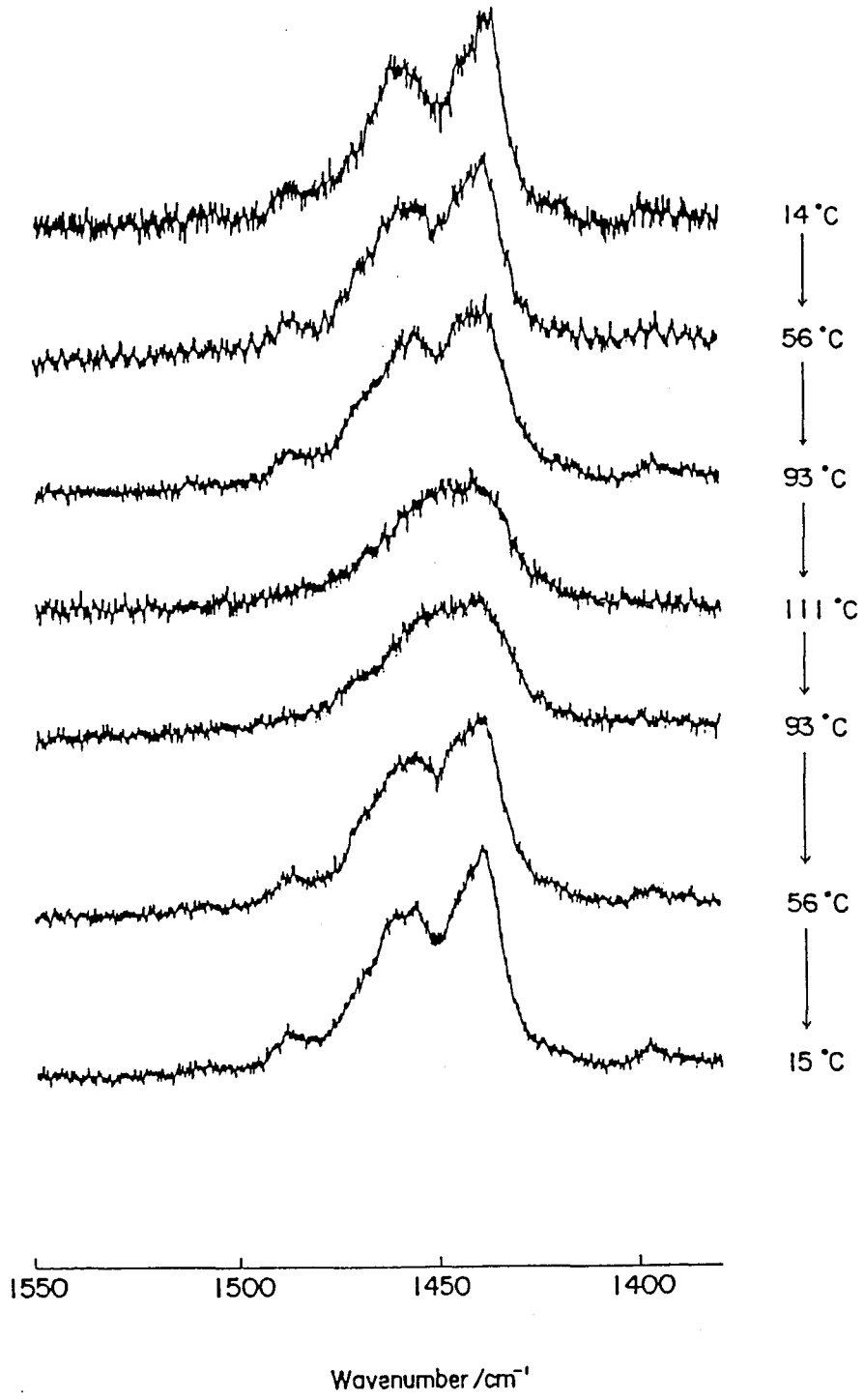

Fig.4-5. $\delta(CH_2)$ band for C_{18}-DABCO-C_{18}-Br_2 at various temperatures.

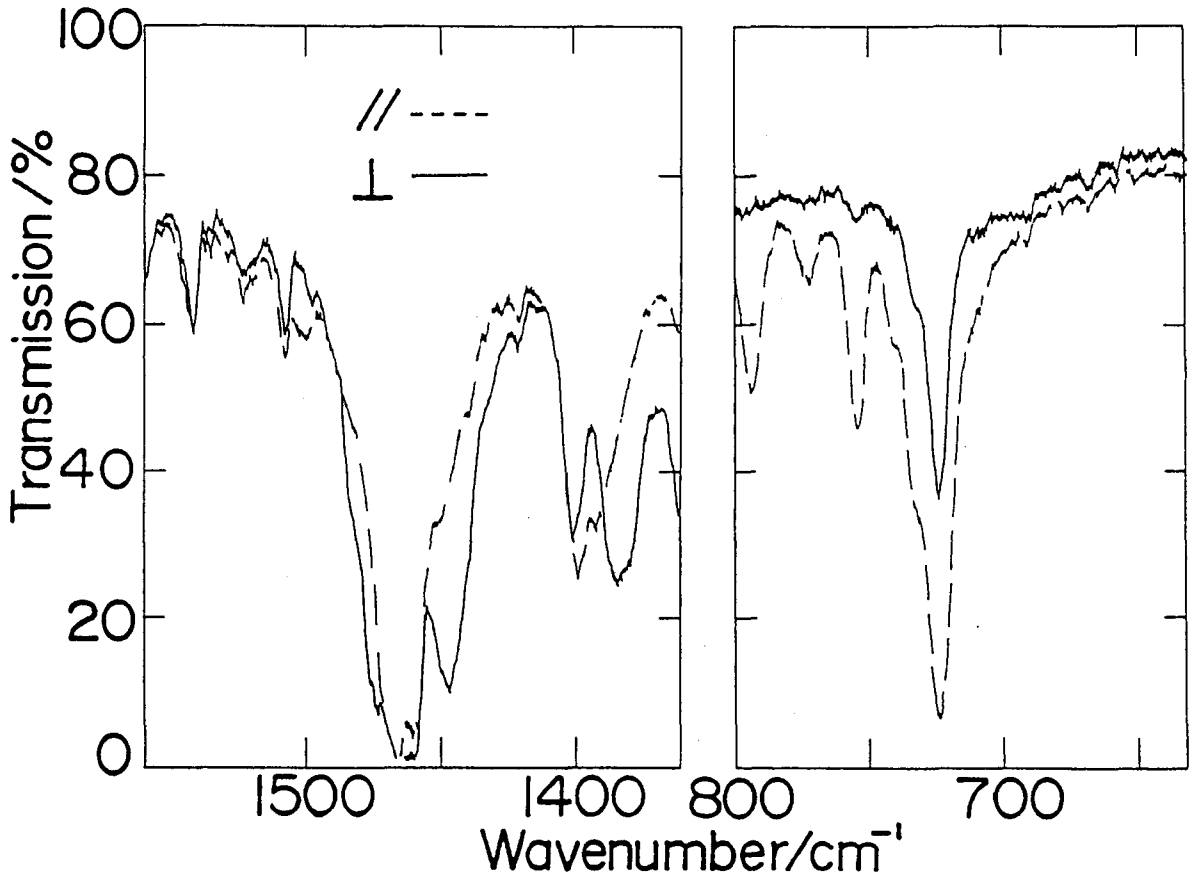

Fig.4-6. Polarized IR spectra for C_{18}-DABCO-C_{18}-Br_2 at room temperature with parallel (//) and perpendicular ($\perp$) polarizations to the longer edge of the rectangular crystal.

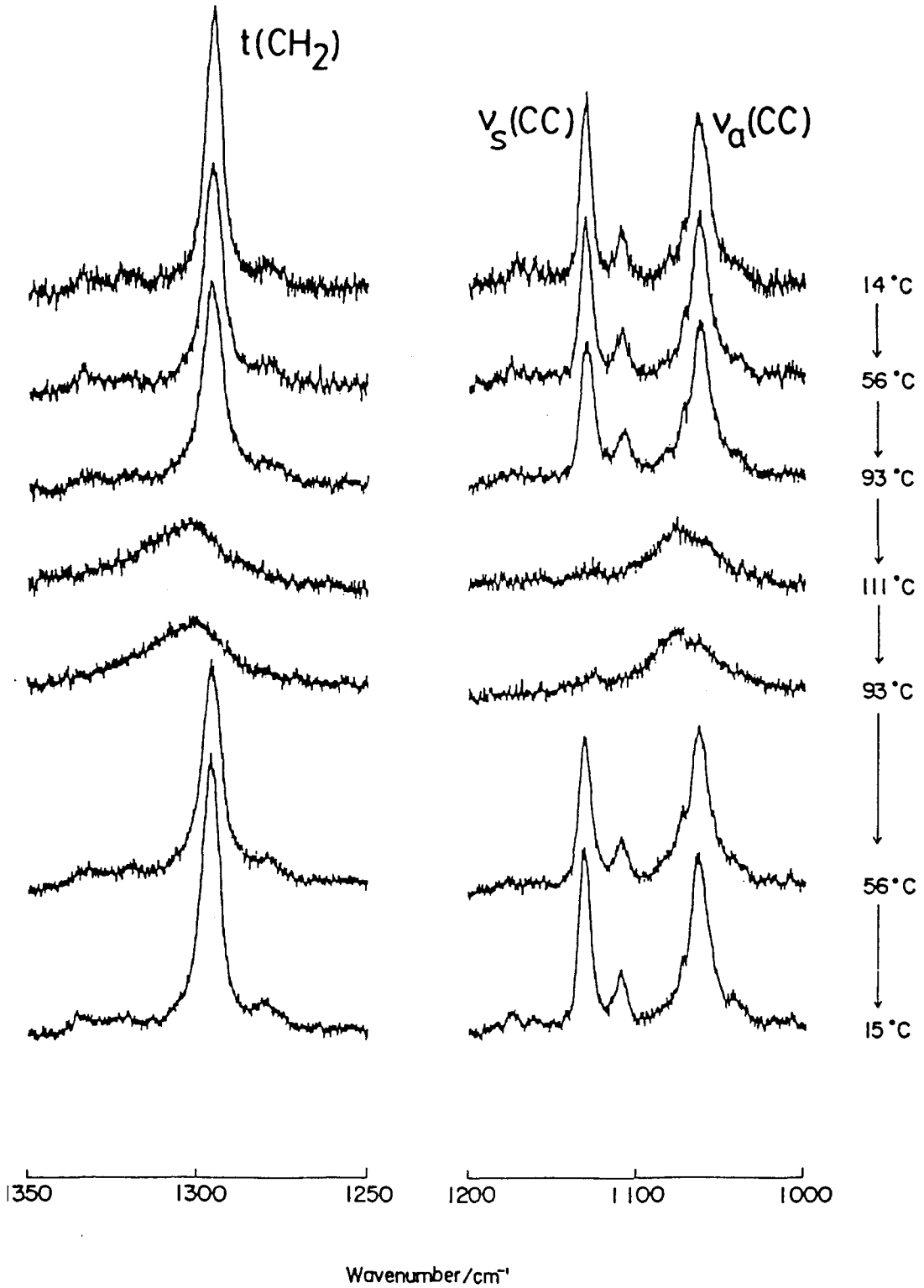

Fig.4-7. $t(CH_2)$ and $\nu(CC)$ band for C_{18}-DABCO-C_{18}-Br_2 at various temperatures.

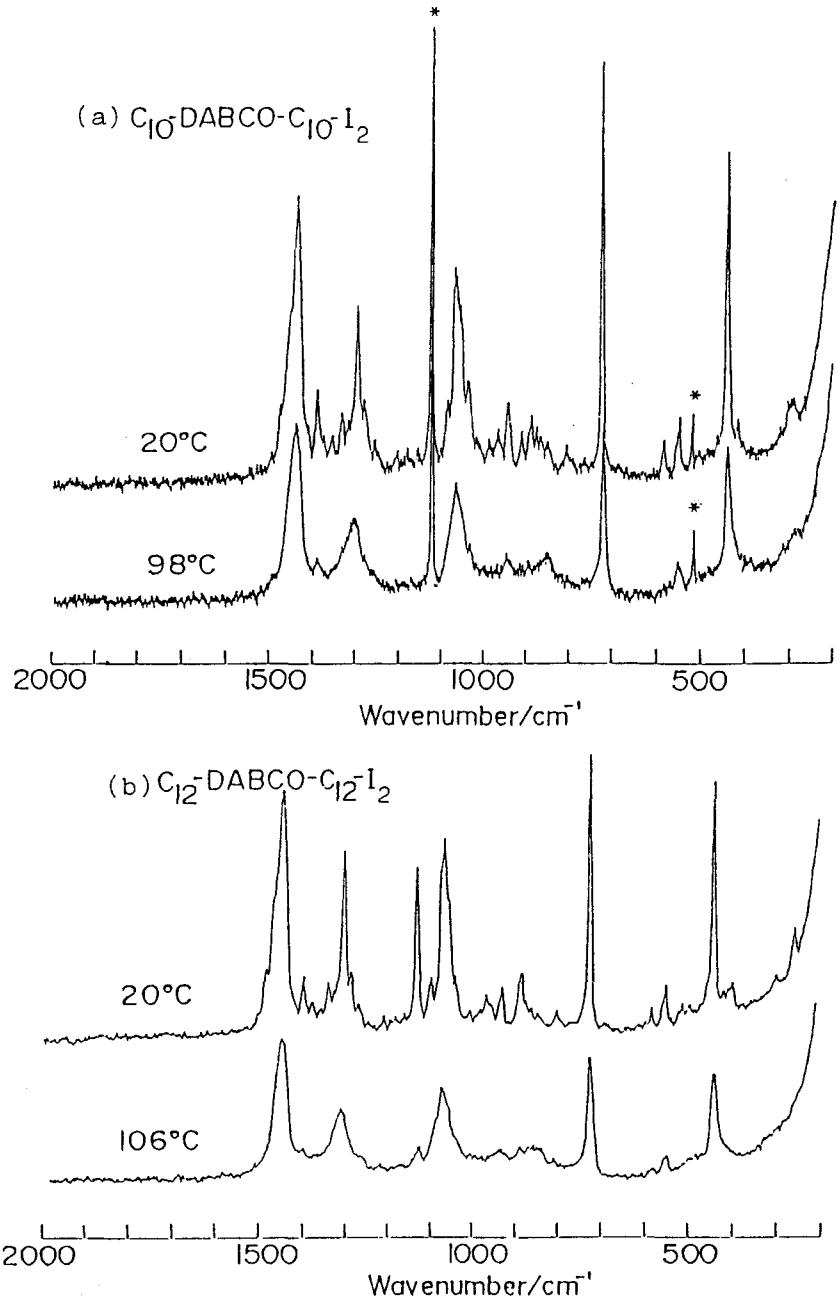

Fig.4-8. Temperature dependence of Raman spectra for (a) C_{10}-DABCO-C_{10}-I_2, transition temperature on heating T_c = 87°C, (b) C_{12}-DABCO-C_{12}-I_2, T_c = 93°C. The lines marked with asterisks are due to the natural emission from Ar^+ laser

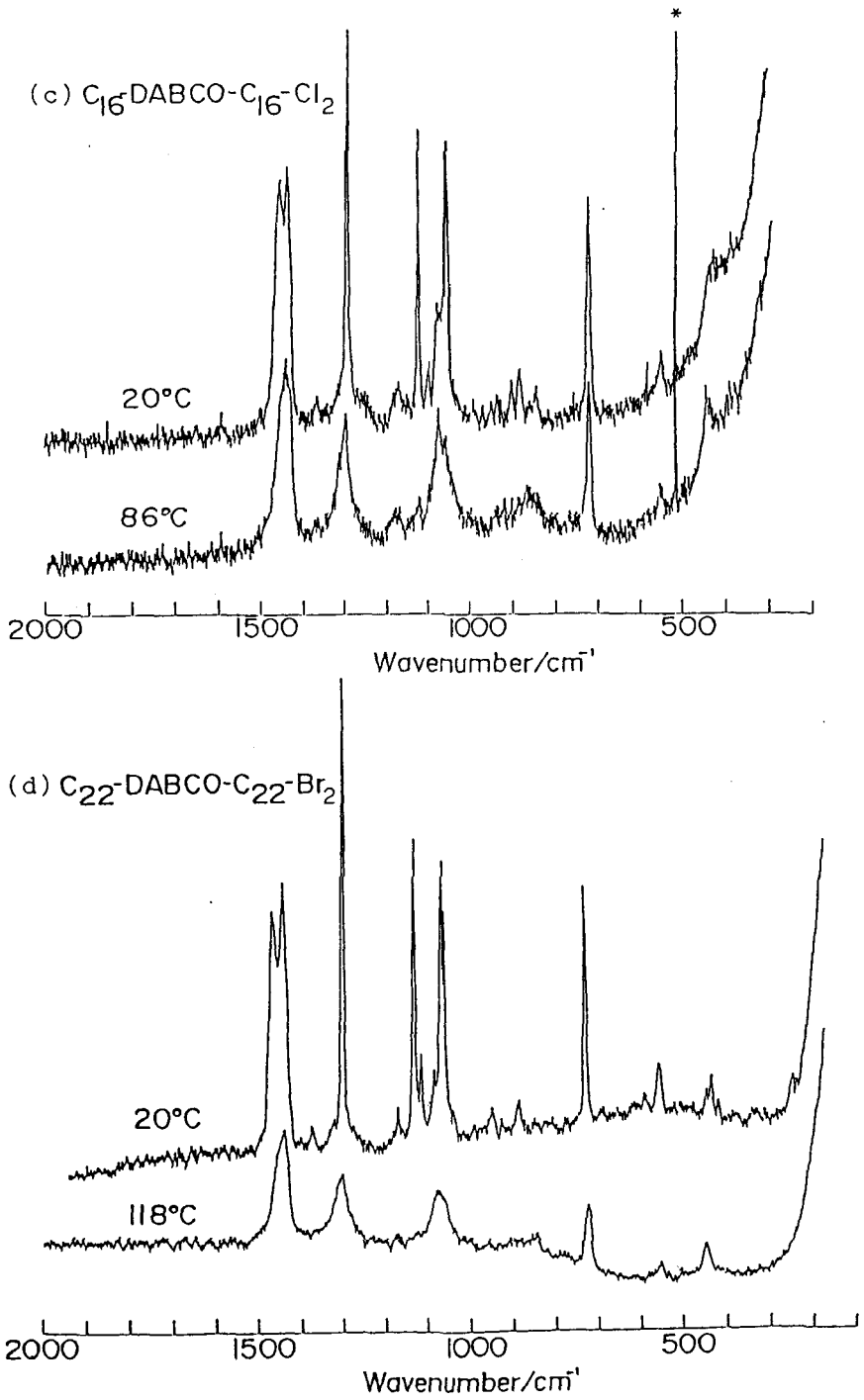

Fig.4-8. (Continued) (c) C_{16}-DABCO-C_{16}-Cl_2, T_c = 73°C, (d) C_{22}-DABCO-C_{22}-Br_2, T_c = 99°C. The lines marked with asterisks are due to the natural emission from Ar^+ laser.

b) Changes in Band Width of the Bicyclo-ring Modes

Temperature dependence of the ν_s (NC$_4$) and δ (CNC) bands both of the A_1 species are shown in Fig.4-9. A discontinuous decrease in intensity along with a substantial broadening of the band-width occurs at the transition point 93 °C. The spectral change occurs apparently a little above the transition point since the difference of temperatures between at the sample and at thermocuple in the heating cell. With increasing temperature above the transition point, further broadening and intensity depression were not observed (Fig.4-10). Temperature dependence of the band shape of the ν_a (NC$_4$) band (E species) is different from those of the above two A_1 bands as shown in Fig.4-11. Above the transition point, this band is broadened very remarkably with increasing temperature and almost disappears above 105 °C. Therefore, the temperature dependence of the band profile, especially in the band-width, above the transition temperature is different between those of the A_1 modes and that the E mode. The values of $\Delta\nu_{1/2}$ for the 727cm^{-1} ν_4 (NC$_4$) A_1 and 888cm^{-1} E bands are plotted against 1/T in Fig.4-12, where $\Delta\nu_{1/2}$ is the full-half-width of each band.

Cho et al. have found that temperature dependence of the band-width depends on the symmetry species and the polarization component of the mode for the case of high temperature phase of urea inclusion adduct of n-$C_{20}H_{42}$.[19] Using a site hopping model, they derived the correlation function of the transition dipole moment and the Raman tensor and interpreted that the temperature dependence of the band-width was caused by the

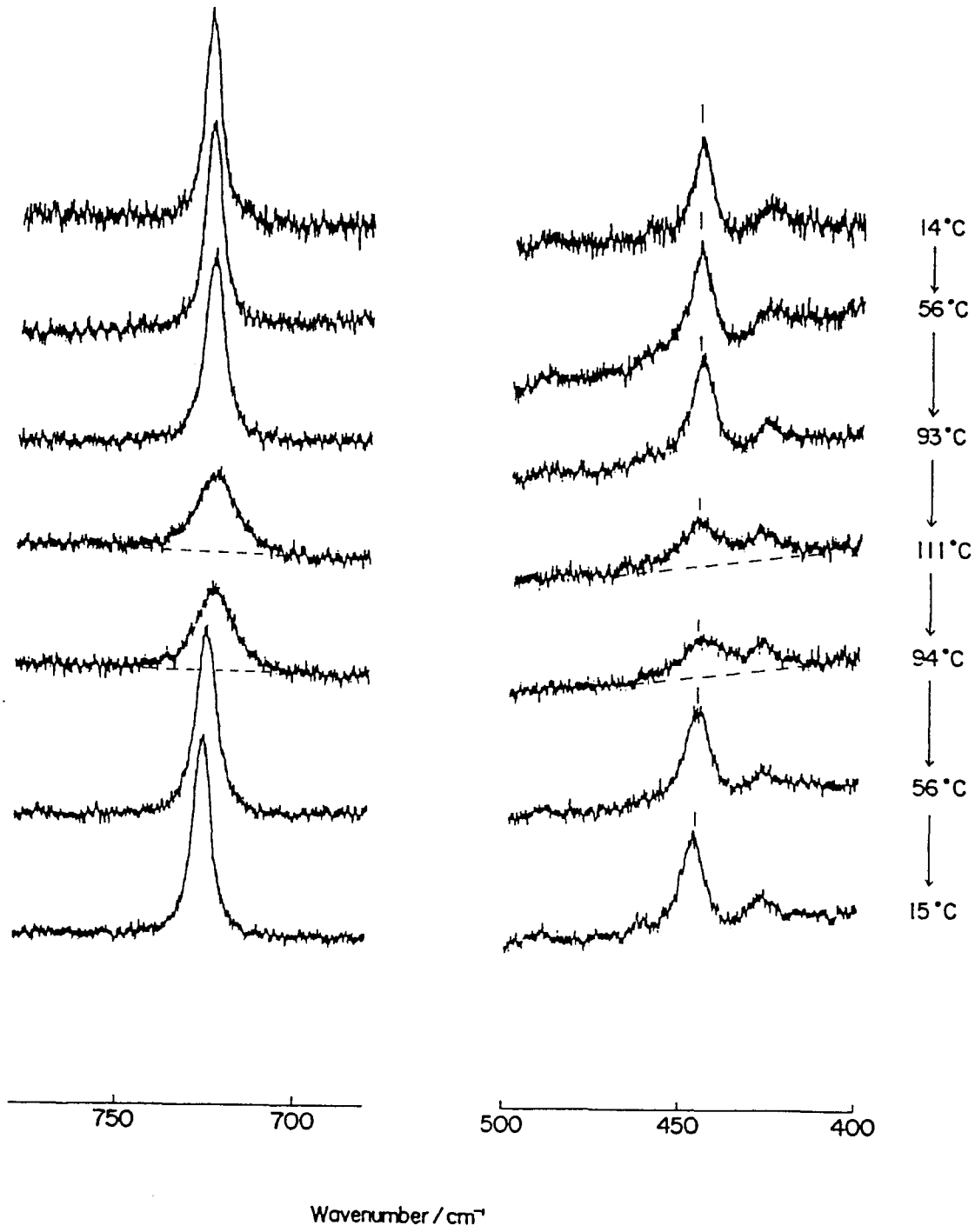

Fig.4-9. $\nu(CN_4)$ A_1 and $\nu(NC_4)$ A_1 mode for C_{18}-DABCO-C_{18}-Br_2 at various temperatures.

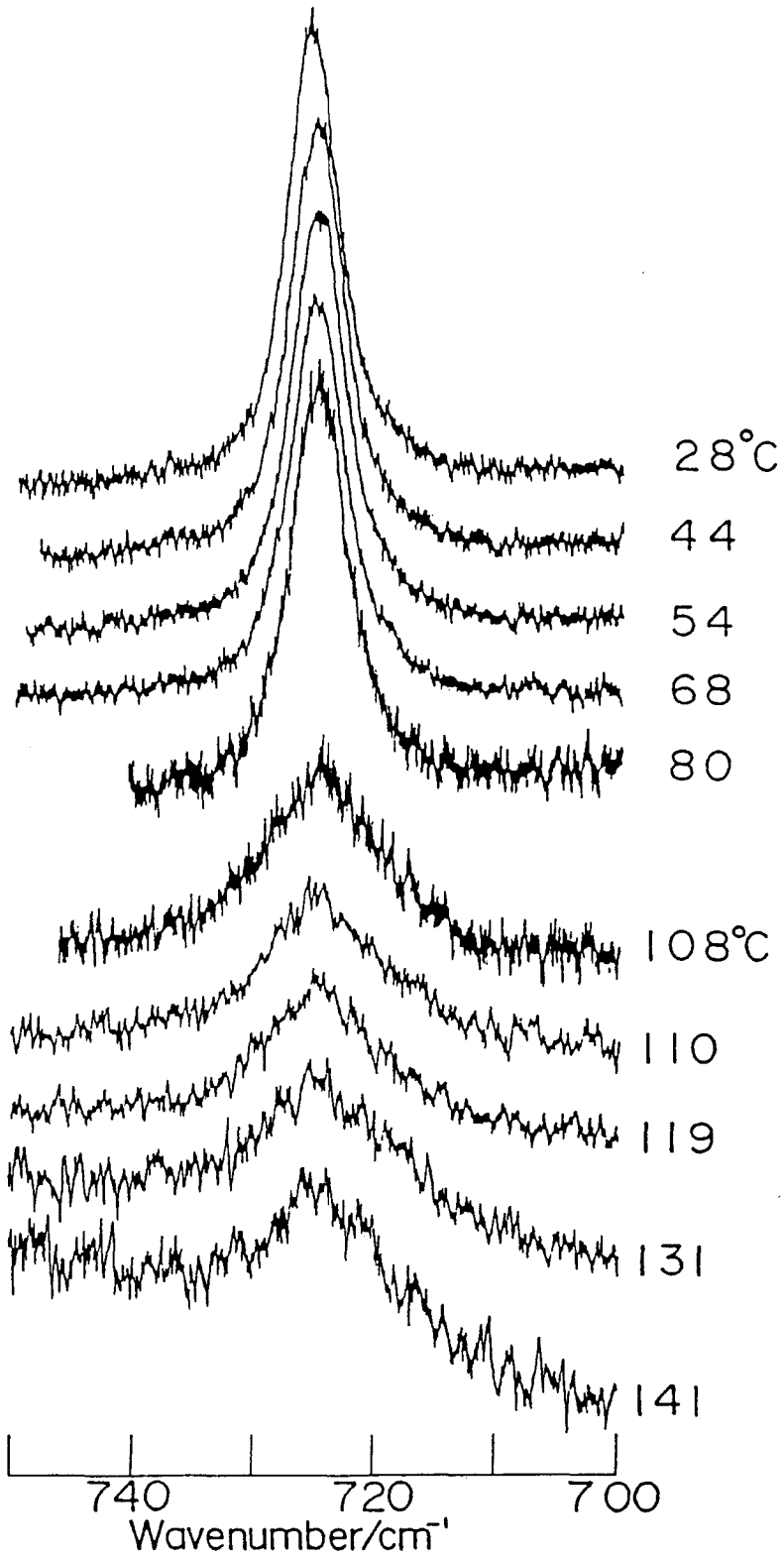

Fig.4-10. Band-widths of $\nu(NC_4)$ A_1 mode at various temperatures.

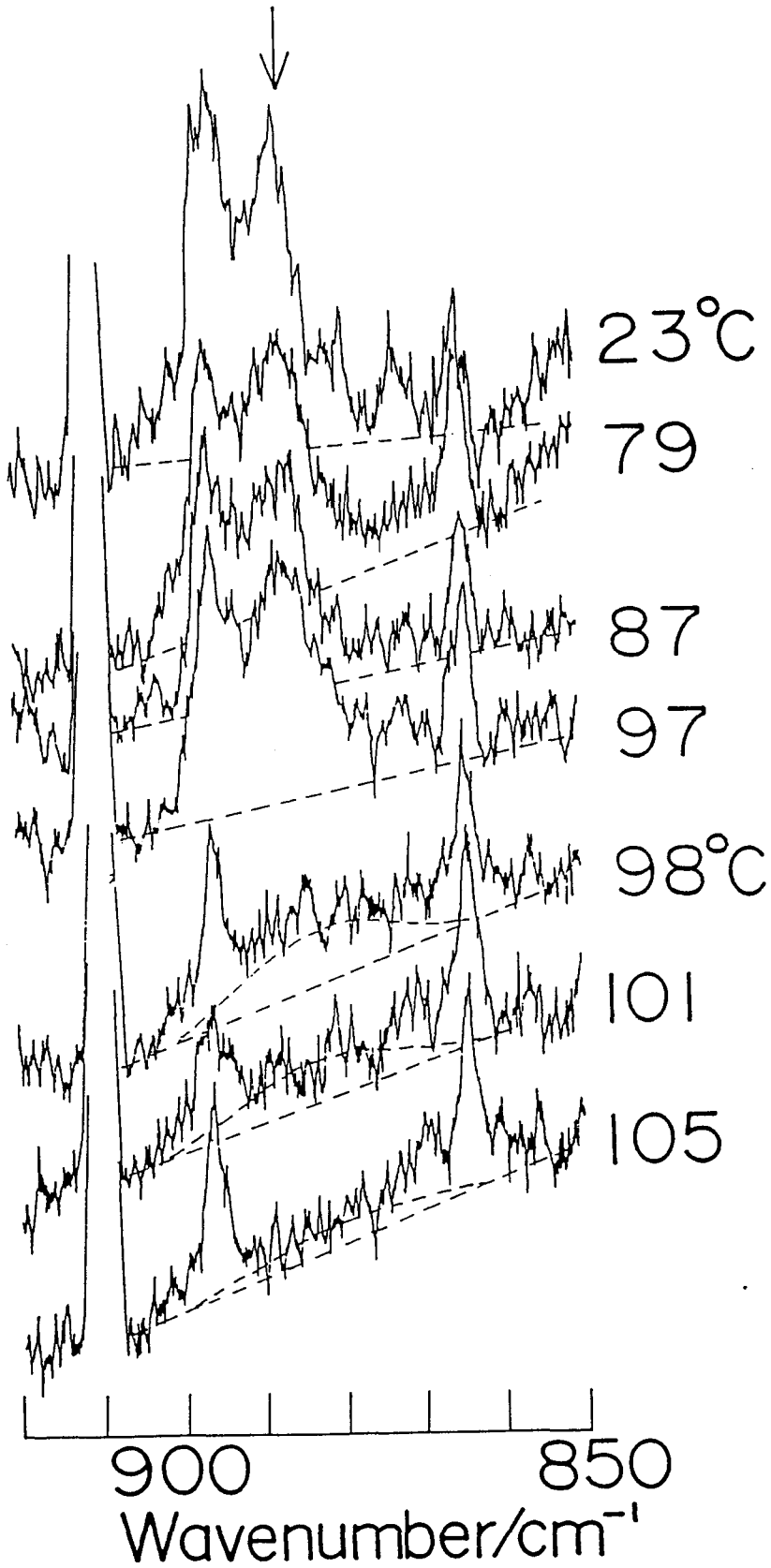

Fig.4-11. band-widths of $\nu(NC_4)$ E mode at various temperatures.

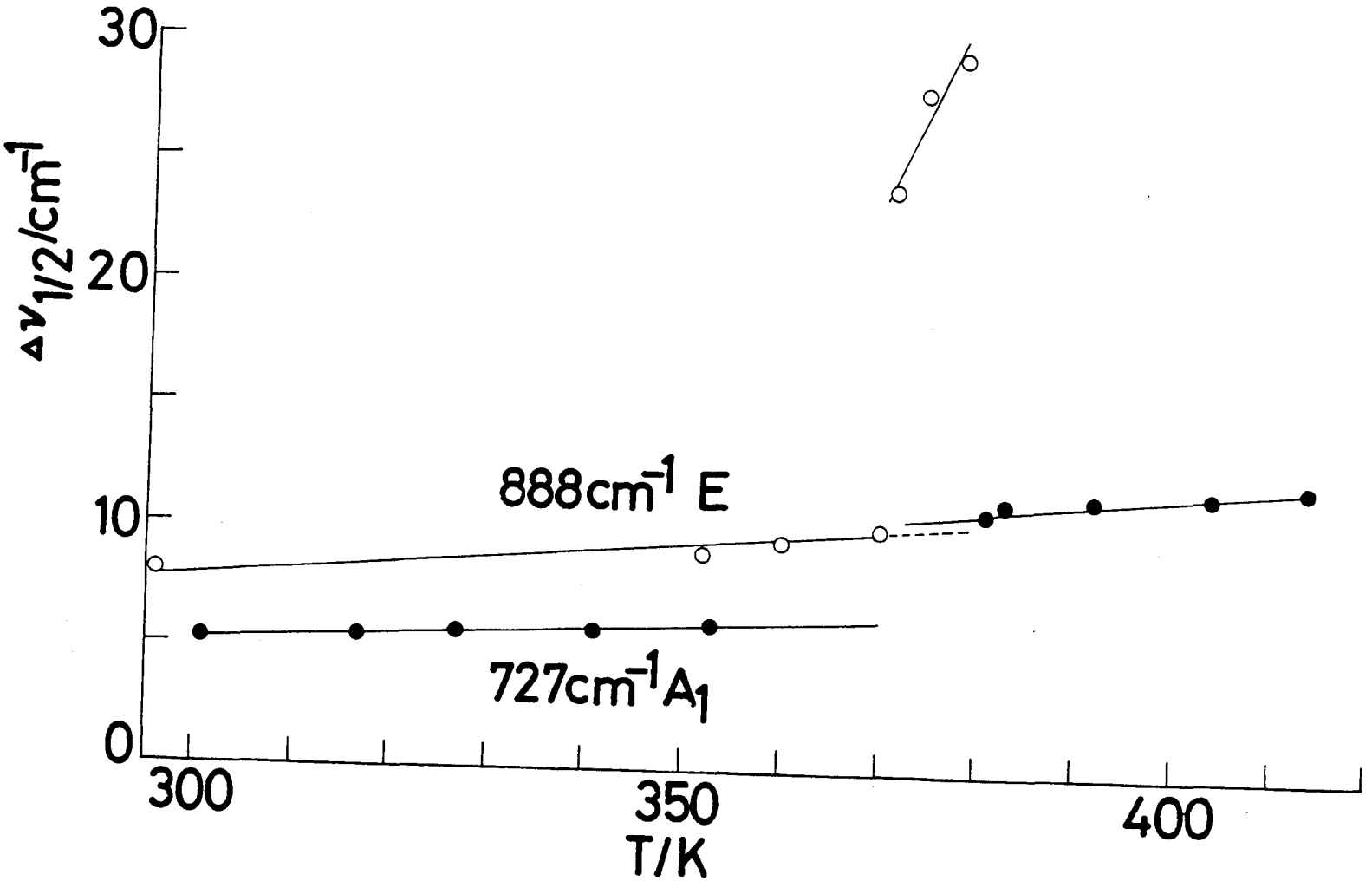

Fig.4-12. Temperature dependence of the full-half-widths of the 888cm^{-1} E mode and the 727cm^{-1} A_1 mode. Broken line extrapolated from the solid line of the E mode of the low temperature phase is subtracted from the solid line of the same mode of the high temperature phase.

rotational reorientational motion of the n-alkane molecule in a channel of the urea crystal.[20] By the same way, the broadening of the Raman bands of the C_n-DABCO-C_{n-2}-X above the transition point was investigated. At atmospheric pressure, 1,4-diazabicyclo(2,2,2)octane (DABCO) undergoes a sloid-solid phase transition at 79.8 °C and melts at 161.1 °C.[21] The low temperature phase is stable below 79.8 °C and the high temperature phase between 79.8 and 161.1 °C. The crystal structure of DABCO in the low temperature phase belongs to the space group C_{6h}^{3}-$P6_{3}/m$. The DABCO molecule having the D_{3h} symmetry is located in a threefold symmetric potential field in the crystal and may execute a 3- or 6-fold reorientational motion around the C_3 molecular symmetry axis and, in addition, reorient around the C_2 molecular symmetry axis as in the case of bicyclo(2,2,2)octane.[22] As an approximation, the situation is assumed to be the case in the high-temperature phase of C_{18}-DABCO-C_{18}-Br_2, although the molecular symmetry of the C_{18}-DABCO-C_{18}-Br_2 is lowered to C_{2v} and the reorientational motion around the C_2 symmetry axis of the bicycloring group may be prohibited by the presence of two long alkyl chains. The molecular motion of the bicycloring of C_n-DABCO-C_{n-2}-Br is approximated by the hopping between two of the three sites 1, 2, and 3 separated by a potential field (Fig.4-13) around the N-N axis of the ring. The N-N axis is assumed to coincide with the threefold axis of the potential field.

According to the result derived by Cho et al.,[20] the profile of a spectral band of a molecule under a reorientational motion is represented, in general, by one Lorentzian function, or

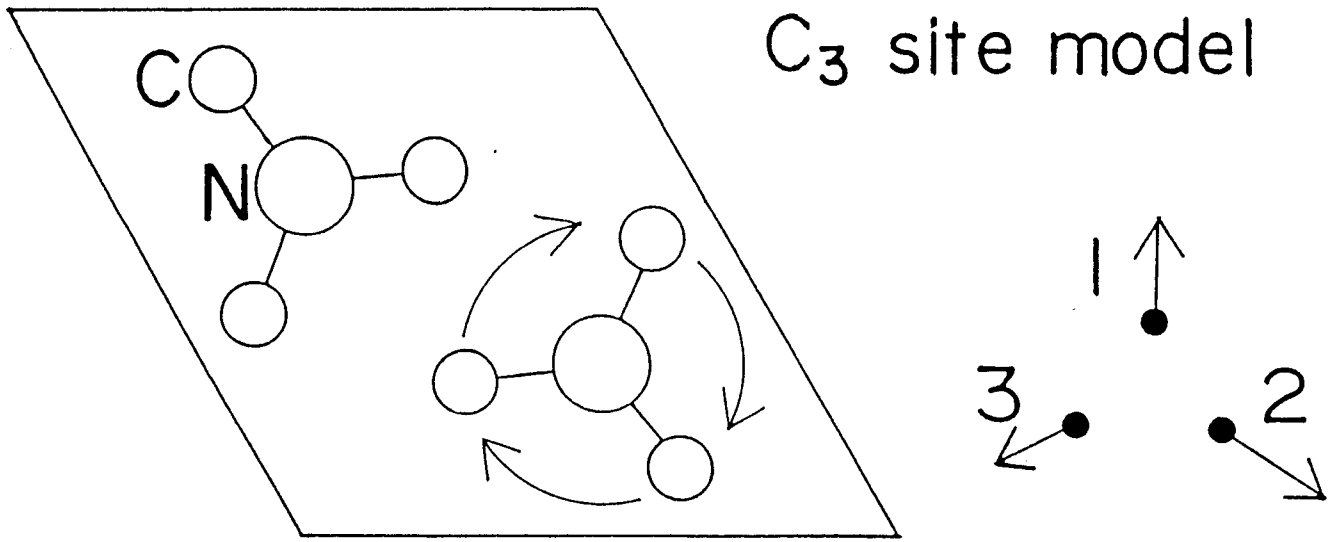

Fig.4-13. Site model.

superposition of certain number of Lorentzian functions which are centered at the same frequency and have different half-width. For the case that is represented by single Lorentzian function, the full-half-width is given by

$$\Delta\nu_{1/2} = \frac{1}{2\pi c}\left[a_K A \exp(-E^*/RT) + r_v\right] \qquad (4\text{-}1)$$

where c is the velocity of light, T the absolute temperature, R the gas constant, and r_v the band width due to both the instrumental resolution and to the relaxation of the vibrational excitation. a_K takes an positive integral value (including zero) depending on the symmetry species of the mode as well as on the polarization measured. E^* depends the activation energy of the reorientational motion of the molecule, and A is the term related to the activation entropy. In the high temperature phase of C -DABCO-C -X , the potential field around the C axis of the bicycloring was supposed to have a C symmetry as described above. In this case, the eigenvalues (exp(-a Kt)) of the matrix of the conditional occupation probability for A and E species are given as 1 and exp(-3Kt) where K is the transition probability of the bicycloring from a site to another site and t is time and therefore the Raman bands of the A and E species consist of one Lorentzian term having $a_K = 0$ (for A) and $a_K = 3$ (for E), respectively (Table IV-I). Thus, the band width of the A mode should be independent on temperature, whereas that of the E mode increases with increase of temperature. In the latter case, the value of E^* is estimated from the slope of the linear plot of ln $\Delta\nu_{1/2}$ vs. 1/T (Fig.4-14):

Table IV-I. Correlation table between D_{3h} and C_3 groups. α_{ij} is the (ij) component of the polarizability tensor where i, j = x, y, z are the Cartesian coordinate fixed on the molecule and α_{IJ} where I, J = X, Y, Z are the space-fixed Cartesian coordinate.[20]

D_{3h} (molecule)	C_3 (site)	C_3(site model)	$\exp(-a_K Kt)$
$\alpha_{xx} + \alpha_{yy}$, α_{zz}	A_1'	A	A $\alpha_{XX} + \alpha_{YY}$, α_{ZZ}	1
	A_2'			
$(\alpha_{xx} - \alpha_{yy}, \alpha_{xy})$	E'	E	E($\alpha_{XX} - \alpha_{YY}$, α_{XY})	exp(-3Kt)
	A_1''		(α_{YZ}, α_{ZX})	
	A_2''			
$(\alpha_{yz}, \alpha_{zx})$	E''			

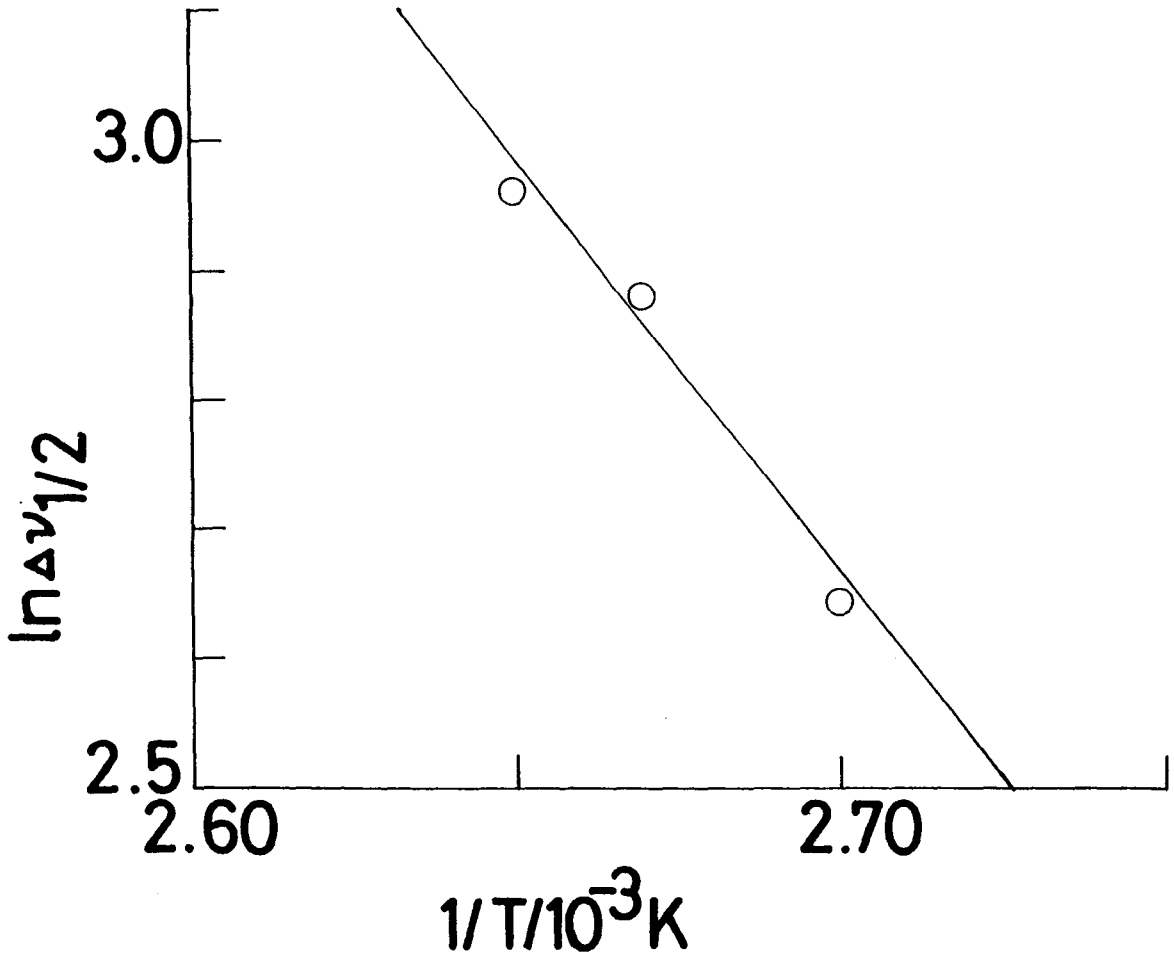

Fig.4-14. $\ln \Delta\nu_{1/2}$ vs. 1/T.

$$\ln \Delta \nu_{1/2} = (-E^*/R)/T + \ln a_K A/2\pi c \qquad (4\text{-}2)$$

With the data of the 888cm^{-1} band, the value of E^* was obtained as 51.8kJmol^{-1}. Here, the contribution of the Γ_v to the bandwidth in the high temperature phase was eliminated by subtracting the width extrapolated from the low-temperature side as shown in Fig.4-12. This value is about three times larger than that (17.1±1.2kJmol^{-1}) of bicyclo(2,2,2)octane in the low temperature phase evaluated from proton n.m.r. spin-lattice relaxation time T_1[22]. The large E^* value of C_{18}-DABCO-C_{18}-Br_2 might be due to the steric hindrance of the rotational motion of the bicycloring group caused by the presence of the Br^- anions. The onset of rotational motion of the ionized bicycloring in the high-temperature phase may be related to the mechanism of ionic conduction.

4-3-3. Transition of C_{17}-DABCO-Br and C_{22}-DABCO-Br

Temperature dependences of the Raman spectra were investigated for C_{17}-DABCO-Br and C_{22}-DABCO-Br. Since similar changes in the Raman spectra were obtained for these compounds, only the spectra of the former are shown in Fig.4-15. The most conspicuous spectral changes at T_o (= 65 °C) is the disappearance of the 1415cm^{-1} band above T_{c1}. This band is associated with the A_g split component of the $\delta(CH_2)$ mode, [14,23,24] and is characteristic of the $O_\perp$ type subcell. Therefore, disappearance of this band means that at T_{c1} the subcell structure changes to another type. This is consistent with the change observed in

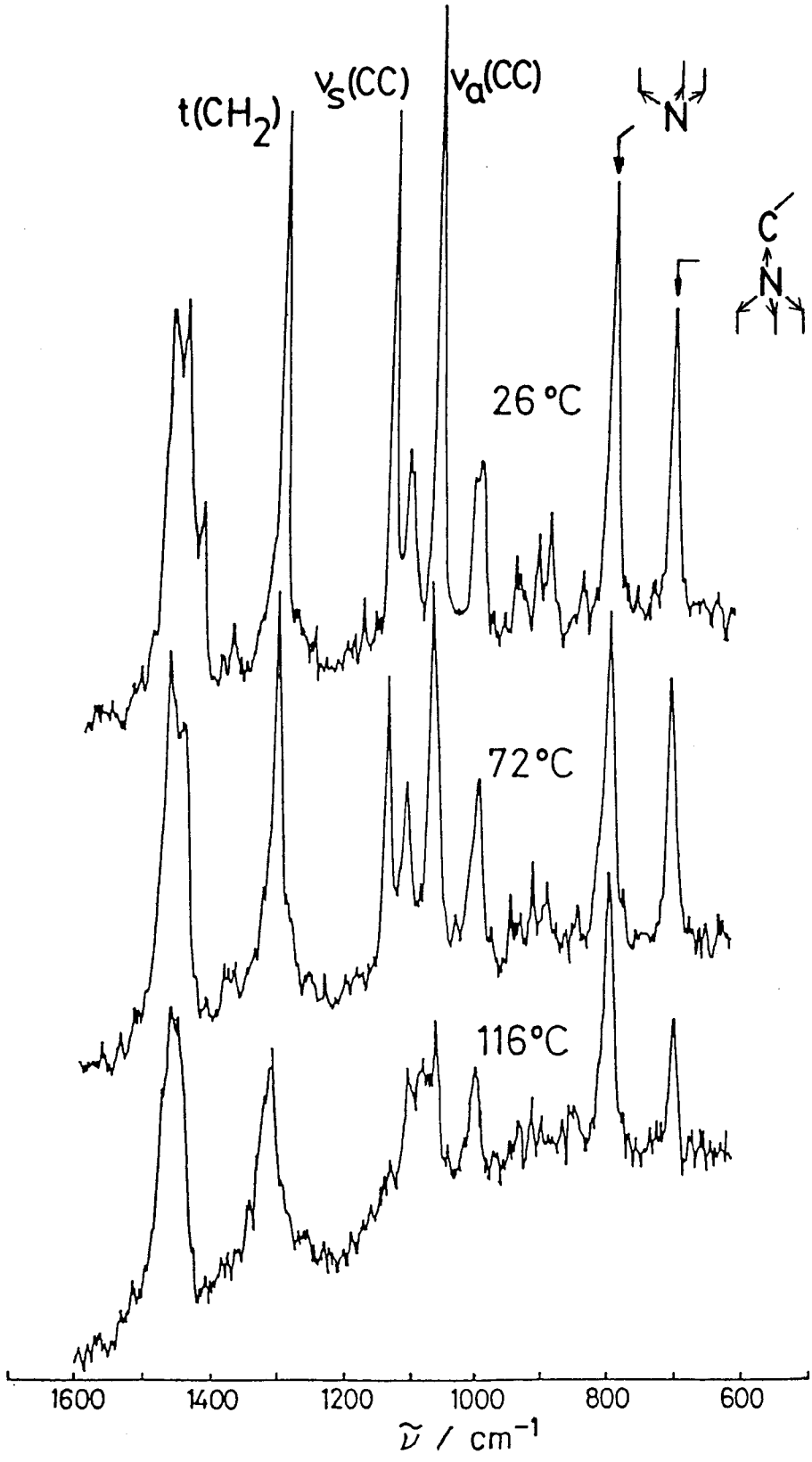

Fig.4-15. Temperature dependence of Raman spectra of C_{17}-DABCO-Br: T_{c1} = 65°C and T_{c2} = 99°C.

the IR spectrum, i.e., the split pairs due to the δ(CH$_2$) at 1476 and 1463cm^{-1} and the CH$_2$ rocking r(CH$_2$) modes at 731 and 720cm^{-1} change to the singlet in the temperature range $T_{c1} < T < T_{c2}$ (= 99 ^{o}C).

As for the subcell structure in the range $T_{c1} < T < T_{c2}$, there are two possibilities, judging from the infrared and Raman spectra. One is the $T_{//}$ type and another is the hexagonal type with rotational disordered orientation of the zigzag planes. When the spectra are measured on powder samples, like in the present case, these two subcell give rise to quite similar spectra and are hardly distinguished from each other. Judging from the large enthalpy change (30kJmol^{-1}) at T_{c1}, the hexagonal packing may be more plausible. The enthalpy changes of n-paraffins C_nH_{2n+2} of n = 17 and 23 from the orthorhombic to the hexagonal phase are 11 and 22kJmol^{-1}, respectively.[25,26]

The strong Raman bands at 1295cm^{-1} (t(CH$_2$) mode), 1131cm^{-1} ν_s(CC) mode, and 1062cm^{-1} ν_a(CC) mode, which appear in the lowest-temperature phase below T_{c1}, are characteristic of the all-trans conformation of the alkyl chain. They decrease in intensity as the amount of conformational defects accomodated in the chain increase, and smear into very broad bands when the chain takes a disordered form like in the liquid alkanes. In the temperature range $T_{c1} < T < T_{c2}$, although these bands still exist with strong intensity and with narrow band-width, the intensities decrease with increasing temperature. This indicates that in this phase a partial conformational disordering takes place in the alkyl chan. Above T_{c2}, all of these conformational-sensitive Raman bands change to those of the

liquid alkanes, indicating that alkyl chain is assumed to take a liquid-like disordered form in the highest-temperature phase.

There are sharp Raman bands at 793 and 704cm^{-1} in the series of the compounds, the position being independent of the alkyl-chain length. They are associated with the C-C and C-N stretching modes of the bicycloring.[11,12] Before and after the T_{c1} transition, these bands show no changes both in intensity and in band-width. Above T_{c2}, the 704cm^{-1} band apparently decreases in intensity. In the case of C_{18}-DABCO-C_{18}-Br$_2$, a strong Raman band (due to totally symmetric ν_4(NC) stretch mode) appears at 727cm^{-1} and this band is broadened above the transition point, suggesting onset of a rotational motion of the bicycloring in the high-temperature phase. The spectral feature of the mono-substituted compounds is somewhat different from that of the di-substituted compounds. Intensity depression of one of the ring bands indicates occurrence of some disordering, either statistically or dynamically, in the ionized bicycloring above T_{c2}, and it may be related to the increase in the ionic conductivity. The difference of the spectral feature ascribed to the chain end-groups between the mono- and di-substituted compounds may caused by the difference of the crystal structure around the end-groups between the two compounds.

4-4. Conclusion

In the highest temperature phase of a series of C_n-DABCO-C_n-X$_2$ and C_n-DABCO-X, the alkylchains have liquid-like irregular conformation although the samples are in solid state. It is certain that the ionic groups bound by electrostatic forces play

an important role in keeping the highest temperature phase crystalline. In the lower temperature phases, the presence of ionic groups keeps the alkyl chains in all-trans conformation at temperature far above the melting point of the corresponding n-alkane. As shown in chapter 1 the presence of ionic groups stabilizes the trans form of polymethylene chains in non-crystalline region in the polyethylene-based ionomers. In conclusion, the presence of ionic groups in ionic long-chain compounds stabilizes trans-conformation of the methylene sequences both in crystalline and non-crystalline phases.

4-5. References

1) J. Shimizu, T. Nogami, and H. Mikawa, Solid State Commun., 54, 1009 (1985).

2) J. Shimizu, T. Nogami, and H. Mikawa, Bull. Chem. Soc. Jpn., 59, 1443 (1986).

3) K. Imamura, J. Shimizu, and T. nogami, Bull. Chem. Soc. Jpn., 59, 2699 (1986).

4) J. Shimizu, K. Imamura, T. Nogami, and H. Mikawa, Bull. Chem. Soc. Jpn., 59, 3367 (1986).

5) K. Imamura, T. Nogami, and Y. Shirota, Bull. Chem. Soc. Jpn., 60, 111 (1987).

6) G. R. Strobl and W. Hagedorn, J. Polym. Sci., Polym. Phys. Ed. 16, 1181 (1978).

7) D. J. Cartler, M. Glotin, P. J. Hendra, H. Jobic, K. H. Moritz M. E. A. Cudby, and H. A. Willis, J. Polym. Sci., Polym. Phys. Ed., 17, 907 (1979).

8) M. Glotin and L. Madelkern, J. Colloid Polym. Sci., 260, 182 (1982).

9) M. Kobayashi, J. Mol. Struct., 126, 193 (1985).

10) Y. Cho, Doctral Thesis, Osaka University (1987).

11) P. Brüesch, Spectrochim. Acta, 22, 867 (1965).

12) P. Brüesch and H. H. Günthard, Spectrochim. Acta, 22, 877 (1965).

13) K. Larsson, Nature, 213, 383 (1967).

14) F. J. Boerio and J. L. Koenig, J. Chem. Phys., 52, 3425 (1970)

15) W. Piesczek, G. R. Strobl, and K. Malzahn, Acta Crystallogr., B30, 1278 (1974)

16) J. D. Barnes and B. Fanconi, J. Chem. Phys., 56, 5190 (1972).

17) G. Zerbi, R. Margil, M. Gussoni, K. H. Morita, A. Biggoto, and S. Dirkov, J. Chem. Phys., 75, 3175 (1981).

18) M. J. Janiak, D. M. Small, and G. G. Shipley, Biochemistry, 15, 4575 (1976).

19) Y. Cho, M. Kobayahsi, and H. Tadokoro, J. Chem. Phys., 84, 4636 (1986).

20) Y. Cho, M. Kobayashi, and H. Tadokoro, J. Chem. Phys., 84, 4643 (1986).

21) T. Wada, E. Kishida, Y. Tomiie, H. Suga, S. Seki, and I. Nitta, Bull. Chem. Soc. Jpn., 33, 1317 (1960).

22) S. McGuigan, J. H. Strange, J. M. Chezeau, and M. Nasr, J. Phys. C: Solid State Phys., 46, 271 (1985).

23) V. B. Carter, J. Mol. Spectrosc., 34, 356 (1970).

24) M. Kobayashi, H. Tadokoro, and R. S. Stein, J. Chem. Phys., 73, 3635 (1980).

25) M. G. Broadhurst, J. Res. Nat. Bur. Stand. Sec. A66, 241 (1962).

26) J. F. Messerly, G. B. Guthrie, S. S. Todd, and H. L. Finke, J. Chem. Eng. Data, 12, 338 (1967).

Chapter 5

Application of Raman Microprobe as a New Technique for Polarization Measurement of Microdomain Structures

5-1. Introuduction

Systems of high polymers as well as long-chain compounds like lipids have attracted great deal of attention as industrial materails exhibiting various functional activities. In most cases, these high-molecular-weight compounds construct heterogeneous domain structures of micron or submicron size. Formation of such higher-order structures is closely related to the specific physical and chemical properties of the bulk materials, so that elucidation of the molecular-level structure of the individual domain of essential importance as the basis of molecular design of these materials. Thus, development of the microcharacterization techniques in the field of molecular spectroscopy is increasing its importance.

The Raman microprobe technique is very powerfull for the investigation of the molecular-level structures of micron-sized samples, and have been used for various systems including high polymers. However, in order to extend the utility of this method there are fundamental problems to be solved. Of these we are concerned in this chapter with the following three problems from the experimental view point. The first one is the spatial resolution in both the axial and horizontal directions. The theoretical consideration has been made by Turrell[1] based on the equations derived by Wolf et al.[2,3] that express the electromagnetic field strength of a focused coherent laser beam. The result gives the limit of the spatial resolution in the Raman microprobe technique. In actual experiment, there will be other factors that lower the resolution. The effective spatial resolution in the axial direction will be derived from the observed depth profile of micropolytype structure in the growth steps on the surface of a single crystal of stearic acid.

Second, we are concerned with the polarization scrambling caused

by a sharp focusing with a high magnification objective. Polarization data of Raman spectra of single crystals give us valuable information about the symmetry species of the bands as well as the molecular and crystal orientations. In the ordinary Raman experiment the effect of the polarization leakage due to the non-parallel incident of the laser beam and collection of the scattered light within a definite solid angle produces not so serious problem. On the contrary, in the case of the microfocus Raman experiment, the scrambling effect is so remarkable that it may lead us to a misunderstanding of the obtained spectral data.[4] Conversely speaking, by utilizing this effect we are able to get structural information along the depth direction. As a typical example, we deal with the micron-sized single crystal of orthorhombic modification of polyoxymethylene. Polarized Raman spectra taken, for the first time, on the single crystal are analyzed by taking this effect into account.

Third, spectral change depending on the position of the focal point in α-quartz single crystal which is caused by the optical rotation of the incident polarization plane is dealt with.

5-2. Experimental

5-2-1. Microprobe Instrument

A JASCO CT 1000D double monochromator (with the focal length of 1m) equipped with an epi-illumination optical microscope (Olympus BH-2) is used. The 514.5nm exiting light (Ar^+ laser) polarized in a particular direction (adjusted by rotating a half-wavelength plate) is focused through an objective at a selected position of the specimen. The depth of the focal point measured from specimen surface is adjusted with a microgauge with precision of 1 μ m. The backward scattered light is collected by the same objective, passes through a beam splitter and a zoom lens Olympus A 70-210mm F4 and is focused on the entrance slit. Before the entrance slit there are an analyzer and a polarization scrambler. An iris diaphragm in the zoom lens acts as a spatial filter controlling the axial-resloving power. The objectives used are OLYPUS Neo Spla x10, x20, x50, and x100, whose optical constants are listed in Table V-I.

5-2-2. Samples

a) Stearic Acid Overgrown Crystals

Experimental spatial resolution was derived from the observed depth profile of micropolytype in the growth steps on the surface of a single crystal of stearic acid B form. Single-crystal specimens of Mon polytype of the stearic acid B form were supplied from Dr. Sato of Hiroshima University. They were lozenge-shaped plate crystals of 50-200μm thickness and several millimeter width with an acute interedge angle of 75° (the characteristic value of the B form). The basal planes of the

Table V-I. The optical constants and spatial resolutions of the objective lenses.

Magnification	N A	θ_m	f	F.L./mm	Resolution $z/\mu m$	Resolution $\bar{x}/\mu m$
x10	0.30	17.5°	1.66	18.0	10.2	0.98
x20	0.46	27.4°	1.09	9.0	4.2	0.65
x50	0.80	53.1°	0.63	3.6	1.2	0.43
x100	0.90	64.2°	0.56	1.8	0.9	0.39

$$N A = \sin\theta_m , \quad f = \frac{1}{2\sin\theta_m}$$

crystals are parallel to the crystallographic (001) plane and the a and b axes are located parallel to the acute and obtuse bisectrices of the lozenge, respectively. Crystals of the C form of staeric acid were obtained from n-hexane solution.

A single-crystal of B(Mon) (the seed crystal) was put in a vessel containing a n-hexane solution nearly saturated with respect to the C crystal. The temperature was controlled within $\pm 0.02^{\circ}C$. After several hours the seed crystal was picked out from the vessel and was subjected to optical microscope observation. Fig.5-1 shows optical micrograph of a basal of a B(Mon) crystal after 9h at $23^{\circ}C$. There are typical growth spiral steps of newly formed crystal of B(Orth II) on the surface which faced the solution. On the photograph the position subjected to microfocus Raman measurement is indicated.

b) o-POM and α -Quartz

The origin of the single crystals of orthorhombic polyoxymethylene is describe in Ref.5. They have a specific shape resembling a "moth" with dimensions as large as 30-50 μm diameter and about 2 μm thickness (Fig.5-2). On the surface, there are observed parallel striations and the sample-based Cartesian coordinates are defined as follows: X is parallel to the striation, Y perpendicular to it within the plane surface, and Z normal to the plate surface. α -quartz crystal used is a synthetic single crystal 1(along the crystallographic z-axis) x 10 x $10mm^3$ and is cut all side accurately normal to the crystallographic axes ($\pm 0.2^{\circ}$).

5-3. Experimental Spatial Resolution

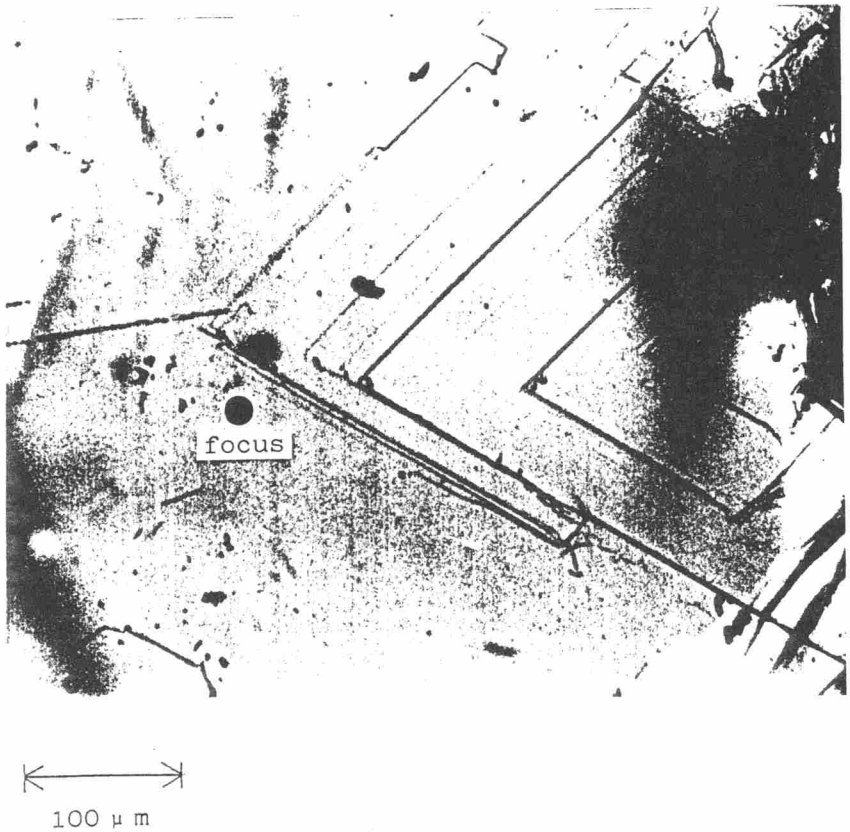

Fig.5-1. Optical micrograph of a basal plane of a B(Mon) seed crystal of the stearic acid B form subjected to an overgrown process in n-hexane solution at 23°C for 9h: growth spiral steps of a newly formed crystal, the position subjected to microfocus Raman measurement being indicated.

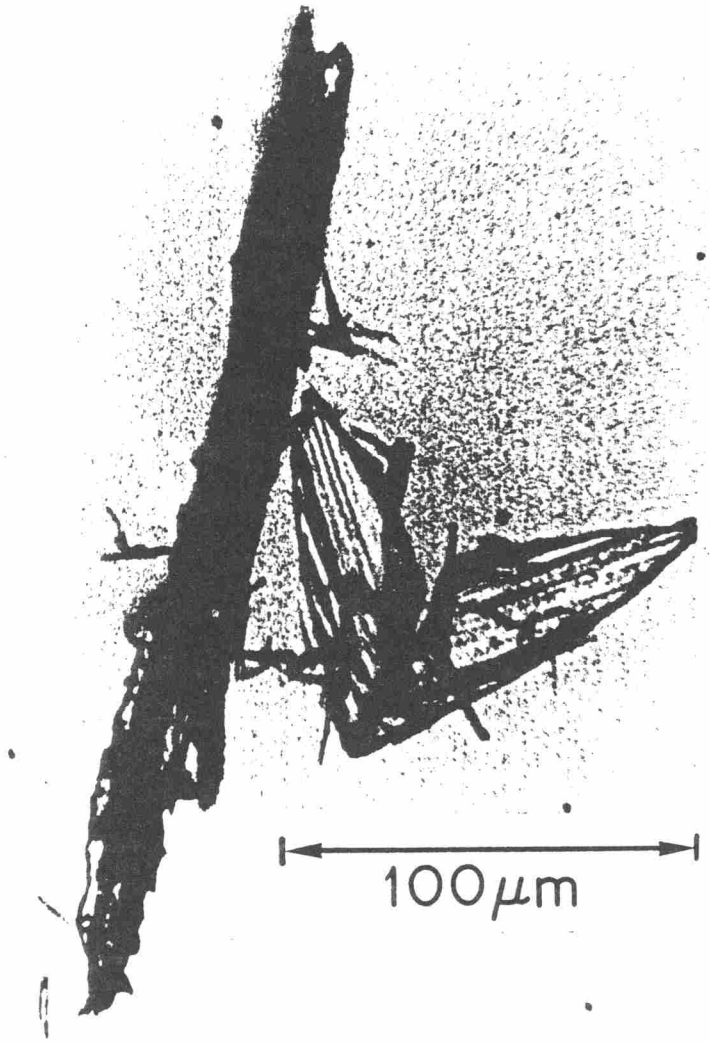

Fig.5-2. Optical micrograph of o-POM single crystal.

In this section, the experimental axial resolution in the Raman microprobe measurement was evaluated from the observed depth profile of micropolytype structure of stearic acid B from. Fig.5-3 reproduces the $c(a\ b)\bar{c}$ spectra taken on a B(Mon) crystal, one basal plane of which is covered with a thin layer overgrown crystal of Orth II, measured by focusing at three different positions: (a) at the surface of the overgrown crystal, (b) near the boundary plane between the seed and the overgrown crystal, and (c) at the surface of the bare seed crystal. Here, the bands at 21.0 and 6.9cm^{-1} are characteristic of Orth II, and those at 23.3 and 10.5cm^{-1} of Mon. The depth profile taken with x100 and F = 32 by Morishita[6] is reproduced in Fig.5-4. As the focal point shifts from the surface of Orth II into interior, the spectrum changes continuously from that typical of Orth II to that typical of Mon. The B(Orth II) band at 21.0cm^{-1} and the B(Mon) band at 23.3cm^{-1} have almost the same scattering power. The fraction of the B(Orth II) component to the total integrated intensity of the overlapping profile, R = I(Orth II)/I(total), was obtained by graphical separation as a function of the depth measured from the step surface. Let us assume that the one-dimensional distribution of the effective scattering intensity from a position apart by x from the focal plane is expressed by an even function f(x). If the boundary plane between the two polytype is located at d apart from the focal plane, R is expressed by the followign equation (see Fig.5-5):

$$R(d) = \int_{-\infty}^{d} f(x)dx \Big/ \int_{-\infty}^{+\infty} f(x)dx = (1/2) + \left(\int_{0}^{d} f(x)dx \Big/ \int_{-\infty}^{+\infty} f(x)dx\right) \qquad (5\text{-}1)$$

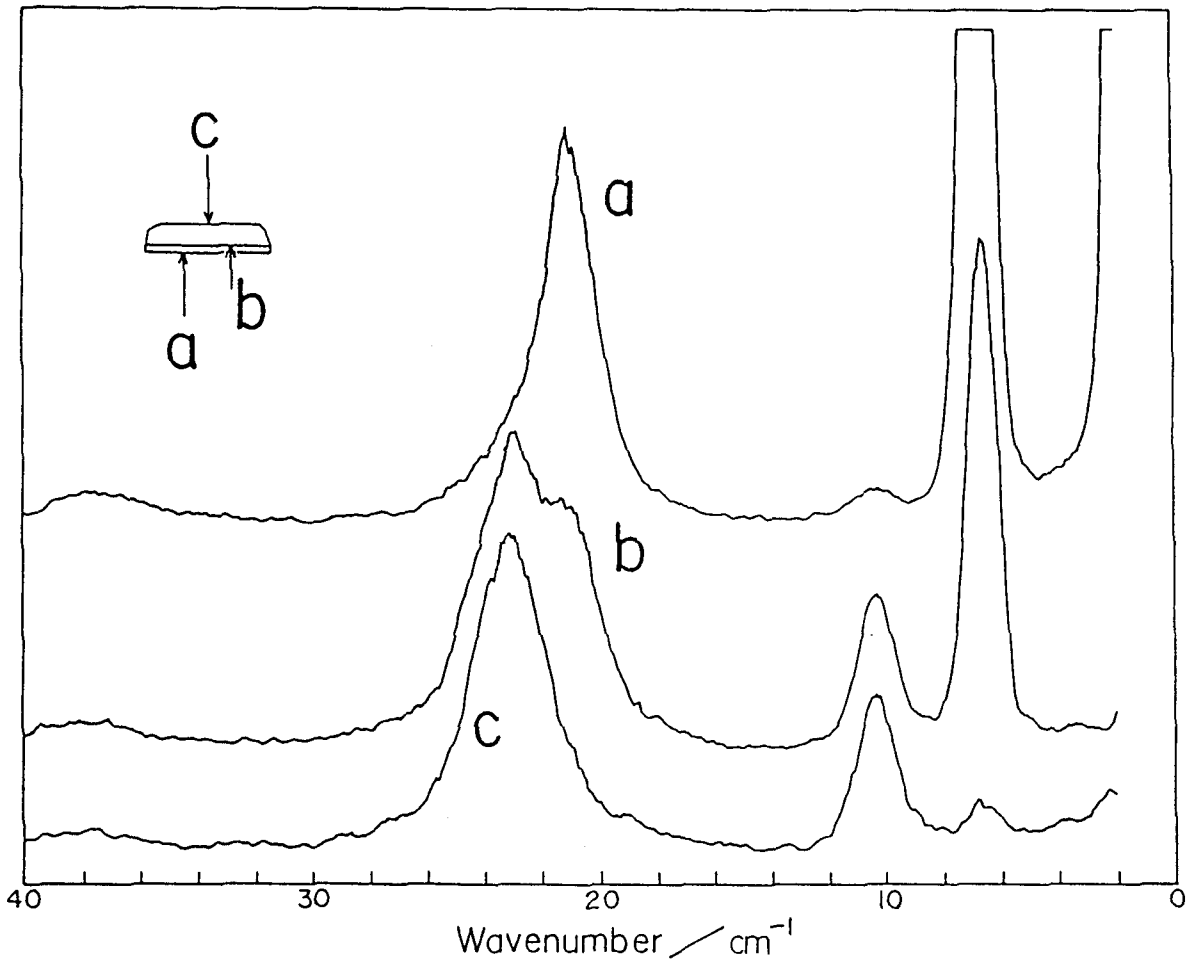

Fig.5-3. The c(a b)$\bar{c}$ component of the microfocus Raman spectra taken on a B(Mon) crystal, one basal plane of which is covered with a thin layer of B(Orth II) crystal, by focussing at three different positions : (a) surface of the overgrown crystal, (b) boundary plane, and (c) surface of the seed crystal.

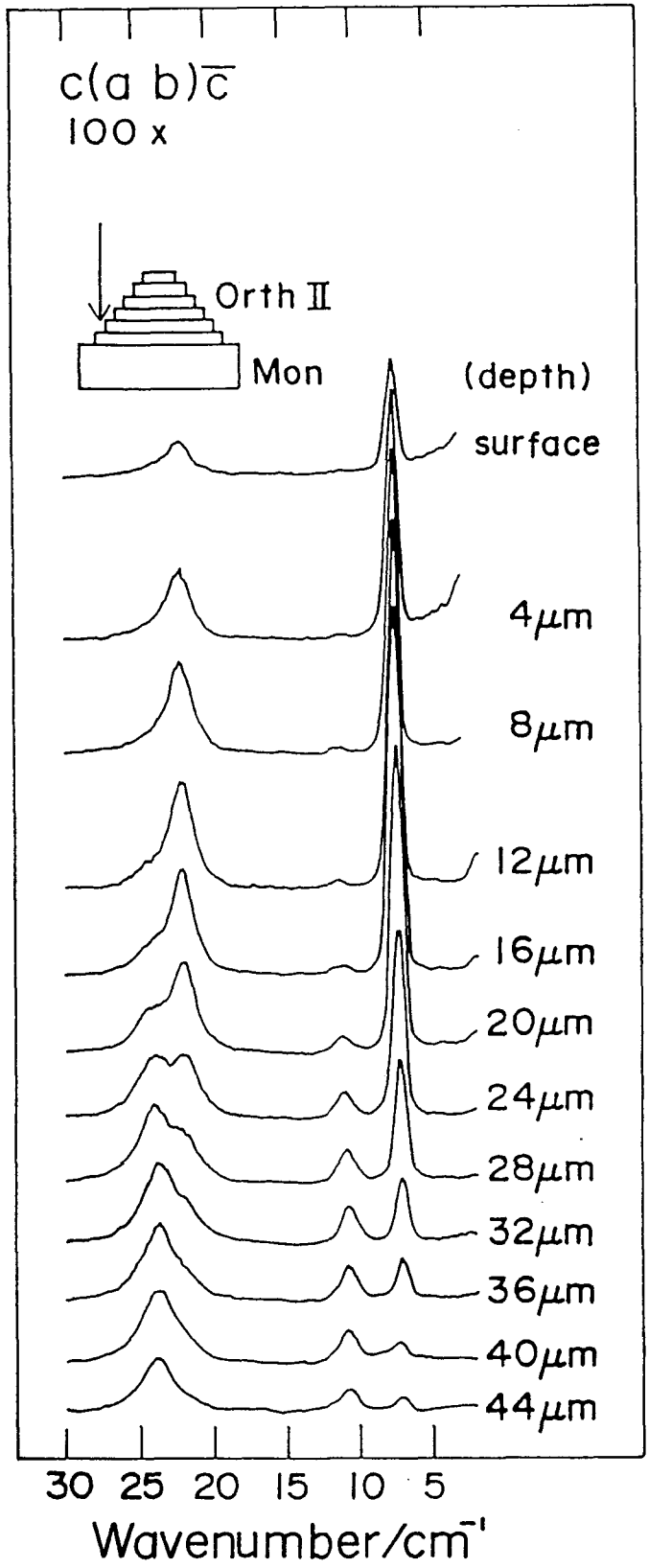

Fig.5-4. Depth profile of the microfocus Raman spectra (x100, F = 32).

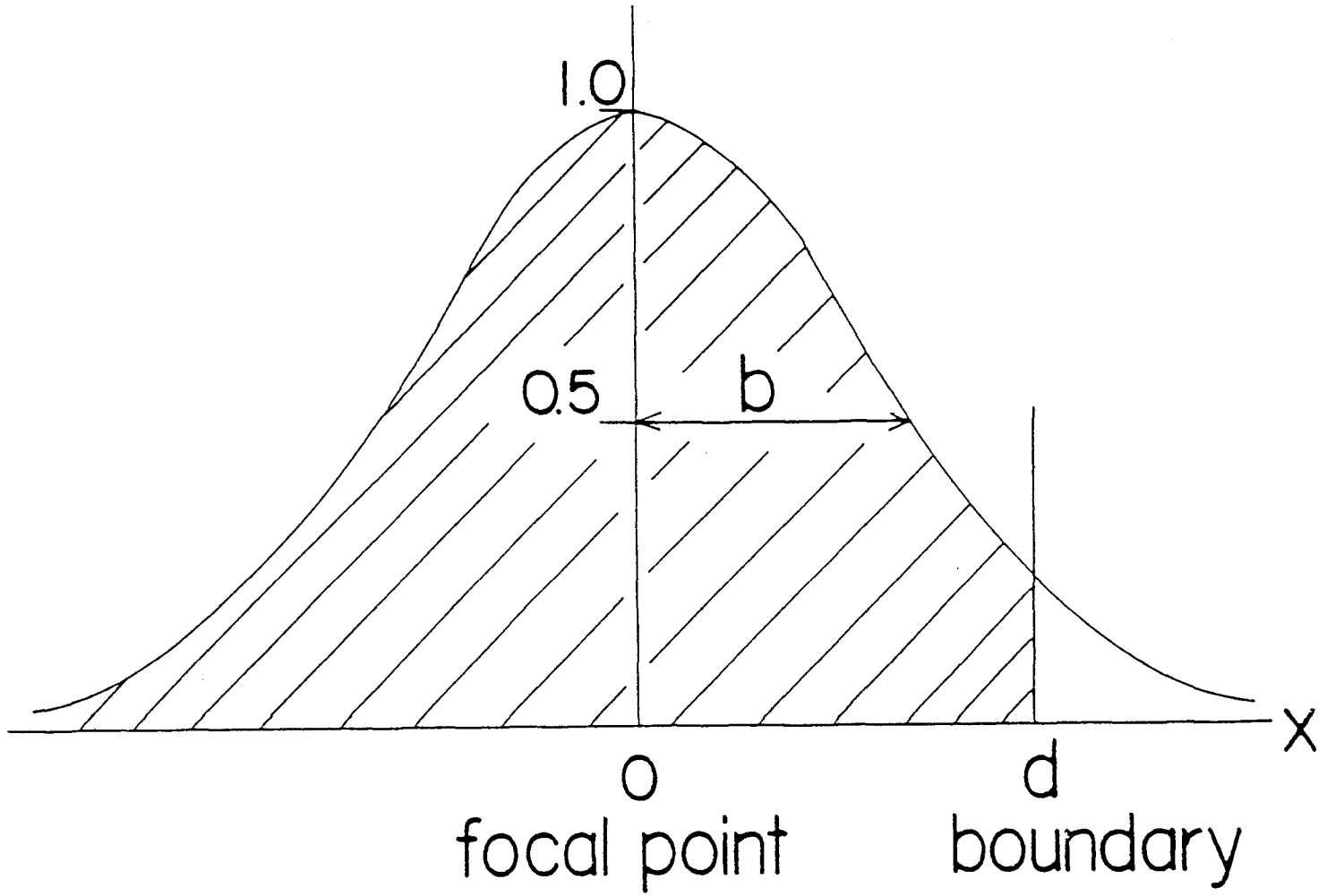

Fig.5-5. One-dimensional distribution function of the effective scattering intnsity.

If f(x) is a Lorentzian function

$$f(x) = a/(b^2 + x^2) \tag{5-2}$$

with the maximum value of a/b^2 and the full-half width of 2b, eq 5-1 is written as

$$R(d) = (1/2) + (1/\pi)\tan^{-1}(d/b) \tag{5-3}$$

the effective spatial resoltuion being 2b. In Fig.5-6, the calculated R(d) curves for various 2b values are compared with the experimental result (open circles), and the experimental spatial resolution is estimated as about 2 μ m.

If a Gaussian function is used

$$f(x) = (1/(2\pi)^{1/2}) \exp(-h^2x^2/2) \tag{5-4}$$

with the maximum value of $1/(2\pi)^{1/2}$ and the full-half-width of $2(2\ln 2)^{1/2}/h$, the R(d) vs. d curves are obtained (by the numerical computation as shown in Fig.5-7. The spatial resolution for the experiment is estimated as 7-10 μ m although the fitting with experimental data is not as good as in Fig.5-6. Thus, the spatial resolution estimated in this may depend on the f(x) assumed.

In order to search for the most plausible distribution function the spatial distribution of the electric energy produced by a coherent laser beam was calculated. The detail will be described in section 5-4. Fig.5-8 shows the distribution along the depth direction. The curve is well reproduced by a Gaussian function (the broken line) except for the ripple at the wing. The theoretical spatial resolution for the x100 objective is

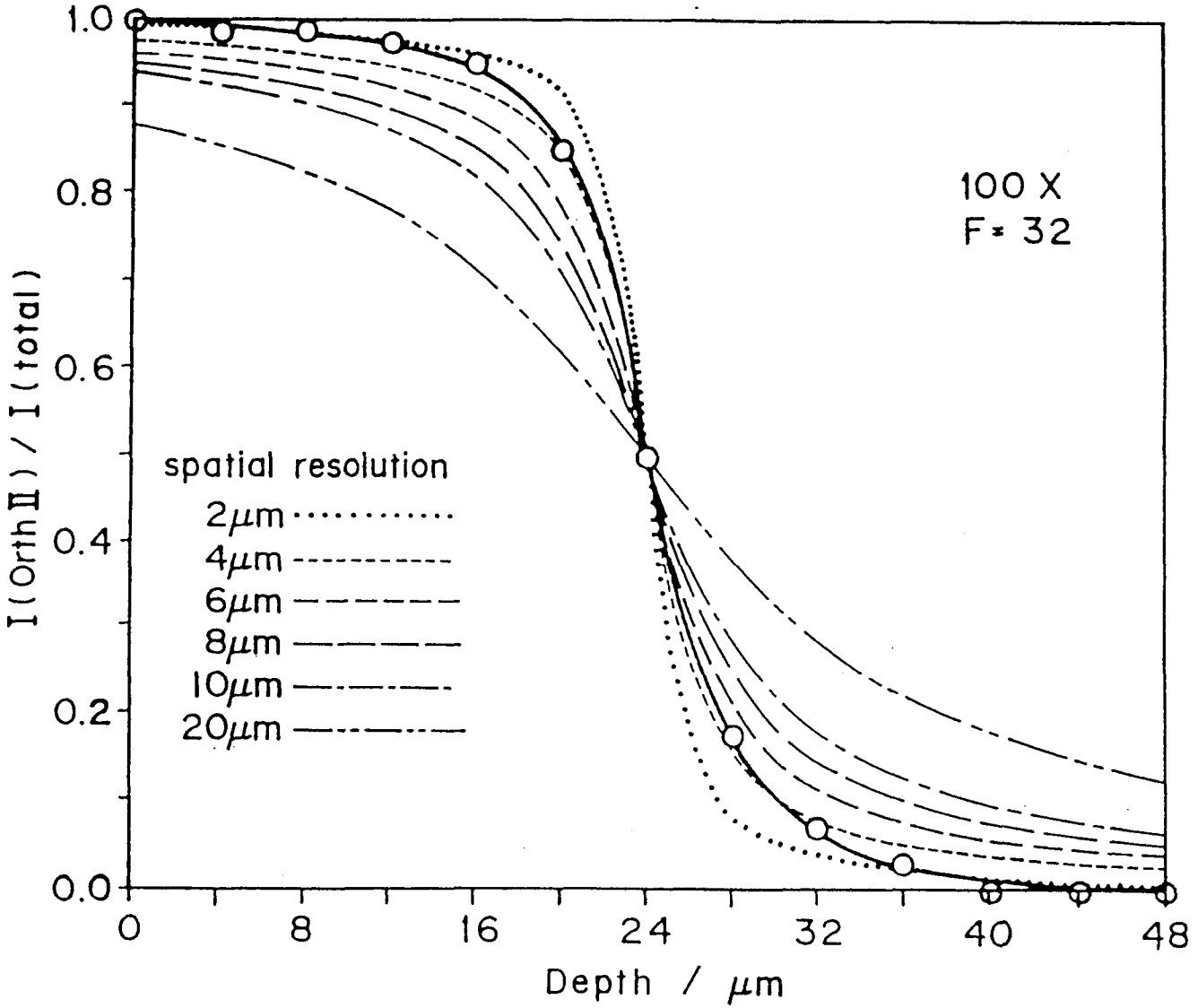

Fig.5-6. R(d) vs. d curves derived from the Lorentzian with various full-half-widths (= 2b) and the experimental data (open circles).

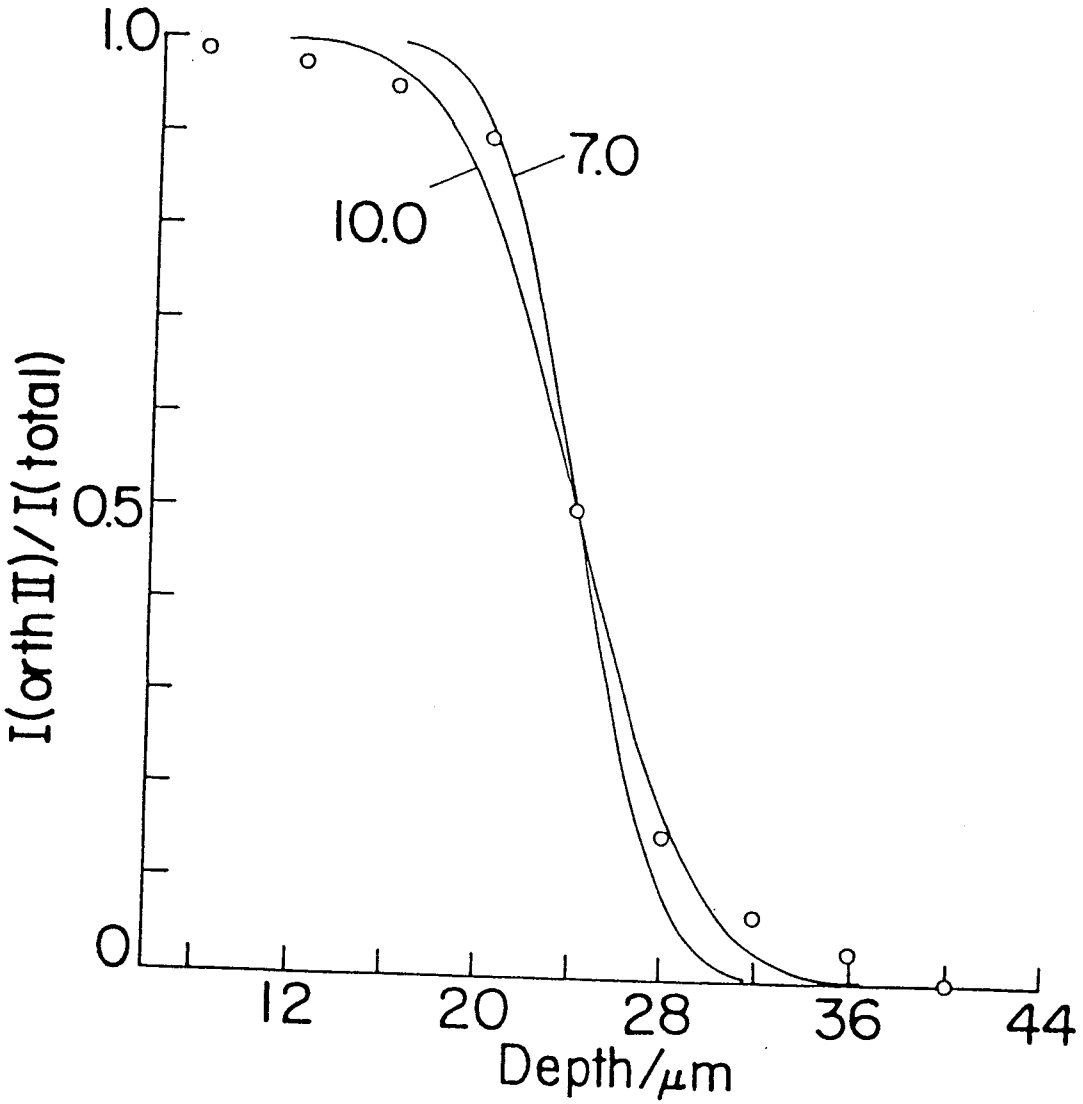

Fig.5-7. R(d) vs. d curves derived from the Gaussian function with two different full-half-widths (7.0 and 10.0μ m) and the experimental data (open circles).

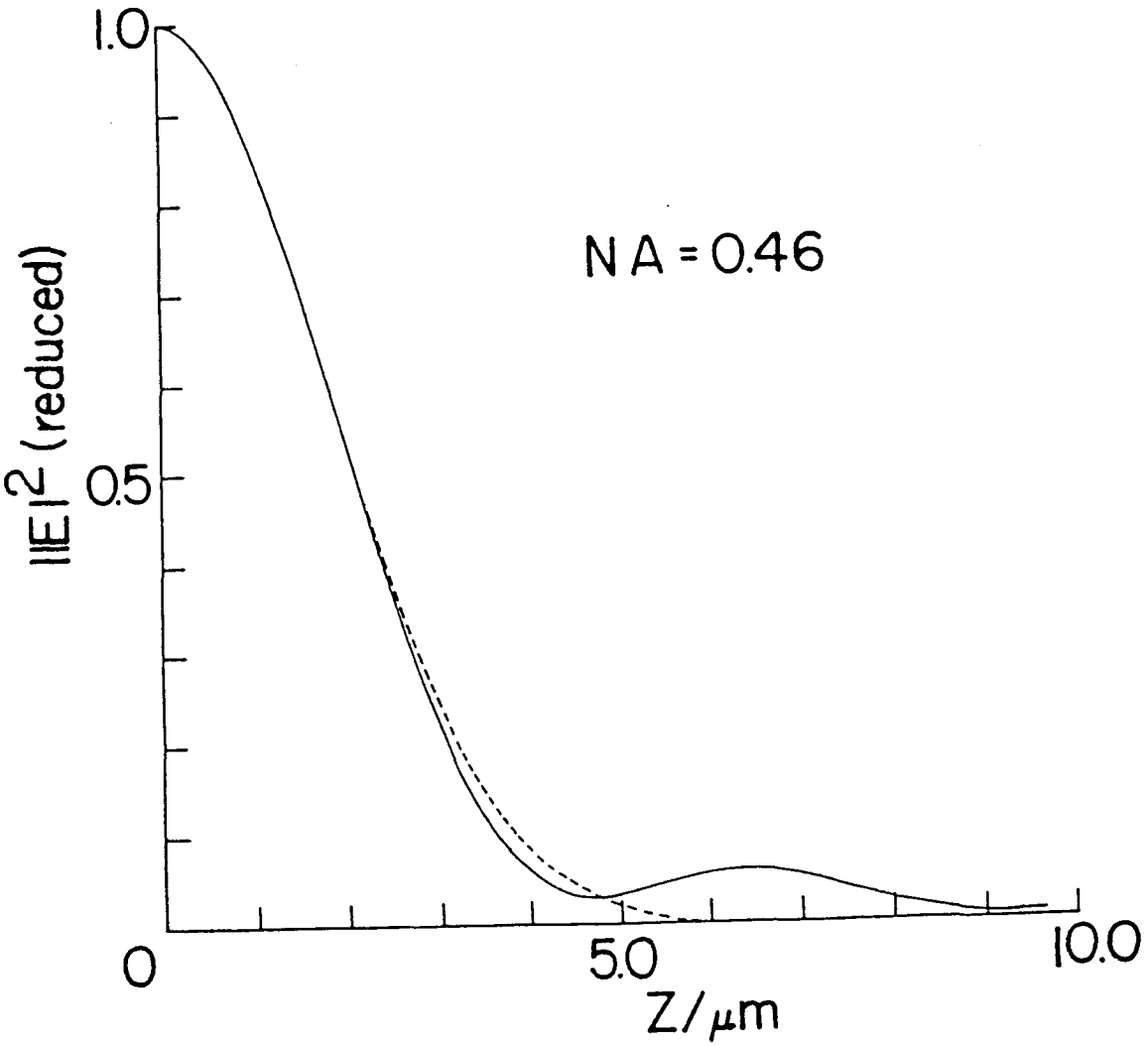

Fig.5-8. Calculated spatial distribution along the depth direction of the electric energy produced by a coherent laser beam. The broken curve represents the best-fit Gaussian function.

estimated (after correction for the refraction) as 2.4μm. This value may correspond to the maximum experimental resolution.

5-4. Calculated Spatial Resolutions

Spatial resolutions in Raman microprobe technique are principally determined by two factors.[7] One is the distribution of electric field of the incident beam near the focus in the specimen. The other is the optical system which collects the scattered light, i.e., the solid angle of the scattering cone and the hole size of the diaphragm inserted into the optical path. In this section the former factor is considered. The effect of refraction at the sample surface is neglected.

Consider a monochromatic incident beam polarized to the X-direction comes from $Z = +\infty$ and is focused at the origin of the Cartesian coordinates (X, Y, Z) as shown in Fig.5-9. The electric field vector at point P specified by polar coordinate (r, θ, ψ) is denoted by $\mathbb{E}_p(r, \theta, \psi)$. The X, Y, Z components of $\mathbb{E}_p$ are given by the formulae derived by Wolf et al. as[2,3,8]

$$E_X = - i (I_0 + I_2 \cos 2\psi) \tag{5-5}$$

$$E_Y = - i I_2 \sin 2\psi \tag{5-6}$$

$$E_Z = -2 I_1 \cos\psi \tag{5-7}$$

where I_0, I_1, I_2 are defined as

$$I_0(u,v) = \int_0^{\theta_m} D(\theta)\sin\theta\,(1+\cos\theta)\,J_0(v\sin\theta/\sin\theta_m) \times \exp(iu\cos\theta/\sin^2\theta_m)\cos^{1/2}\theta\,d\theta \tag{5-8}$$

$$I_1(u,v) = \int_0^{\theta_m} D(\theta)\sin^2\theta J_1(v\sin\theta/\sin\theta_m)$$

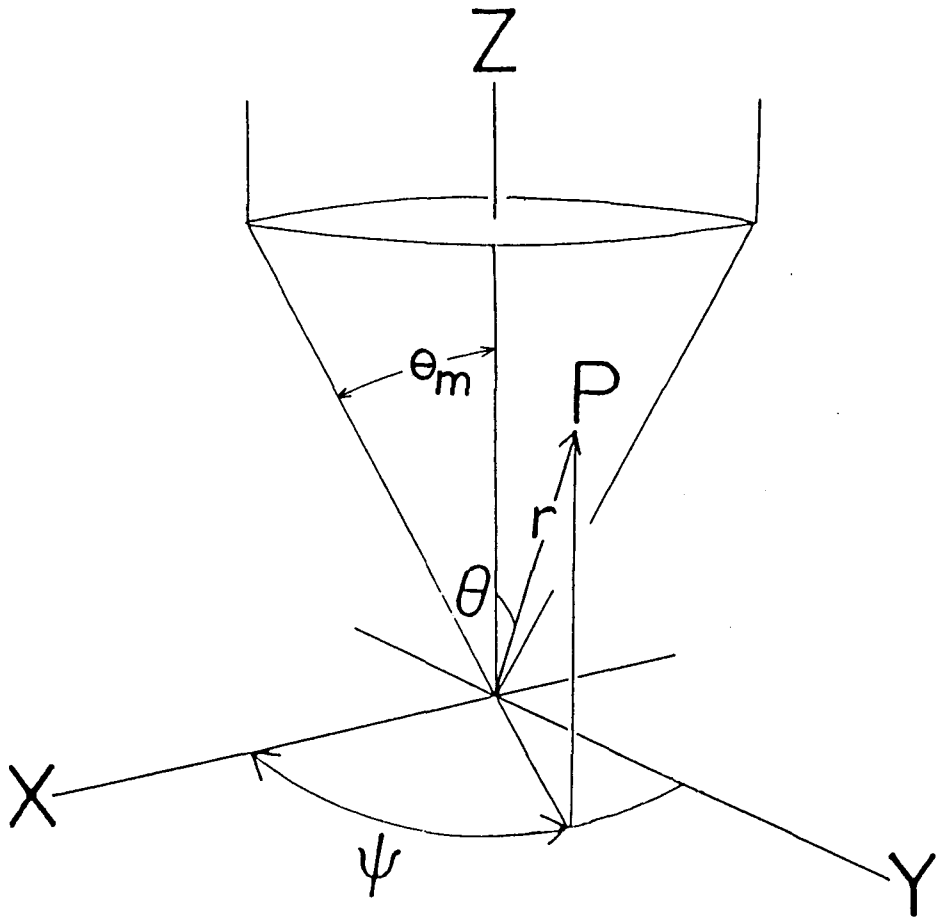

Fig.5-9. Polar coordinates for monochromatic coherent incident electric field near focus.

$$x\exp(iu\cos\theta/\sin^2\theta_m)\cos^{1/2}\theta\, d\theta \qquad (5\text{-}9)$$

$$I_2(u,v) = \int_0^{\theta_m} D(\theta)\sin\theta(1-\cos\theta)J_2(v\sin\theta/\sin\theta_m) \; x\exp(iu\cos\theta/\sin^2\theta_m)\cos^{1/2}\theta\, d\theta \qquad (5\text{-}10)$$

$D(\theta)$ is the radial intensity distribution of Gaussian form given as

$$D(\theta) = N\,\mathrm{cosec}\,\theta_m \exp(-\sin^2\theta/\sin^2\theta_m) \qquad (5\text{-}11)$$

where the factor N, which is a function of the wavelength and intensity of the laser, was adjusted to normalize the total electric energy at the focal point ($u = v = 0$). The $J_n(v\sin\theta/\sin\theta_m)$ are Bessel function of the first kind of order n, u and v the dimensionless optical coordinates given by

$$u = kZ\sin^2\theta_m \qquad (5\text{-}12)$$

and

$$v = k\sqrt{X^2 + Y^2}\sin\theta_m \qquad (5\text{-}13)$$

where $k = 2\pi/\lambda$ (with $\lambda = 514.5$nm) and θ_m the angular semi-aperture ($= \sin^{-1}(1/2f)$) defined as shown in Fig.5-9. Each component of $\mathbb{E}_p$ is specified by u and v. Calculations were carried out by a NEC computer ACOS 1000, at the steps $u = 0.2$ and $v = 0.2$. With a graphical interpolation technique, the distribution of the electric field in the vicinity of the focus was obtained.

5-4-1. Energy Distribution along Z-axis

The time-averaged electric energy distribution along the Z-axis was calculated and the axial resolution was considered. In Fig.5-10, the calculated values of $|\mathbb{E}|^2$ divided by the intensity at

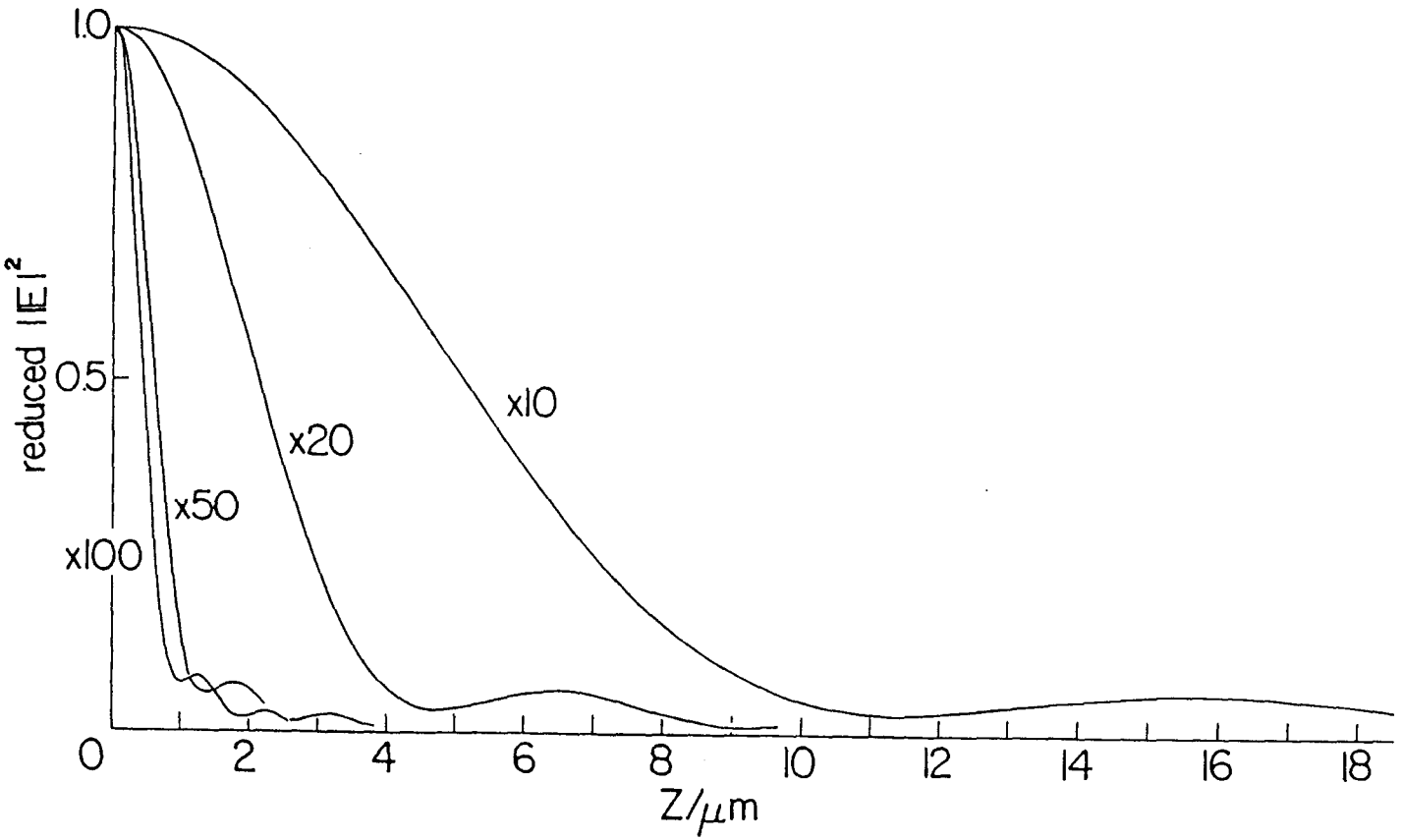

Fig.5-10. Energy distribution along Z-axis.

the focus are drawn against the Z coordinate for various magnifications of the objective. The intensity along the Z-axis decreases monotonously first and followed by small ripple at the tail. This result is essentially the same obtained by Turrell (Fig.3 in ref.1). The full half-widths of $|E|^2$ obtained from the graphs are listed in Table V-I. The objectives of magnification x100 and x50 have the spatial resolutions of 0.9 and 1.2 μm. The resolution for the objective with magnification x20 is 4.2 and that for x10 is 10.2μm.

5-4-2. Energy Distribution within X-Y Plane

Distribution of the electric field on the focal plane was calculated as a function of v and ψ, and plotted against the X and Y coordinates (Figs 5-11 -14). The spatial resolutions obtained from the averaged full half-widths of X and Y directions are listed as $\bar{X}$s in Table V-I. The horizontal resolution spreads from 0.39 to 0.98μm as the magnification decreases from x100 to x10.

5-4-3. Distribution of $|E_X|^2$ and $|E_Z|^2$

For the polarization analysis in the microprobe technique the fraction and distribution of E_Z is important. In this part the distribution of E_Z and E_X are evaluated quantitatively. Fig.5-15 shows the contour maps of the time-averaged E_X and E_Z components of the complex electric field on the focal plane for the case of magnification x10. The values of $|E_X|^2$ and $|E_Z|^2$ are normalized to the $|E_X|^2$ value at the origin. Two maxima of $|E_Z|^2$ (=0.009) are attained at X = ±0.66 and Y = 0μm. Integrated

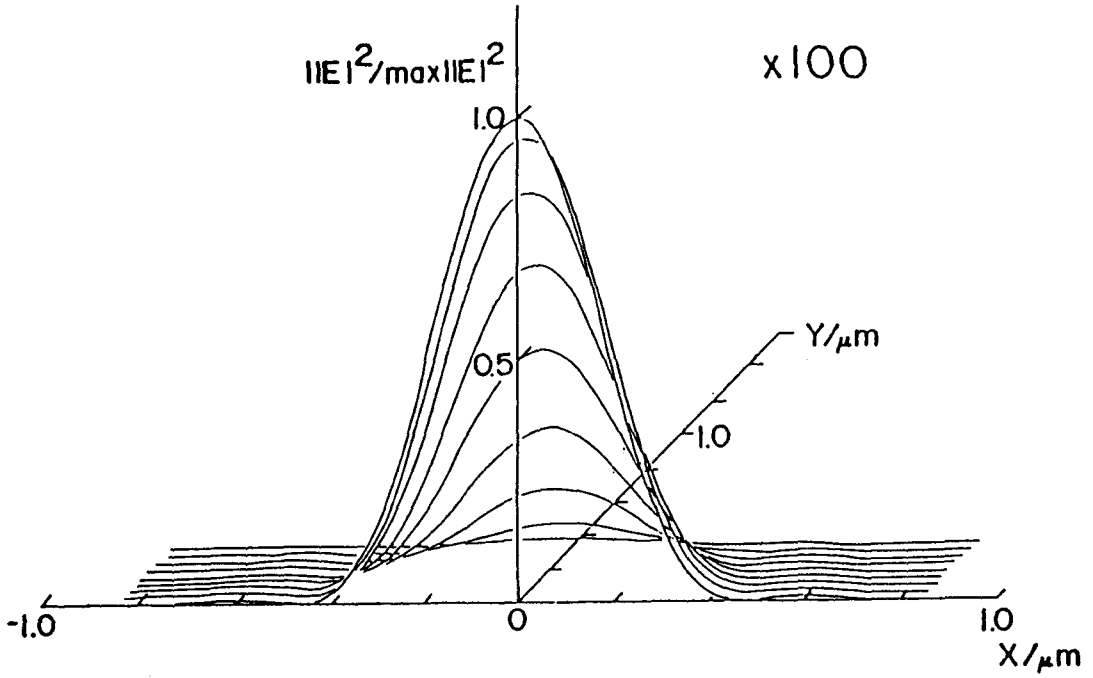

Fig.5-11. Energy distribution within X-Y plane of NA 0.90.

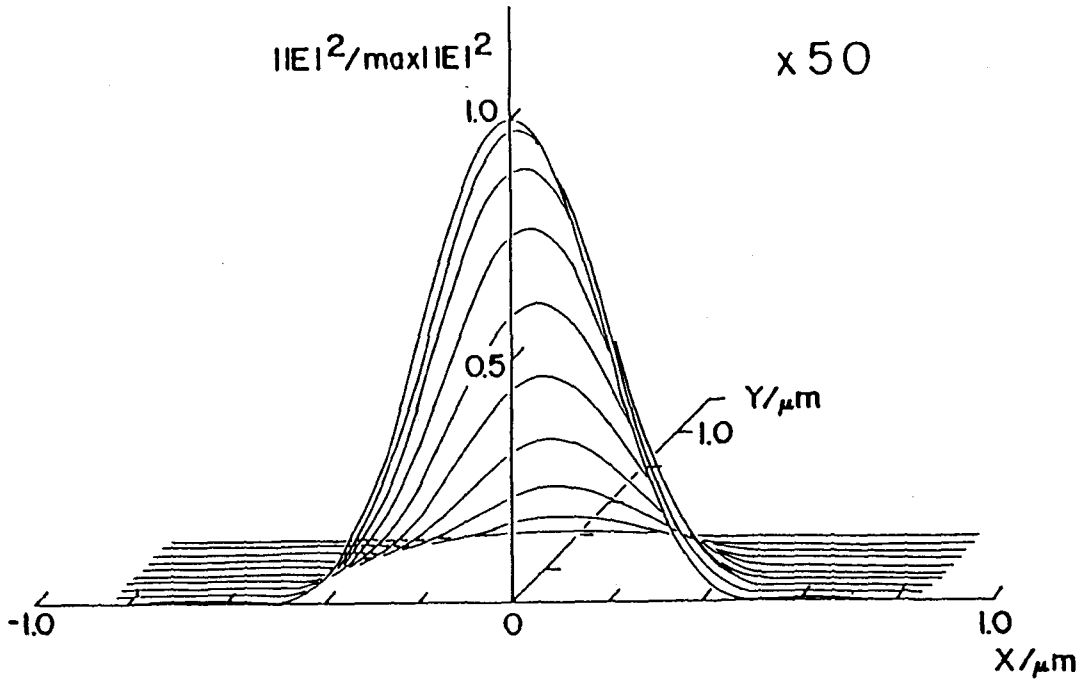

Fig.5-12. Energy distribution within X-Y plane of NA 0.80.

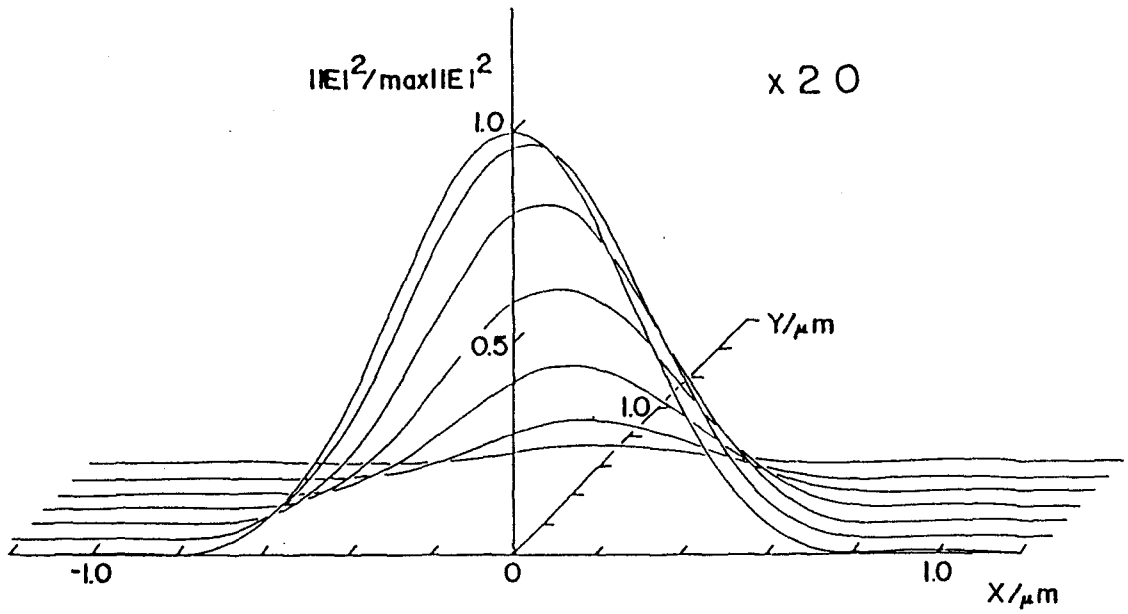

Fig.5-13. Energy distribution within X-Y plane of NA 0.46.

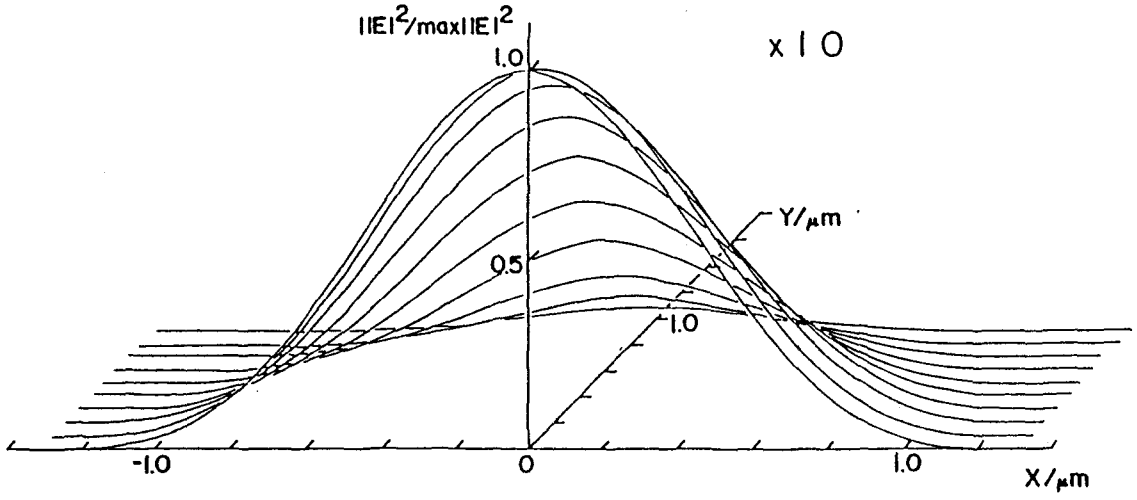

Fig.5-14. Energy distribution within X-Y plane of NA 0.30.

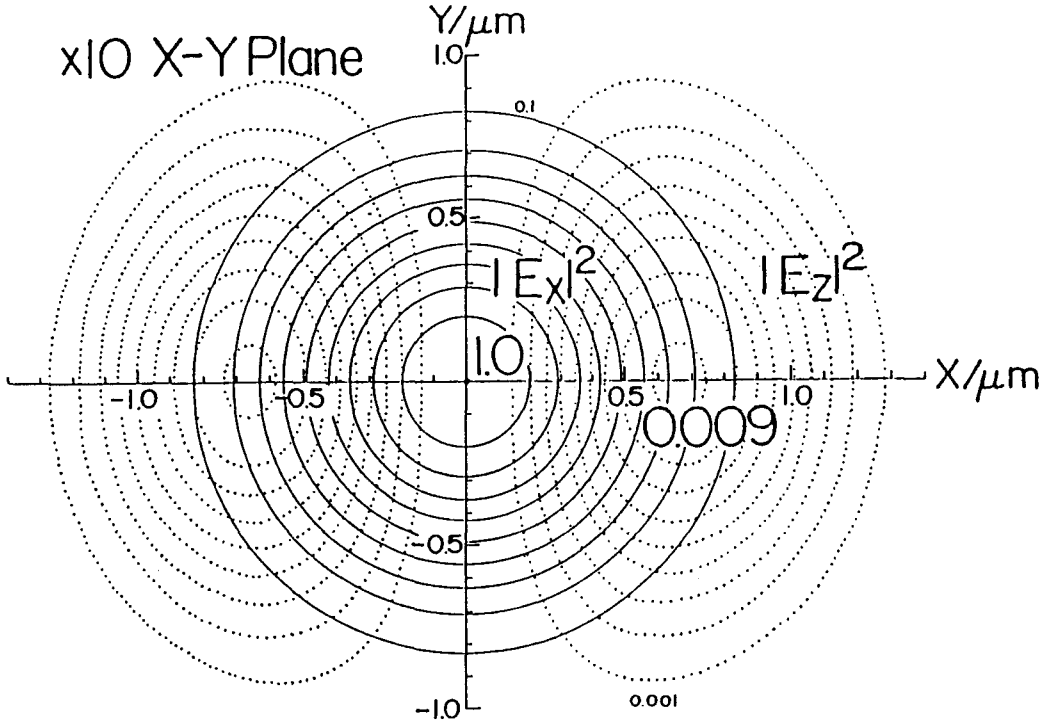

Fig.5-15. Contours of the time-averaged electron energy density in the focal plane Z = 0μm of NA 0.30, $|E_Z|^2_{max}$ = 0.009.

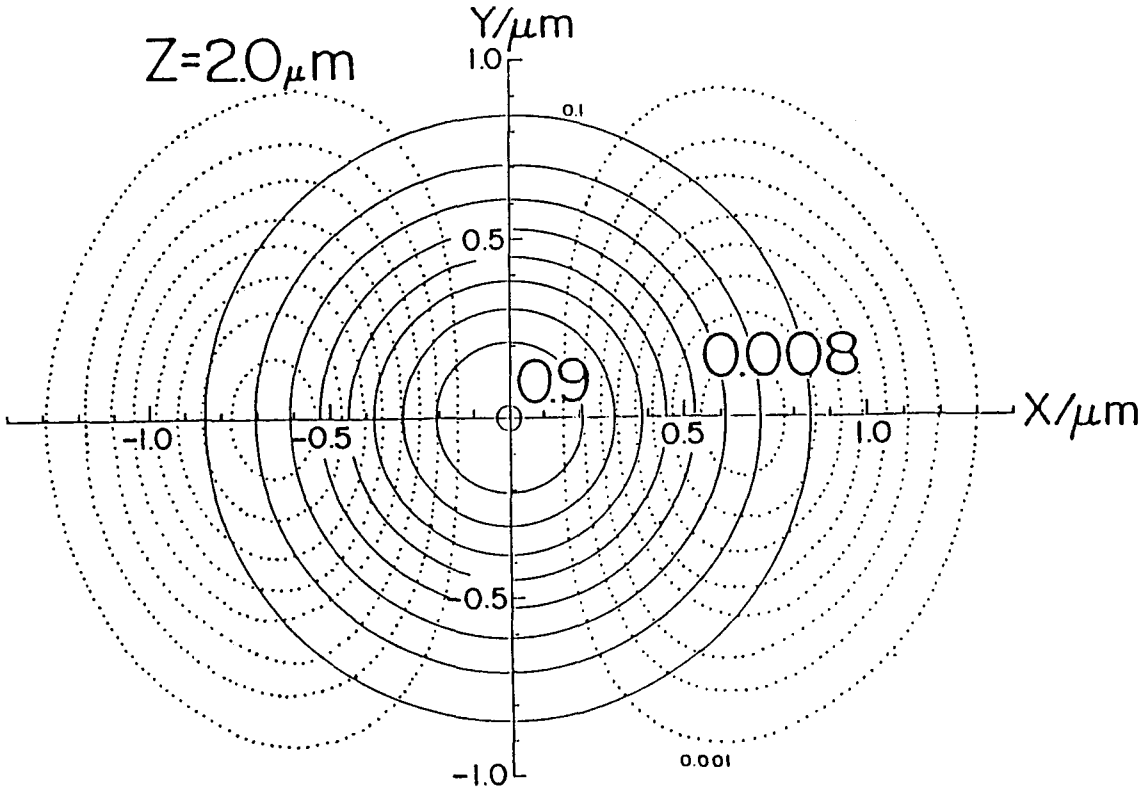

Fig.5-16. In the plane Z = 2.0 μ m of NA 0.30, $|E_Z|^2_{max}$ = 0.008.

values of $|E_X|^2$, $|E_Y|^2$, and $|E_Z|^2$ within the focal plane (S) are obtained by the integration from v = 0 to v = v_{max} which corresponds to the radius at the first minimum of $|E|^2$, the ratio being $\int|E_X|^2dS$: $\int|E_Y|^2dS$: $\int|E_Z|^2dS$ = 99 : 0 : 1. At Z = 2.0μm, the maximum value of $|E_X|^2$ reduces to 0.9 and that of $|E_Z|^2$ to 0.008 (Fig.5-16). Two components decrease with Z in proportional to each other. At Z = 0.5 μm (Fig.5-17), $|E_X|^2$ and $|E_Z|^2$ reduce to the half of those at the focal plane and $|E_Z|^2$ spreads out side. At Z = 11.5μm (Fig.5-18) the relative intensities become a few% of those at Z = 0μm. For the magnification x100 the ratio at the focal plane is obtained as $\int|E_X|^2dS$: $\int|E_Y|^2dS$: $\int|E_Z|^2dS$= 85 : 1 : 14 (Fig.5-19). Two maximum of $|E_Z|^2$ are attained at X = ±0.22 and Y = 0μm. The intensities decrease more rapidly along the Z axia (Figs 5-19 -22). It should be noted that with higher magnification of the objective, the contribution of the vertical component E_Z becomes more significant.

5-5. Analysis of Polarization Measurements

5-5-1. Intensities of Polarized Spectra

In this section the method of analysis for polarized micro-Raman spectra is considered. A general equation expressing the scattered intensity I has been derived by Turrell[1] as

$$\begin{aligned} I = &(\alpha_{XX}^2A + \alpha_{XY}^2A + \alpha_{XZ}^2B)(2C_0 + C_2) \\ &+(\alpha_{YX}^2A + \alpha_{YY}^2A + \alpha_{YZ}^2B) C_2 \\ &+(\alpha_{ZX}^2A + \alpha_{ZY}^2A + \alpha_{ZZ}^2B) 4C_1 \end{aligned} \qquad (5\text{-}14)$$

where

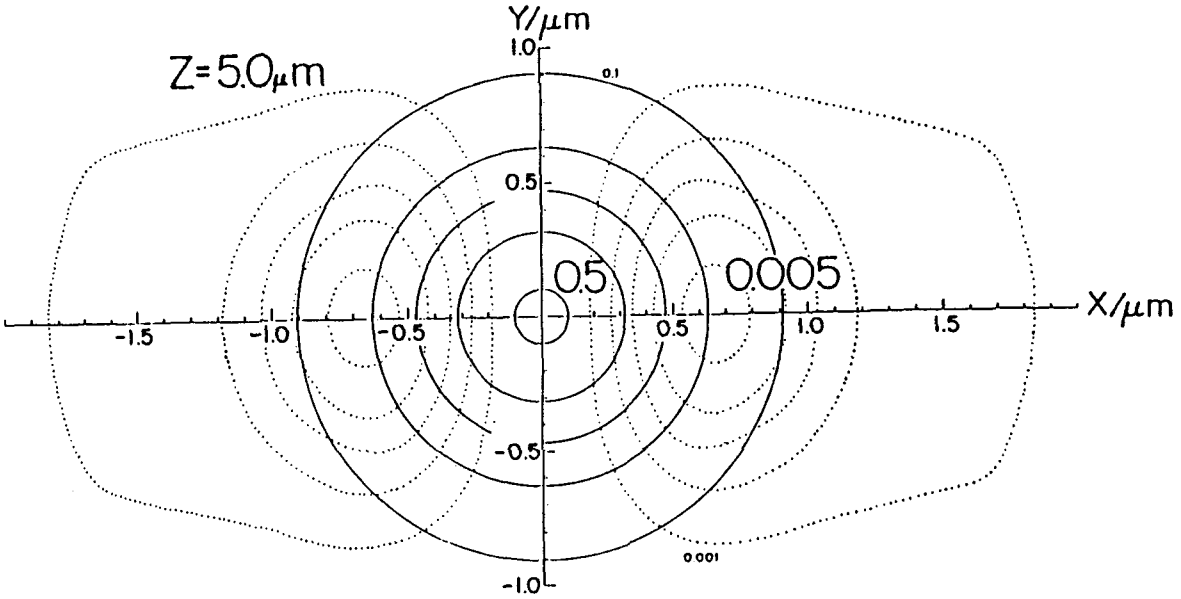

Fig.5-17. In the plane Z = 5.0 μ m of NA 0.30, $|E_Z|^2_{max}$ = 0.005.

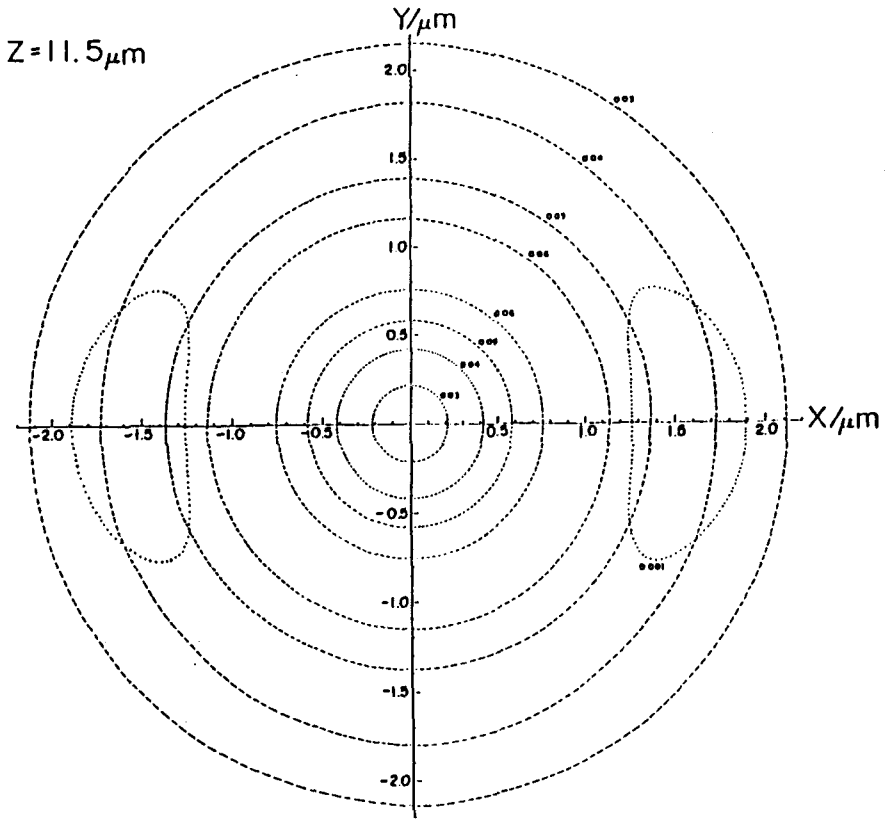

Fig.5-18. In the plane Z = 11.5 μ m of NA 0.30, $|E_Z|^2_{max}$ = 0.001.

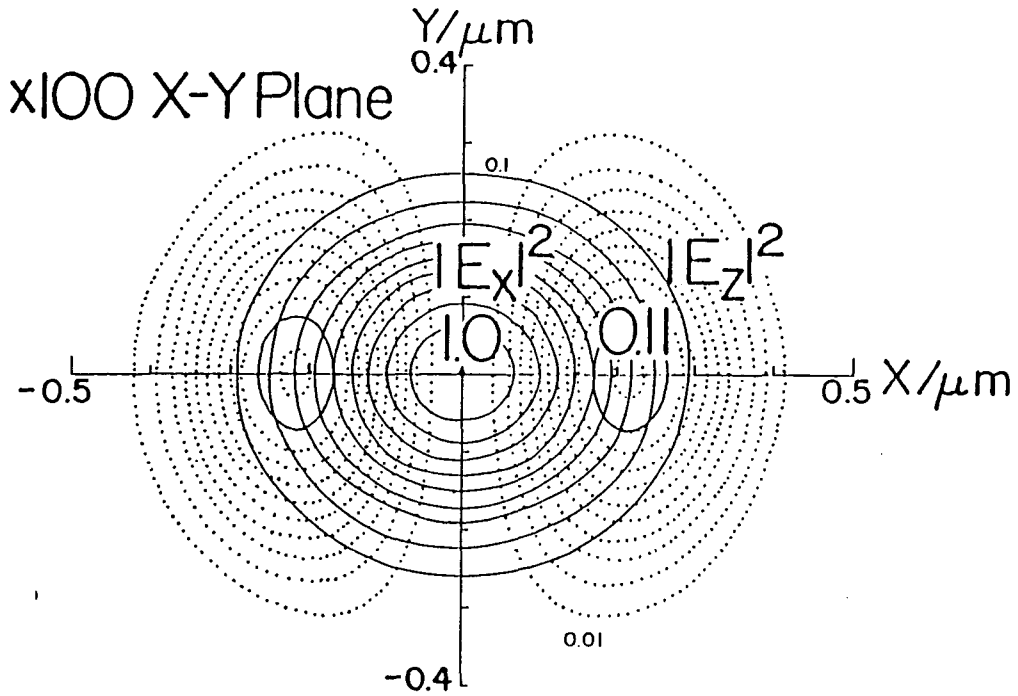

Fig.5-19. Contours of the time-averaged electric energy density in the focal plane Z = 0μm of NA 0.90, $|E_z|^2$max = 0.11.

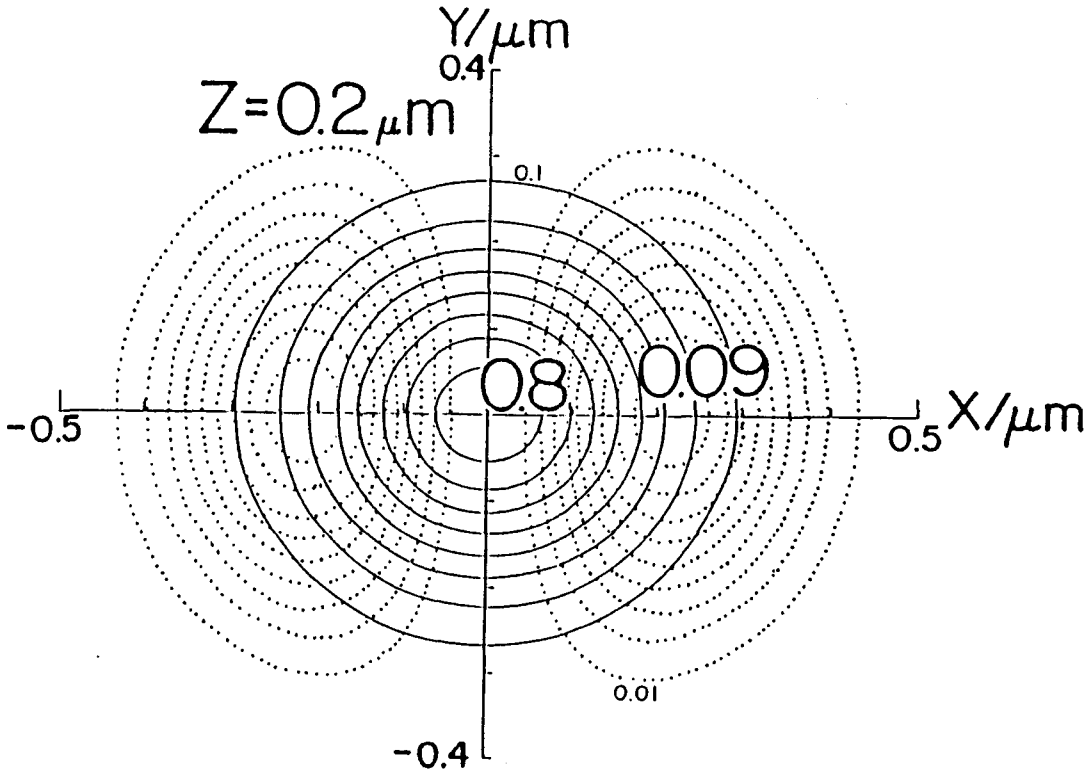

Fig.5-20. In the plane Z = 0.2μm of NA 0.90, $|E_z|^2$max = 0.09

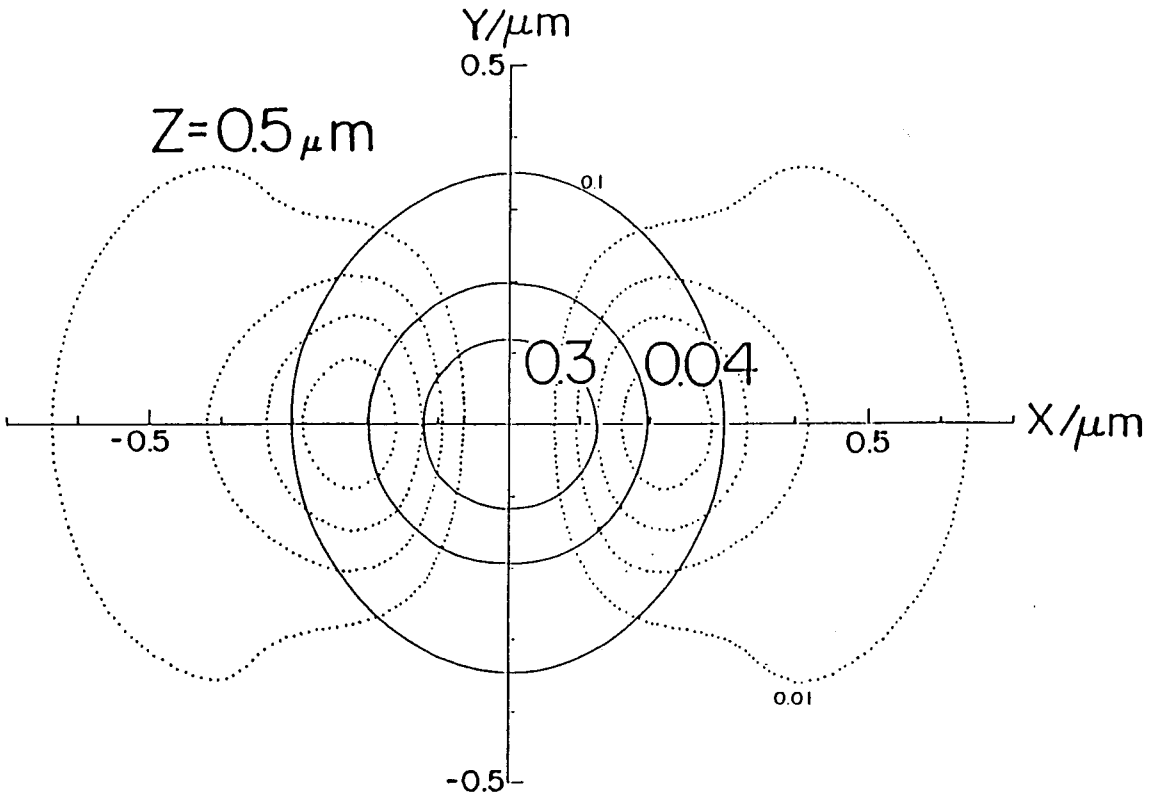

Fig.5-21. In the plane Z = 0.5μm of NA 0.90, $|E_Z|^2_{max}$ = 0.04.

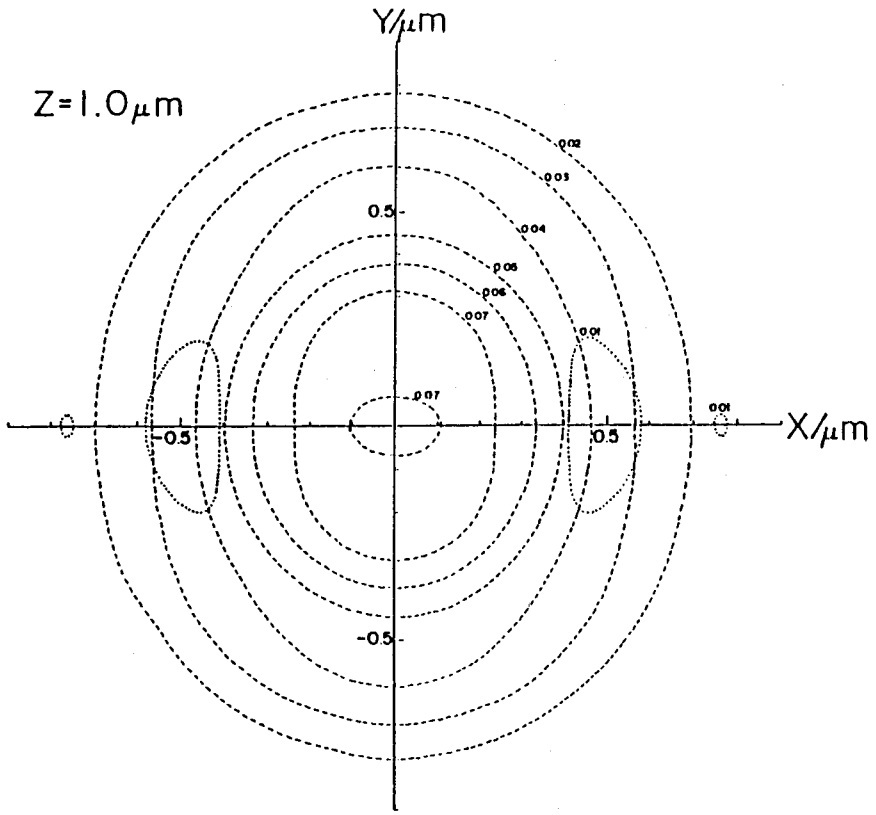

Fig.5-22. In the plane Z = 1.0μm of NA 0.90, $|E_Z|^2_{max}$ = 0.01.

$$A = \pi^2((4/3) - \cos\theta_m - (1/3)\cos^3\theta_m) \quad (5\text{-}15)$$

$$B = \pi((2/3) - \cos\theta_m + (1/3)\cos^3\theta_m) \quad (5\text{-}16)$$

Here, the Raman tensor α_{IJ} is formulated in terms of the space-fixed Cartesian coordinates I, J = X, Y, Z. The parameters A and B are related to the in-plane and Z components of the electric vector of the scattered light to be collected by the objective. C_0, C_1, and C_2 are associated with the squares of the X, Y, and Z elements of the incident electric field. Turrell evaluated the values of C_0, C_1, and C_2 by the integration over the whole space. Thus, the values are independent of the position of the focus and therefore, are not applicable to analyse the spectral changes caused by the shift of the focus in the sample. As described in the preceding section, the energy of the incident light is concentrated on the focal plane, and the light scattered from the plane is dominant compared with that from the rest of the whole space. Therefore, as an approximation, the incident electric field only on the focal plane is assumed here to contribute to the scattering intensity. Thus, C_0, C_1, and C_2 are obtained by the integration over the focal plane, instead of the whole space, as

$$C_0 = \int_0^{v_{max}} |I_0|^2 \, vdv \quad (5\text{-}17)$$

$$C_1 = \int_0^{v_{max}} |I_1|^2 \, vdv \quad (5\text{-}18)$$

$$C_2 = \int_0^{v_{max}} |I_2|^2 \, vdv \quad (5\text{-}19)$$

The values of the parameters A, B, C_0, C_1, and C_2 calculated for the four objectives with different magnifications are listed in Table V-II.

For polarization analysis, for example, the scattered intensity for $Z(X\ X)\bar{Z}$ polarization is given with the eq 5-14 as follows. The incident light with X polarization is represented with terms $(2C_0 + C_2)$ (X-polarization component), C_2 (Y-polarization laekage component caused by the collection of the incident light by the high NA objective, this term is negligible compared with the X and Z components) and $4C_1$ (Z-polarization component caused by the collection). The scattered light is with $\alpha_{XX}{}^2A$, $\alpha_{YX}{}^2A$, $\alpha_{ZX}{}^2A$ (X-polarization), and $\alpha_{XZ}{}^2B$, $\alpha_{YZ}{}^2B$, $\alpha_{ZZ}{}^2B$ (Z-polarization). As a result, I is expressed as

$$I = (\alpha_{XX}^2 A+(1/2)\ \alpha_{XZ}^2 B)(2C_0+C_2) + (\alpha_{YX}^2 A+(1/2)\ \alpha_{YZ}^2 B)C_2 + (\alpha_{ZX}^2 A+(1/2)\ \alpha_{ZZ}^2 B)4C_1 \quad (5\text{-}20)$$

Similarly for $Z(X\ Y)\bar{Z}$ polarization

$$I = (\alpha_{XY}^2 A+(1/2)\ \alpha_{XZ}^2 B)(2C_0+C_2) + (\alpha_{YY}^2 A+(1/2)\ \alpha_{YZ}^2 B)C_2 + (\alpha_{ZY}^2 A+(1/2)\ \alpha_{ZZ}^2 B)4C_1 \quad (5\text{-}21)$$

Here, the terms $\alpha_{XZ}^2 B$, $\alpha_{YZ}^2 B$, and $\alpha_{ZZ}^2 B$ contribute to I for $Z(X\ X)\bar{Z}$ and $Z(X\ Y)\bar{Z}$ polarization equivalently.

5-5-2. Analysis of Polarized Spectra of α-Quartz and o-POM Single Crystals

With the parameters calculated above, the spectral analysis of α-quartz and o-POM single crystals was carried out.

Table V-II. Parameters A, B, C_0, C_1, and C_2 for various magnifications.

Magnification	N A	θ_m	f	A	B	C_0	C_1	C_2
x100	0.90	64.2°	0.56	8.593	0.8134	2.140	0.1826	0.02636
x50	0.80	53.1°	0.63	6.521	0.4348	1.676	0.1039	0.01024
x20	0.46	27.4°	1.09	2.095	0.0381	0.5500	9.692×10^{-3}	2.227×10^{-4}
x10	0.30	17.5°	1.66	0.8928	0.0066	0.2346	1.683×10^{-3}	1.470×10^{-5}

a) α-Quartz: α-Quartz crystal has the D_3 symmetry and contains three SiO_2 units per unit cell. Factor group analysis predicts that of the 24 zone-center normal modes four are totally symmetric (A_1 modes) and eight are doubly degenerate (E modes). The remainder is four infrared-active A_2 modes.[9-13] The elements of the Raman tensors for the D_3 symmetry have the following form (the optical axis // z):[14]

$$A_1 \begin{pmatrix} a & & \\ & a & \\ & & b \end{pmatrix}, \quad E(x) \begin{pmatrix} c & & \\ & -c & d \\ & d & \end{pmatrix}, \quad E(y) \begin{pmatrix} & -c & -d \\ -c & & \\ -d & & \end{pmatrix} \qquad (5\text{-}22)$$

The relative squared values of the elements have been determined experimentally by the right angle scattering measurement as a^2 = 906, b^2 = 1000 for the 464cm^{-1} A_1 mode and c^2 = 11, d^2 = 1 for the 394cm^{-1} E mode.[13] Bremard et al.[4,15] derived first the equations of the intensities of the micro-Raman polarization components, but they missed the contribution of the axial component. Taking this term, the equations describing the intensties of the $z(x\ x)\bar{z}$ and $z(x\ y)\bar{z}$ components are obtained as summarized in Table V-III.

With the formulae the changes in spectra with variation of the focal position in α-quartz were analyzed. Figs.5-23 and 5-24 show the spectra in the 300 to 500cm^{-1} region for the $z(x\ y)\bar{z}$ and $z(x\ x)\bar{z}$ polarizations, respectively, measured with an objective (NA = 0.90), at the three focal positions (measured from the surface) (1) d = 0mm, (2) 0.15mm, and (3) 0.30mm. Appreciable depth dependence was obsereved in the $z(x\ y)\bar{z}$ component. The obsereved ratios E(x)+E(y)(394cm^{-1})/A_1(464cm^{-1}) of the integrated intensties are listed in Table V-IV. Here the

Table V-III. Formulae of polarized intensities for α-quartz.

	$z(x\ x)\bar{z}$	$z(x\ y)\bar{z}$
A_1	$a^2A(2C_0 + C_2) + 2b^2BC_1$	$a^2AC_2 + 2b^2BC_1$
E_x	$c^2A(2C_0 + C_2) + \frac{1}{2}d^2BC_2$	$c^2AC_2 + 4d^2AC_1 + \frac{1}{2}d^2BC_2$
E_y	$c^2AC_2 + 4d^2AC_1 + \frac{1}{2}d^2B(2C_0 + C_2)$	$c^2A(2C_0 + C_2) + \frac{1}{2}d^2B(2C_0 + C_2)$

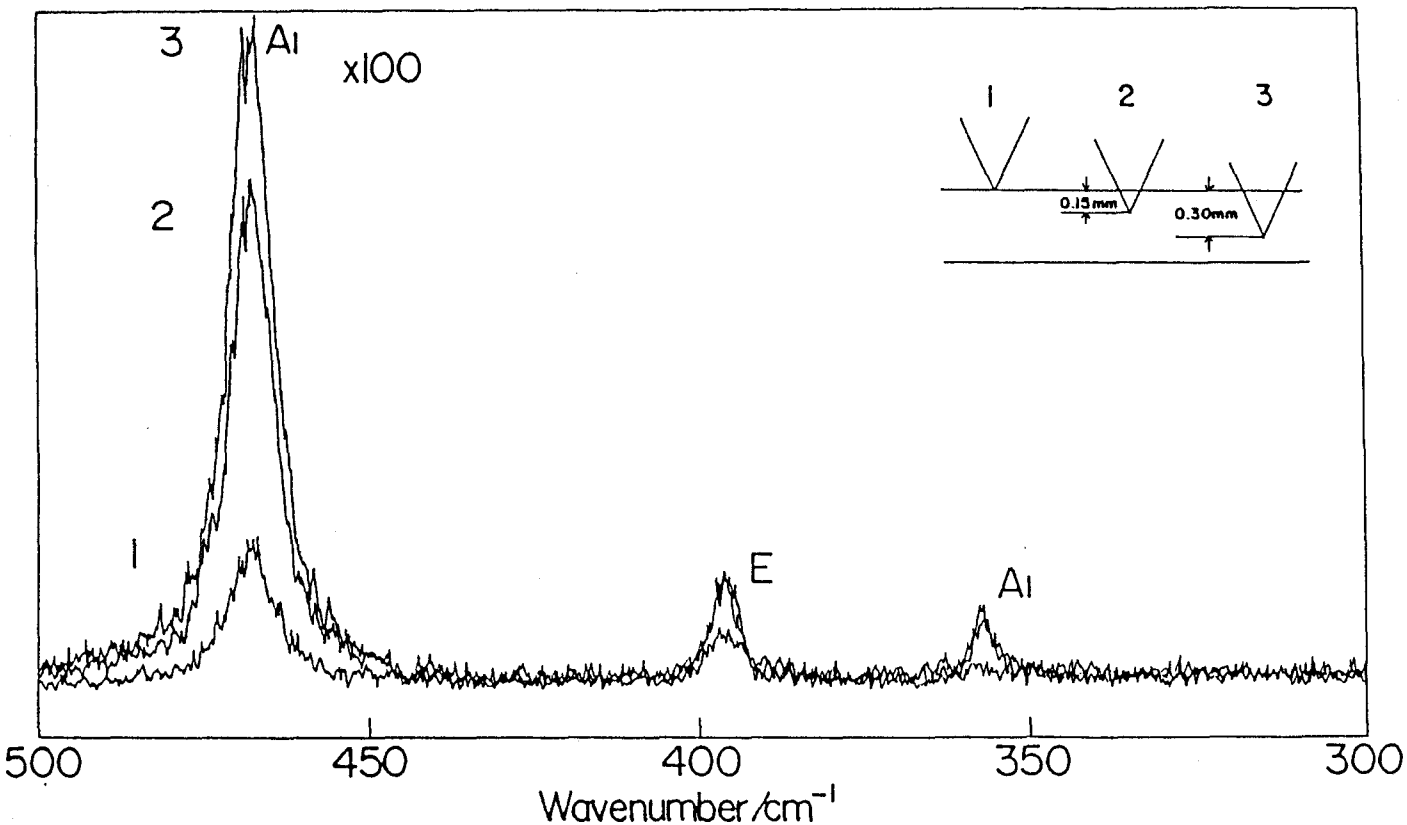

Fig.5-23. Depth of the focus dependence for micro-Raman spectra of $z(x\ y)\bar{z}$ polarization in α-quartz.

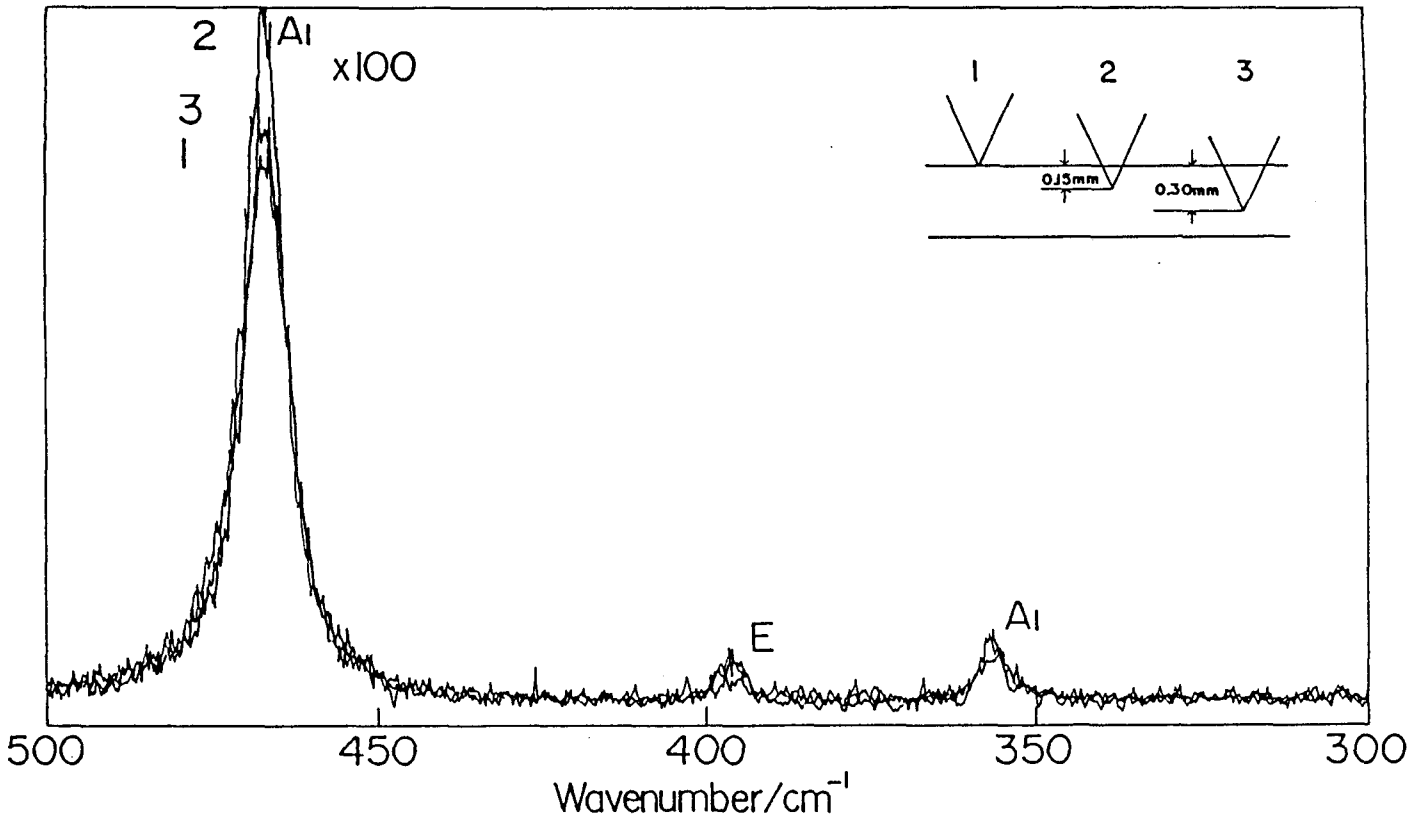

Fig.5-24. Depth of the focus dependence for micro-Raman spectra of $z(x\ x)\bar{z}$ polarization in α-quartz.

Table V-IV. Depth of the focus dependence of calculated and observed intensity ratio $E(x)+E(y)(394cm^{-1})/A_1(464cm^{-1})$ in α-quartz.

		$z(x\ y)\bar{z}$		$z(x\ x)\bar{z}$	
d/mm	ζ /°	obs.	calc.	obs.	calc.
0.00	0.00	0.25	0.83	0.038	0.012
0.15	4.35	0.12	0.38	0.040	0.012
0.30	8.70	0.11	0.20	0.042	0.012

effect of the optical rotation[16] of angle ζ was taken into account for the incident radiation which has been ignored in ref.4. A fairly good agreement was obtained between the obsereved and calculated values.

b) o-POM: Next the polarization spectra for an o-POM microcrystal were analysed. Two 2/1 helical molecules passes through the unit cell of o-POM.[20] The optical-active vibrational modes are treated by the factor group isomorphous to the point group D_2. The line group for the single 2/1 helical molecule also belongs to D_2. The $A-B_1$ or B_2-B_3 pairs of the molecular modes in the crystal is due to the correlation field splitting (Davydov splitting). Here the sample-fixed Cartesian coordinates were defined as follows: X is parallel to the striation, Y perpendicular to it within the plate surface, and Z normal to the plate surface (Fig.5-25). Based on the observation of the polarized Raman and Infrared spectra and the result of the normal mode analysis, Kobayashi et al.[18,19] determined that the X, Y, and Z directions were parallel to the crystallographic c, a, and b axes, respectively. Fig 5-25 shows the spectra in the region of 800-1200cm^{-1} of $Z(X\ Y)\bar{Z}$ polarization of o-POM. With decreasing magnifications of the objective from x100 to x20, the observed ratio B_2/B_3 increases appreciably. This is caused by the contribution of axial polarization component in the incident and scattered lights. The fraction is largest in x100 and is reduced with decreasing magnification. The polarizability tensor of B_2 and B_3 mode are given as[14]

$$B_2 \begin{pmatrix} & e & \\ e & & \end{pmatrix}, \qquad B_3 \begin{pmatrix} & f & \\ f & & \end{pmatrix} \tag{5-23}$$

The scattering intensities of B_2 at $950cm^{-1}$ and B_3 at $937cm^{-1}$ for the $b(c\ a)\bar{b}$ polarization are represented as

$$I(B_2) = e^2 A\ 2(C_0 + C_2) \tag{5-24}$$

$$I(B_3) = (1/2)f^2 B\ (2C_0 + C_2) \tag{5-25}$$

The B_2 and B_3 modes exhibit the same scattering power in powder sample.[18] Thus, $e^2 \cong f^2$ and $C_0 \gg C_2$. Therefore from eqs 5-24 and 5-25 the intensity ratio $I(B_2)/I(B_3)$ is given as

$$I(B_2)/I(B_3) = 2A/B \tag{5-26}$$

The ratio $I(B_2)/I(B_3)$ was calculated with the parameters listed in Table V-II. The results are listed in Table V-V with the observed ratios. The calculated ratio increases as the magnification rises but its magnitude is about 10 times larger than that observed. The difference might be ascribed to the depolarization effects caused by the optical inperfections on the crystal surface.

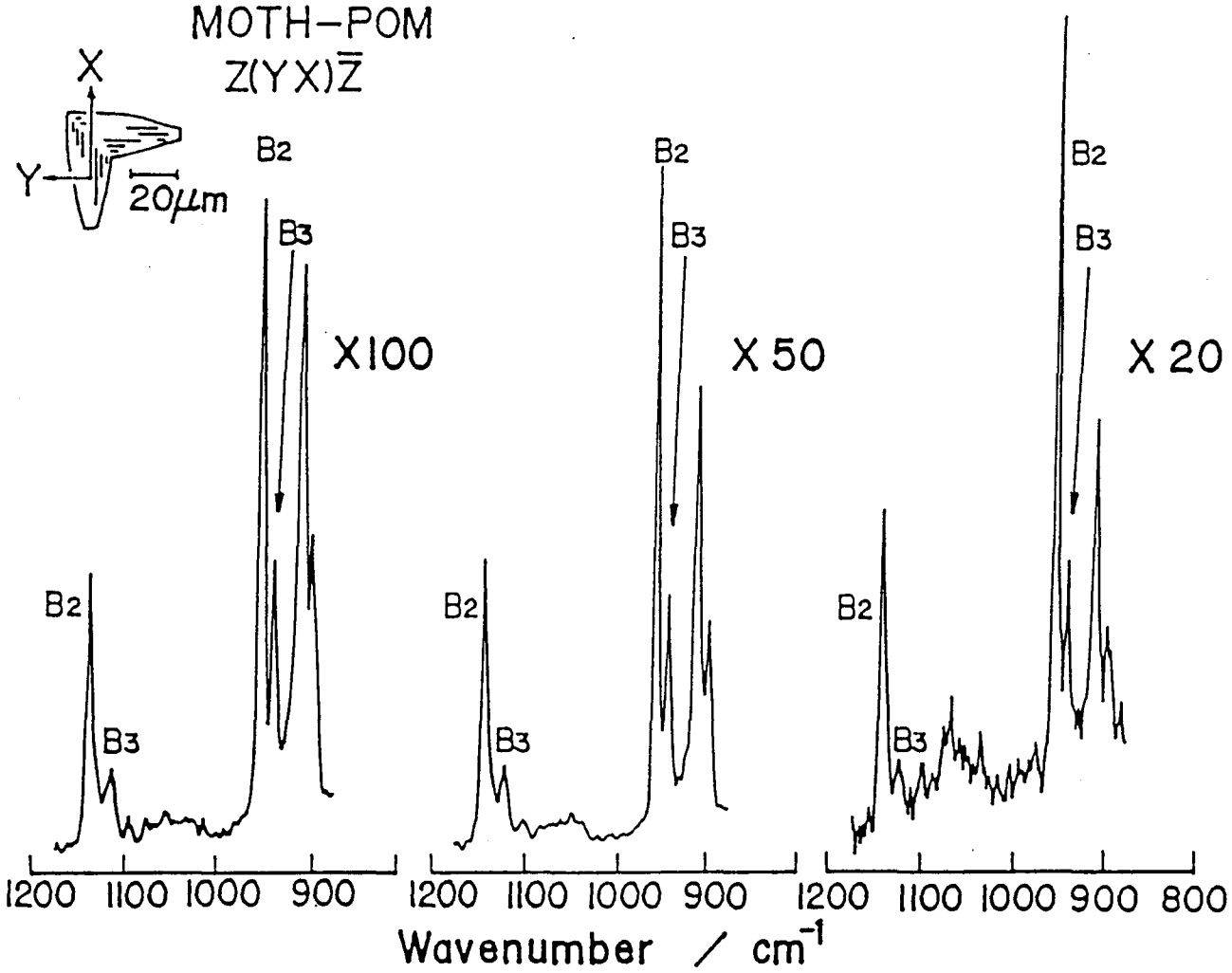

Fig.5-25. Magnification of objective dependence for micro-Raman spectra of Z(Y X)$\bar{Z}$ polarization in o-POM single crystal.

Table V-V. Magnification dependence of calculated and observed peak intensity ratio $B_2(950cm^{-1})/B_3(937cm^{-1})$ in o-POM.

Magnification	x100	x50	x20
$I(B_2)/I(B_3)$ calc.	21	30	110
$I(B_2)/I(B_3)$ obs.	2.4	2.9	3.8

5-6. References

1) G Turrell, J. Raman Spectrosc., 15, 103 (1984).

2) B. Richards and E. Wolf, Pro. R. Soc. London, A253, 349 (1959).

3) A. Boivin and E. Wolf, Phys. Rev. B, 138, 1561 (1965).

4) C. Bremard, P. Dhamelincourt, J. Laureyns, and G. Turrell, Appl. Spectrosc., 39, 1036 (1985).

5) M. Kobayashi, Y. Itoh, H. Tadokoro, M. Shimomura, and M. Iguchi, Polym. Commun., 24, 38 (1983).

6) H. Morishita, T. Ishioka, and M. Kobayashi, J. Phys. Chem., 91, 2273 (1987).

7) A. Ishitani, "Raman Microprobe", Sekigai-Raman-Shindou, Kagaku no Ryoiki, Vol.140, Nankb-do, Co., Tokyo, 1983.

8) E. Wolf, Proc. R. Soc. London, A253, 349 (1959).

9) V. G. Zubov and L. P. Osipova, Kristallografiya, 6, 418 (1961). (Soviet Phys. Crystallogr., 6, 330 (1966)).

10) D. F. Kiselev and L. P. Osipova, Kritallografiya, 11, 279 (1966). (Soviet Phys. Crystallogr., 11, 255 (1966)).

11) D. F. Kiselev and L. P. Osipova, Kristallografiya, 11, 401 (1966). (Soviet Phys. Crystallogr., 11, 357 (1966)).

12) A. S. Pine and P. E. Tannewald, Phys. Rev., 178, 1424 (1969).

13) J. D. Masso, C. Y. She, and D. F. Edwards, Phys. Rev., B, 1, 4179 (1970).

14) R. Loudon, Adv. Phys., 13, 423 (1964).

15) C. Bremard, P. Dhamelincourt, J. Laureyns, and G. Turrell, J. Mol. Struct., 142, 13 (1986).

16) S. Chandrasekhar, Proc. R. Soc. London, A259, 531 (1961).

17) G. Carazzo and M. Mammi, J. Polym. Sci., A1, 965 (1963).

18) M. Kobayashi, H. Morishita, T. Ishioka, M. Iguchi, M. Shimomura and T. Ikeda, J. Mol. Struct., 146, 155 (1986).

19) H. Morishita and M. Kobayashi, Rep. Prog. Polym. Phys. Jpn., in press (1987).

Chapter 6

Summary and Conclusion

In this thesis, the author studied the structures and the transition behaviors of two kinds of ion-containing long chain compounds; ethylene-methacylic acid (E-MA) ionomers and N,N'-dialkyl-1,4-diazabicyclo(2,2,2)octane halides with vibrational spectroscopic methods and small-angle x-ray scattering (SAXS) technique, and also dealt with some fundamental problems in the analysis of the micro-focus Raman spectroscopy as a new technique for the microcharacterization of microdomain structures. The summary is listed below.

Chapter 1. Brillouin and Raman Study on Melting Process of Ethylene-methacrylic Acid Ionomers

In this chapter, the author investigated how the presence of the ionic groups influences the molecular-level structure of the ionic and the non-ionic parts of E-MA ionomers and, as a result, increases the elastic constant.

The author compared the changes in structures as well as in the elastic constant on the melting process of the two ionomers: E-MA-Na and E-MA-Zn, and non-ionic low density polyethylene (LDPE). Temperature dependence of the elastic constant was measured for the three samples with Brillouin scattering method. Characteristic melting behavior was found for the two ionomers. The elastic constant of E-MA-Na showed a plateau in the range in 60-90 ^{o}C followed by a sharp depression at 100 ^{o}C. On the other hand in E-MA-Zn, there arose a smaller plateau in the range 70-80 ^{o}C and a sharp depression started at 80 ^{o}C. In contrast to the ionic samples, depression of the elastic constant of LDPE occurred more gradually in the lower temperature region in 60-

80 °C without plateau. To elucidate the characteristic melting behavior from the structural view point, temperature dependence of the degree of crystallinity of polyethylene phase, the structural changes in the ion aggregate, and the acid dimer-monomer equilibrium were investigated. However, the appreciable correlation was not found between these structural changes and the temperature dependence of the elastic constant.

With Raman method, the author investigated the conformational order, in other word, the amount of short trans-sequence of polyethylene chains in the non-crystalline phase. Close correlation between the temperature dependence of the order and that of the elastic constant was found. This was also confiremed by the temperature dependence of the intensity of the D-LAM band. The high elasticity of the ionomers was suggested to be significantly affected by the amount of short trans sequences in the non-crystalline region.

Chapter 2. Small-angle X-ray Scattering Study on Structural Changes of Ion Cluster in Zinc Salt of Ethylene-methacrylic Acid Copolymer on Water Absorption

In order to reveal the characteristic mechanical properties of ionomers, investigation of the structure of the ion aggregate, i.e. cluster, is necessary. In this chapter, the dimensional changes of ion aggregate on water absorption in the E-MA-Zn ionomer was examined with SAXS technique. The change of the Bragg spacing ascribed to the cluster dimension from 22.4 to 15.4Å was observed as the water content decreased from 0.19 to

0.06wt%. The change occurred reveasibly with absorption-desorption procedure. In order to interpret the change, the SAXS curves were analyzed quantitatively with the scattering intensity equation for a model of closely assembled hard spheres having an uniform radius. The result indicated that the change of the scattering profile on the water absorption-desorption process was interpreted by the change of the closest approach distance between the clusters and of the cluster electron density. As for the cluster structure, the core radius of 0.38-0.40nm, the closest approach distance of 0.84-0.75nm, a sample volume per perticle of $13nm^3$ were obtained.

Chapter 3. Infrared Study on Intra-cluster Structural Changes in Zinc Salt of Ethytlene-methacrylic Acid Copolymer on Water Absorption

Local structural change in the ion aggregate in E-MA-Zn on water absorption-desorption process was investigated with infrared spectroscopy. In the dried state, three split bands at 1539, 1560, and 1625cm^{-1} were found in the ν_a(COO) region. On swelling they collapsed into a singlet at 1587cm^{-1}. The spectral change was observed reversibly with respect to the water content. From the analysis of the change in IR band intensity with respect to the amount of absorbed water, about one water molecule is revealed to be absorbed on two zinc cations. In the hydrated state, the zinc cation is suggested to be surrounded by tetrahedrally by two oxygens of unidentate carboxylate groups and (1/2) water molecule (one water molecule may be located between two zinc cations). The band split in a dry state was

interpreted to be caused by the vibrational coupling among the vibrational units rather than by the change of the coordination structure. Simple coupled oscillator model consisting of three vibrational units of zinc methacrylate anhydride was considered to analyse the split frequencies and, as for the intra-cluste structure in a dry sate, the aggregate of the three zinc methacrylate anhydrides having tetrahedral coordination to each zinc cation was proposed. The structure was quantitatively consistent with the SAXS analysis in chapter 2.

Chapter 4. Phase transition of Ion containing Long-chain Compounds

In order to reveal the effect of the ionic groups on the conformational orderliness of the non-ionic alkyl chains, the structural transition behaviors of bis- and mono-alkyl DABCO halides were investigated as model compounds of E-MA ionomers.

The bis-alkyl DABCO bromide of C_{19}-DABCO-C_{18}-Br_2 shows one-step phase transition at 93 °C. The subcell structure of the alkyl chains in the low temperature phase was determined as $T_{//}$ type with IR polarized spectra. All-trans conformation was kept in the phase. As increasing temperature, above the transition point, conformational order of the alkyl chains went into liquid state and disordering of the chain-packing occurred. The same transition behavior was observed for the homologous series of C_n-DABCO-C_n-X_2. Onset of reorientational rotational motion of the bicycloring was suggested in the high temperature phase.

In contrast, mono-alkyl DABCO bromides of such as C_7-DABCO-

Br and C -DABCO-Br have two steps phase transition at temperature T_{c1} and T_{c2}. In the temperature (T) range $T < T_{c1}$, their alkyl chains take all-trans conformation and the subcell structure was determined as $O_{\perp}$ packing from the crystal field splitting of the $\delta(CH_2)$ and $r(CH_2)$ modes. In $T_{c1} < T < T_{c2}$, the subcell structure changed into $T_{//}$ or hexagonal packing and the splitting disappeared. The chains took trans conformation having a little conformational disorder. In $T < T_{c2}$ the chain went into disordered state and the rotational-disorder or -motion of the bicycloring took place.

The presence of the ion groups was revealed to stabilize the conformational orderliness of the non-ionic alkyl chains of these compounds to higher temperatures compared with n-alkanes and the result in chapter 1 was confirmed.

Chapter 5. Application of Raman Microprobe as a new Technique for Polarization Measurement of Microdomain Structures

The author solved the problems of the spatial resolution and the polarization analysis of Raman microprobe technique in order to develop new microcharacterization technique for microdomain structures in such as ionomers. The experimental axial resolution was investigated with a single crystal of stearic acid B form whose (001) surface was covered with overgrown steps of different polytypic structure. Spatial resolution for axial and horizontal directions in vacuum were estimated theoretically by the analysis of spatial distribution of the incident electric field near the focal point. Based on the results, a method of correction for the polarization scrambling effect caused by the

sharp focusing objective in the polarization analysis was developed. The method was applied to the polarization analysis of the spectra for the single crystals of α-quartz and o-POM.

In this way, vibrational spectra: their frequencies, band-width, and intensities of the ion-containing long chain compounds have a lot of informations about the static molecular structure, their transition behaviors, and dynamical motions of the molecules. With X-ray diffraction methods and more detailed vibrational analysis with normal mode calculations, this fruitful new field of molecular structural study will be further explored.

List of publications

The contents of this thesis have been or will be published in the following papers.

1. Structural Changes in Ionomers on Water Adsorption
   T. Ishioka and M. Kobayashi, Rep. Prog. Polym. Phys. Jpn., 29 195 (1986).
2. Vibrational Spectroscopic Study on Polymorphism and Molecular Aggregation States in Polyoxymethylene
   M. Kobayashi, H. Morishita, T. Ishioka, M. Iguchi, M. Shimomura, and T. Ikeda, J. Mol. Struct., 146, 155 (1986).
3. Application of Raman Microprobe Technique to the Study of Organic Polymers and Long Chain Compounds
   M. Kobayashi and T. Ishioka, "Vibrational Spectra and Structure", H. D. Bist, J. R. Durig, and J. F. Sullivan, eds, Elsevier, Amsterdam, Vol. 17B, 369-390 (1989).
4. Structural Transition Behavior of Potassium Stearate
   T. Ishioka, Rep. Prog. Polym. Phys. Jpn., 32, 195 (1989).
5. Small-angle X-ray Scattering Study for Structural Changes of Cluster in Zinc Salt of Ethylene-methacryli Acid Ionomer on Water Absorption
   T. Ishioka and M. Kobayashi, Macromolecules, in press (1990).
6. Brillouin and Raman Study on Melting Process of Ethylene-methacrylic Acid Ionomers
   T. Ishioka and M. Kobayashi, Macromolecules, to be published.
7. Infrared Study on Intra-cluster Structural Changes in Zinc Salt of Ethylene-methacrylic Acid Copolymer on Water Absorption
   T. Ishioka and M. Kobayashi, Macromolecules, to be published.

8. Raman Study on Structural Transition of N, N'-distearyl-1,4-diazabicyclo(2,2,2)octane Bromide
   T. Ishioka, M. Kobayashi, J. Shimuzu, T. Nogami, and Y. Shirota, Bull. Chem. Soc. Jpn., to be published.
9. Study of Spatial Resolutions and Polarization Analysis in Raman Microprobe Technique
   T. Ishioka and M. Kobayashi, Appl. Spectrosc., to be published.

Related Papers

1. Study of Micropolytype Structures in Crystals of Stearic Acid B Form by Raman Microprobe Technique
   H. Morishita, T. Ishioka, M. Kobayashi, and K. Sato, J. Phys. Chem., 91, 2273 (1987).
2. The phase Transition of 1-Alkyl-4-aza-1-azoniabicyclo(2,2,2)-octane Bromides, Cn-DABCO-Br ($11 \leqq n \leqq 22$)
   K. Imamura, T. Nogami, Y. Shirota, T. Ishioka, and M. Kobayashi, Bull. Chem. Soc. Jpn., 60, 3879 (1987).
3. Crystal Structure of Poly(ethyleneimine)-acetic Acid Complex
   Y. Chatani, Y. Yakura, and T. Ishioka, Polymer, 31, 208 (1990).